Design, Assembly, and Testing of a Small 3D-printed Thick-GEM

by

Jerry Lamar Collins II

A thesis submitted to the College of Engineering and Science of
Florida Institute of Technology
in partial fulfillment of the requirements
for the degree of

Master of Science
in
Physics

Melbourne, Florida
December, 2021

We the undersigned committee hereby approve the attached thesis,
"Design, Assembly, and Testing of a Small 3D-printed Thick-GEM"
by
Jerry Lamar Collins II

DocuSigned by:
Marcus Hohlmann
Marcus Hohlmann, Ph.D.
Professor
Aerospace, Physics and Space Sciences
Major Advisor

DocuSigned by:
Gnana Bhaskar Tenali
Gnana Bhaskar Tenali, Ph.D.
Professor
Mathematical Sciences

DocuSigned by:
Francisco Yumiceva
Francisco Yumiceva, Ph.D.
Staff Transformational Physicist
Northrop Grumman Corporation

DocuSigned by:
David Fleming
David C. Fleming, Ph.D.
Associate Professor and Department Head
Aerospace, Physics and Space Sciences

Abstract

Title: Design, Assembly, and Testing of a Small 3D-printed Thick-GEM

Author: Jerry Lamar Collins II

Advisor: Marcus Hohlmann, Ph.D.

Thick GEMs are a type of gas electron multiplier, a micropattern gaseous detector, with many applications in research. The subject of this study is whether or not a small 3D printed thick GEM board can be used to form a well-functioning detector. A Thick GEM having three separate board sectors, each having different sized clearance rim annuli around their holes, was designed, printed, and assembled. Several studies to quantify its behavior over both short and long time intervals were conducted, and the results calculated. The THGEM sector with 0.1 mm annulus rims was able to achieve primarily 10^2 gain, whereas the sector with 0.2 mm annulus rims was able to achieve 10^3 gain by going to a higher bias voltage than the 0.1mm rim sector was able to achieve. The sector with 0.15 mm annulus rims was the only one able to achieve 10^4 gain. It was shown for the 0.2 mm rim sector that by leaving the Thick GEM powered for at least 10 hours, it is possible to stabilize the gain at an order of magnitude higher than what it would be if it had been in an off state for some time prior. While there were concerns with the overall long-term functionality of the Thick GEM, we show that they are able to perform as functioning GEMs.

Table of Contents

List of Figures

List of Tables

Acknowledgements

I would like to thank my God and Father, the Father of my Lord Jesus Christ. Without Him, I could do nothing.

I would like to thank my family, whose constant support I will forever be grateful for.

I would like to thank Dr. Marcus Hohlmann, my advisor and professor who has taught me very much over both my undergraduate and graduate career.

I would like to thank Dr. Aiwu Zhang, who taught me a great deal about GEM detector assembly.

I would like to thank the other members of HEP Lab A, including Mehdi Rahmani, Stephen Butalla, and Devon Madden for their support and assistance.

Dedication

This Thesis is dedicated to my mother, the greatest mother I could have ever hoped for, and the greatest person I know.

Chapter 1

Introduction

Gas Electron Multiplier, or, GEM detectors, are a type of gaseous detector. Gaseous detectors are particle detectors that take advantage of ionization caused by an incident particle passing through their gas volume, allowing for the detection of the incoming particle. A type of gaseous detector, of which GEM detectors are included, are micropattern gaseous detectors, or MPGDs, invented by Fabio Sauli in 1997 [1]. MPGDs are devices created to possess high rate and multi-track capabilities while having sturdier structures than previous detectors. These detectors were designed to have improved performance capabilities compared to previous detector types, as well as to mitigate long-term reliability problems [2]. GEM detectors are made up of components called GEM foils, which are Polyimide (Kapton®) foils coated in metal on both sides, typically copper, and chemically etched such as to have many tiny holes, typically 50-100 per square mm [1]. An example of a GEM foil is shown in Figure 1. The chemical etching is done via controlled immersion in a polymer-specific solvent. This produces double-conical holes that are beneficial for reducing the charging up of the insulator, which would affect the gain [3]. An example of a GEM foil can be seen in Figure 1.

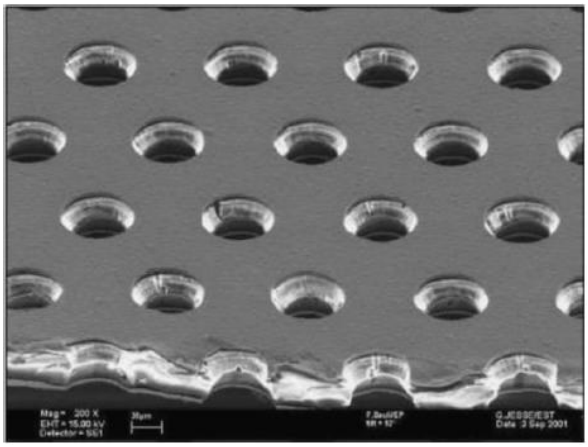

Figure 1: Microscope image of a GEM foil 50 microns thick, with hole pitch of 140 microns and diameter of 70 microns. [1]

The negative signal on the anode of the detector is generated only by electrons collected from the operation of the detector. Without contribution from positive ions as in previous detectors, this allows GEM detectors to be potentially very fast while minimizing space charge problems. There also was a reduced probability of discharges [1]. A similar alteration regarding the holes is done to a similar benefit in Thick GEMs.

Thick GEMs are known as such because they are significantly thicker versions of GEMs, made of sturdier materials. They are typically manufactured using standard printed circuit board production techniques. Benefits of THGEMs include that they can be built to be robust; they can be produced significantly cheaper than standard GEMs and can produce comparable gains while maintaining moderate localization resolution, as well as having high-rate capabilities and fast signal production [4]. The mechanical properties of THGEMs, with their thicker supports, has shown them to be useful for applications requiring large area and

rigid electrodes, such as photosensitive detectors and cryogenic devices [2]. Instead of a double conical hole shape as in standard GEMs, however, clearance rims, regions around the holes free of metal, are used, which will be discussed later. These rims can have significant effects on the gain, as well its long-term behavior under irradiation [2].

In a typical GEM detector, there are three of these GEM foils, separated by spacers at predetermined distances. A High Voltage Divider is designed based on these separation distances. This HV divider is a convenient set of resistors used to apply the proper potentials across the different foils. Typical configurations are the so-called “3-2-2-2” or “3-1-2-1” configuration, which are the numbers representing the gaps in millimeters between drift and the nearest (first) foil (drift gap), the first two foils, the next two, and between the final foil and the readout anode, called the induction gap, respectively.

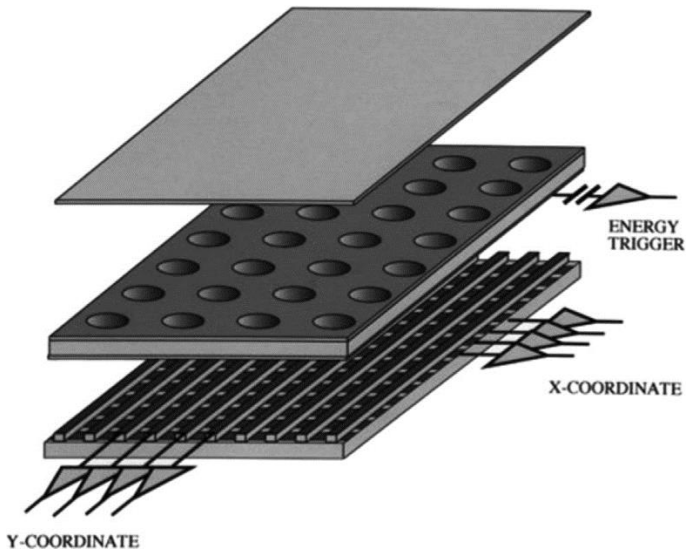

Figure 2: Sketch showing from top to bottom the drift foil, drift gap, GEM foil, induction gap, and readout [1]

Figure 2 above shows an example of a single GEM detector layout. From top to bottom we see the drift foil, drift gap, the GEM foil (for a triple GEM you would have three total foils and two additional gaps in place of the depicted single GEM foil), the induction gap, and the readout anode.

A large potential difference is applied between the two faces of the GEM foil, creating a high electric field in the holes. Electrons from (in our case) the argon atoms within the gas contained in the detector, freed by ionization caused by an incoming particle, drift toward the GEM by an electric field produced by the potential difference between the drift foil and the top GEM electrode. As the electrons near the GEM, they are accelerated by the strong electric fields of the holes toward and into the holes at sufficient energies as to cause further ionization of argon atoms. This results in an electron avalanche. A large number of these electrons then transfer into another multiplying section or, guided by an electric

field in the induction gap (formed from the potential difference between the bottom of the final GEM electrode and the “readout” anode), transfer to a collection electrode (the anode). The signal of the detector is read out from the anode, while the positive ions “drift” in the direction of the electric field vector towards the “drift” cathode, thus the naming conventions [2, 3].

The freed electrons drift and are accelerated through the holes of the GEM foil, such as those of Figure 1, due to the high electric fields brought about by the high potential difference applied between the two faces of the foil [2]. High electric fields (for example, Figure 4) cause electrons to gain greater and greater energy between collisions, allowing for the production of inelastic phenomena and excitation. The atoms of Noble gases, such as argon, de-excite via photon emission, while gases such as CO_2 can dissipate energy without the production of photons, which is important for achieving high gain in a stable way. High electric fields also increase the probability of ionizing collisions, which results in electron-ion pairs, with the primary electron continuing its motion in the gas. These electrons then go on to cause further ionization in the neutral gas, which results in a rapid growth of electrons and ions, known as an electron-ion avalanche, which is the method for signal amplification in gas proportional counters [3].

In the case of a multi-GEM chamber there are typically three stages of these GEM foils, where at each stage the electrons are further accelerated, increasing the total ionization of the gas throughout the chamber (as in Figure 3). This multi-stage

process was inspired by the Multi-step Avalanche Chamber [2], which showed that discharges could be better avoided by operating multiple individual electrodes at a level below the critical gain for discharges, while still producing a sufficiently high overall gain from their combined operation. The moderate fields within both the transfer gaps (gaps between multiplying electrodes) and induction gaps (gaps between sensing electrodes) also reduces the probability of discharges [2].

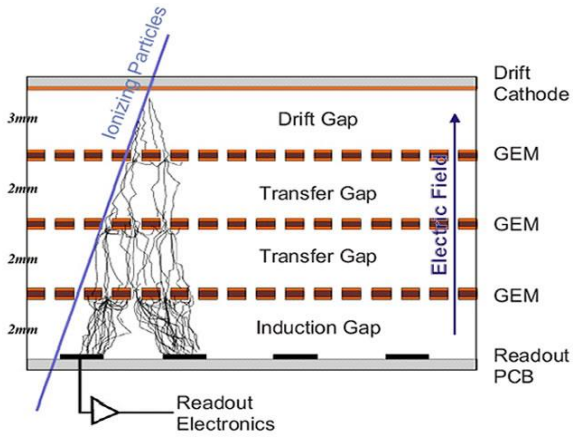

Figure 3: Triple GEM configuration [5]

Ultimately, the total accumulation of electrons that reach the collection anode, connected to the readout electronics, produce a far greater signal than what would have been produced by the incoming particles without the electron avalanche. This increase in signal response is known as "gas gain." For GEM detectors, it is possible to achieve gas gain on the order of 10^4 – 10^5 (though this is not typical). It has been found that high gains can be found at lower voltages in multi-GEM setups than in single-GEM setups, as each GEM foil in the multi-GEM setup contributes toward the overall gain, allowing lower potential differences

across each individual GEM foil, while still achieving similar results, which improves the reliability of the detector [3]. After ionization, the remaining ions then drift towards the drift cathode.

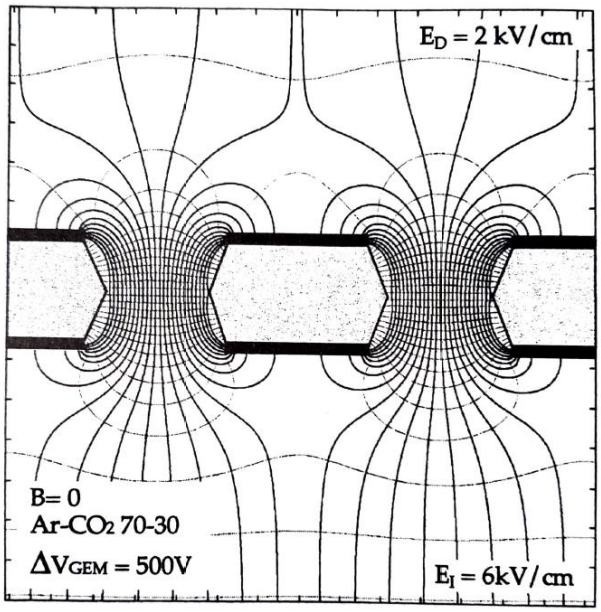

Figure 4: The electric field within the holes of a typical GEM foil in typical operating conditions [3]

Gas gain can be measured by irradiating the THGEM with X-rays and measuring the current and trigger response rate off of the readout board. These values are also taken without the X-ray source. Being a multiplication factor defined as the ratio of the current at a given voltage to the constant value before multiplication, the gain is then given by:

$$G = \frac{I}{eNR} \qquad \text{(Equ.1)},$$

where G is the gain, I is the absolute value of the current taken at a given voltage, e is the elementary charge, N is the number of primaries, and R is the

incident rate. The gas gain is important because it allows the detection of small amounts of primary charge, which otherwise would not be detectable [3]. GEM-based detectors using Argon/CO_2 provide fast particle detection efficiencies near 100%, localization accuracies of approximately 70 um rms, and 10 ns resolution, with the readout electrode being able to be patterned however desired, including zig-zag and straight strips [3].

The overall gain of a multi-GEM structure is a product of the gain due to each GEM foil. When transfer efficiency is taken into account, this is called "effective gain (see Figure 5)" [3].

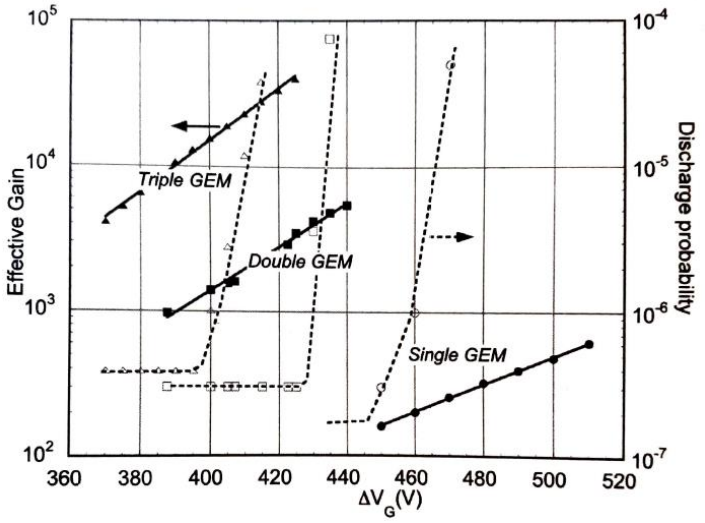

Figure 5: Gain (solid) and discharge probability (dashed) for different GEM configurations [3].

Electric fields greater than a few kV/cm allows electrons enough energy to engage in inelastic collisions and produce ionizations. The electrons in their collisions release energy equal to or greater than their excitation energy, leaving the now excited atom or molecule (for a Noble gas) to de-excite by emitting a photon.

The addition of an organic vapor in the gas mixture allows dissipation of energy without the creation of photons or ions, which is useful in certain types of detectors [3].

There are several gas mixtures which have been used within GEM detectors to serve as the medium in which the ionization and signal amplification would occur. One of these gasses is CF_4, which can achieve very high gains and a high time resolution [3]. Another common gas mixture, which is used in our lab, is Argon-CO_2, in our case 30% Argon and 70% CO_2. Argon serves as the gas that will be ionized by collision with electrons, with CO_2 serving as a quenching gas. As a quenching gas, the CO_2 prevents the argon ions from neutralizing at the Drift in an excited state, avoiding the further discharge effects which could occur if the excited ions were to directly land on the Drift, leading to error in the measurements [6]. Argon-CO_2 is non-flammable and allows for fast particle detection efficiencies near 100%, with localization accuracies around 70 microns rms and 10 ns resolution [3]. The high precision tracking capability of GEM detectors opens them up to wide varieties of applications, particularly as tracking detectors.

One type of GEM detector readout anode pattern is the “square pad” pattern. A printed circuit board (PCB) which implemented this pad pattern was developed at the High Energy Physics Lab A of Florida Tech under Dr. Marcus Hohlmann by Elizabeth Starling, Dr. Aiwu Zhang, and with my own contribution. In this design, as can be seen in Figure 6 below, each square pad connects to a trace which leads to

a pin on a signal connector (Panasonic Co.), which allows for electron counts as well as the current from the readout of the detector to be collected. The electrons, along with their positional information within the grid are then able to be processed analyzed.

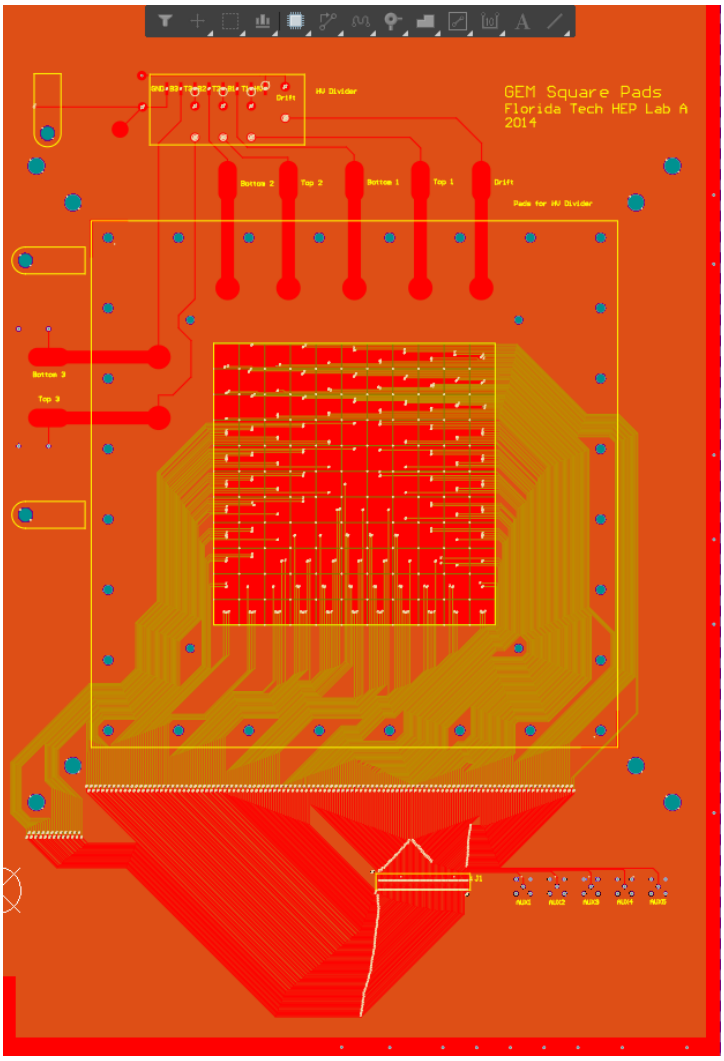

Figure 6: Collection electrode in square pad pattern viewed in Altium Designer. Each pad is 9 mm × 9 mm. The circuitry in the top left provides sites for mounting resistor chains, typically in the consolidated form of an "HV Divider," as well as the mounting of protection resistors.

One type of GEM detector is the Thick GEM (THGEM). Thick GEMs are known as such because they are significantly thicker versions of GEMs, made of sturdier materials. They are typically manufactured using standard printed circuit board production techniques, including the formation of holes through drilling. Benefits of THGEMs include that they can be built to be robust; they can be produced significantly cheaper than standard GEMs and can produce comparable gains while maintaining moderate localization resolution, as well as having high-rate capabilities and fast signal production [4]. The mechanical properties of THGEMs, with their thicker supports, has shown them to be useful for applications requiring large area and rigid electrodes, such as photosensitive detectors and cryogenic devices [2]. Instead of the double conical hole shape of standard GEMs, clearance rims (such as those that can be seen in Figure 7 below), which are regions around the holes free of the metal which otherwise covers the full surface of the active area of the THGEM board, are used. These rims can have significant effects on the gain, as well its long-term behavior under irradiation [2]. The holes of THGEMs are also larger than in standard GEMs. For the purposes of this research a 10 cm × 10 cm Thick GEM was used.

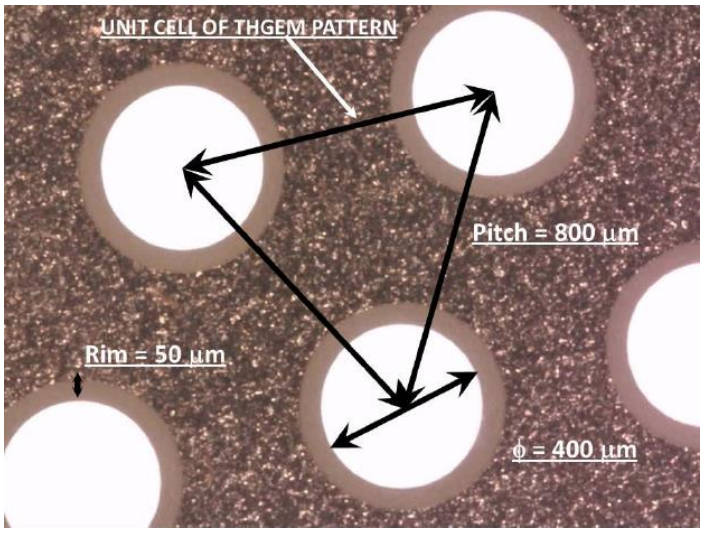

Figure 7: Thick GEM parameters [7]

For this study, instead of PCB production techniques, the THGEM was formed through 3D printing, the print job being outsourced to the company Nanodimensions. With the standard production methods, the rims around the holes would be formed through copper etching. In our case, we were able to include these clearances around the holes within the design, which was made using the software Altium Designer.

Chapter 2

Thick GEM Designs

For the purpose of producing the digital model of our Thick GEM (THGEM) designs, we utilized the PCB designing software Altium Designer. All versions of the THGEM which were ultimately produced were designed within this software, which is able to output files in various formats useful for PCB manufacturers as well as 3D printers.

Initial Design

The production style of THGEMs, the composition materials, as well as the use of clearance rims instead of double-conical holes are the primary differences between THGEMs and standard GEM foils. The other factors are largely the same, including the hole diameter-to-thickness ratio being (typically) 1:1 in both models.

The design of a THGEM depends heavily upon the motivations for the study. Early in the process, our motivations became to determine which hole configuration would produce the optimum results, i.e. yield the greatest gain. This led to the production of a “sampler coupon” board design, with a 9 cm × 9 cm active area region. This design had six sets of hole diameters, as shown in Figure 8.

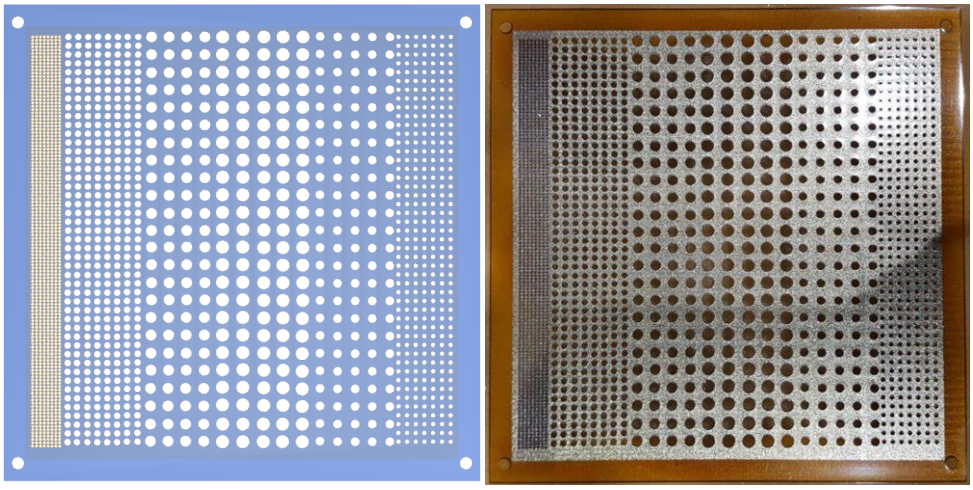

Figure 8: (Left) 3D Altium Designer view of board model; (right) printed version

The hole diameters for this model were, in millimeters, 0.5, 1.5, 2.5, 3, 2, 1, from left to right, as shown in Figure 8 above. This configuration was done such that when installed in a detector with an anode connected to readout electronics, and only a particular region irradiated, gain information connected to the distinct regions of the board would be found, which would allow us to determine which particular configuration in use with a gas mixture of Argon (70%) and CO_2 (30%) would yield the greatest gain.

After receiving the produced version of the board, several challenges appeared, through a combination of design oversight and problems inherent to the production.

Figure 9: (Left) Overall glossiness of the board; (Right) Microscope image

As seen in Figure 9, there appeared a glossy layer covering what should have been a bare silver layer of the board. This was shown to be some additional substance coating the silver in the microscope imaging. This was due to an unnoticed default application of a solder mask over PCB designs in the Altium software, which, for our purposes, would not be acceptable. With this solder mask applied over the conductive layer, there was no point of electrical contact which could be made to power the board. In an effort to at least be able to make proper connections and apply a bias voltage (as well as do proper tests for any shorts on the board) a carbide tipped scriber was used to physically remove the material.

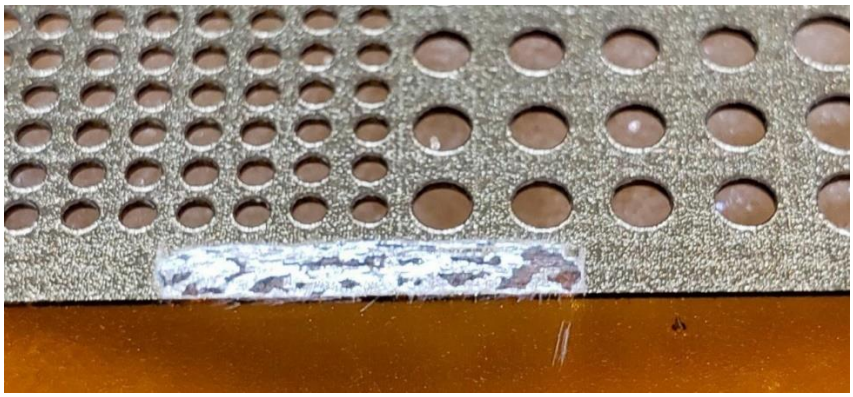

Figure 10: Scriber revealed the shiny silver layer underneath the mask

An ohmmeter (within a digital multimeter) was then used to show that this layer was indeed conductive, which then meant presumably that newly exposed regions like the one shown in Figure 10 could be used to carry the potential across the full surface of the board.

There was another issue with the board, however. It was found that within the design, there was a push-back against the solder mask material around the holes that made up the 0.5 mm region of the board that was added by default, leaving it the only region which had a conductive surface exposed already. Unfortunately, these holes were also marked to be through-plated, which presented a critical design flaw, as it shorts out.

Perhaps fortunate in hindsight, due to the small pitch of the holes, the thinness of the material, and other factors, this 0.5 mm region developed a separation along the length bordering the other regions of the board. This severing, combined with the fact that that region was causing a direct shorting of the board, meant that that entire sector needed to be removed, as seen in Figure 11.

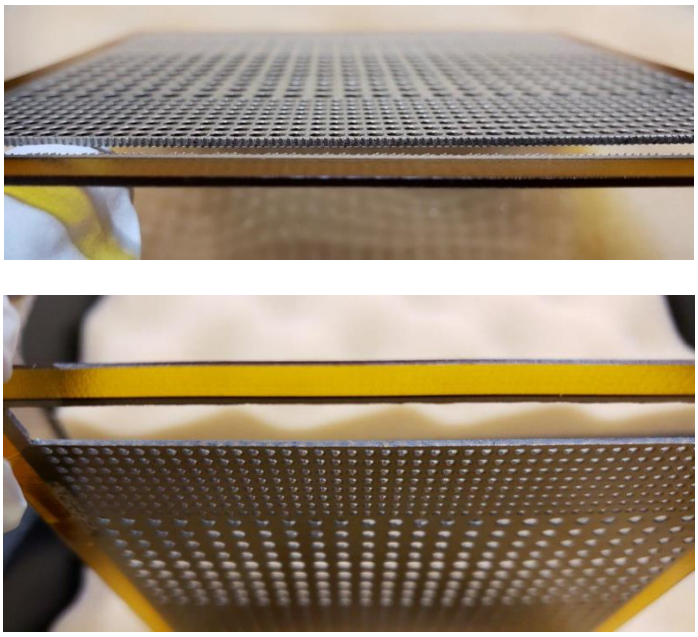

Figure 11: Troubled sector removed (top); metallic border shaved away (bottom)

After that sector was removed, there still remained some of the metallic plating that existed in those bordering holes. Using an X-Acto knife, that region shaved down until only the plastic dielectric material remained. Testing using both a multimeter and a Giga-Ohmmeter (Megger) suggested that there was still some connection between top and bottom. It was likely due to slight amounts of metal on the inside of the holes in other sectors. This was not due to any designed plating, but simply a product of the 3D printing process.

The last major issue with this THGEM board was the hole shape. There often existed printing artifacts consisting of extra pieces of silver, jagged edges, or more within the holes.

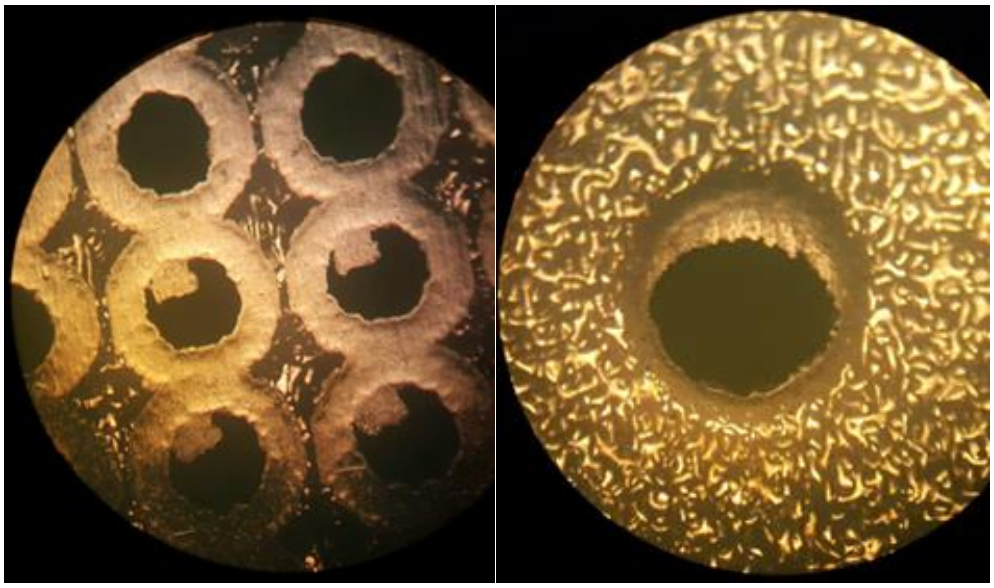

Figure 12: Anomalies involving the holes in the THGEM board

These errors, combined with any lack of decent circular shape of the holes, could significantly affect the electric field expected in this region of the board. Some errors were repeated on occasion, as in the left of Figure 12 above, whereas other errors were of a different type altogether, as shown in the right.

These errors, combined with the fact that several breaks in the edges of the board occurred while making these corrections, ultimately led to the decision to abandon this board in favor of another design.

Final Design

With the help of an undergraduate member of our High Energy Physics (HEP) group, John "JT" Hammond, a couple of different designs were produced and considered, including versions with tabs or varying trace thicknesses leading to pads on which to mount electrical connections which would be used to power the board. Ultimately it was decided that the design we would go with would be one consisting of a 10 cm × 10 cm active region divided into three equal sectors of approximately 10 cm × 3.3 cm area each. These sectors would have traces leading to pads which would allow them to be powered independently within a "10 × 10 Detector," giving us the ability to have three separate types of THGEMs on one board. This concept is similar to the idea with the coupon before, except now each region is totally separate from the other, as seen in Figure 13 below.

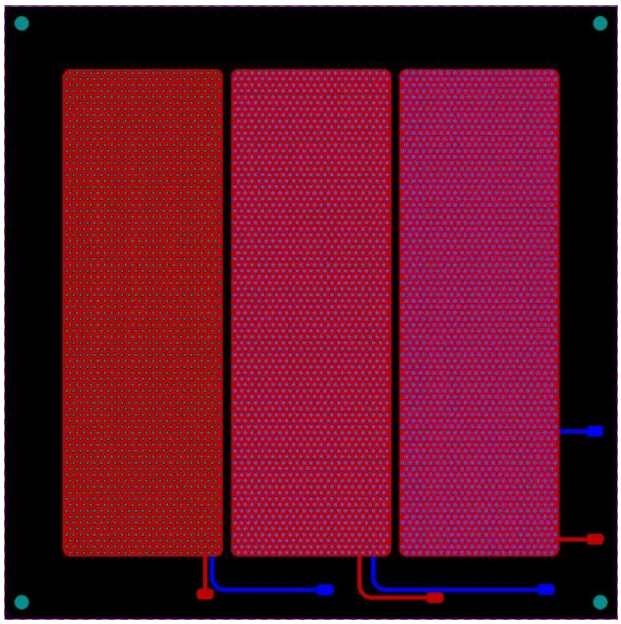

Figure 13: View of the new THGEM design within Altium Designer

This new design was largely due to new motivations for testing, inspired largely by a paper by Alexeev et. al. Studying their paper [7], along with others, resulted in our decision to make all holes in each sector 0.7 mm, with a pitch of 1.4 mm. The board thickness was designed to be 0.7 mm as well. This is on the larger side for THGEMs, as standard ones have a PCB thickness of 0.2-1 mm, hole diameter of 0.2-1 mm, pitch of 0.5-1.2 mm, and rim width between 0 and 0.1 mm [7]. An example is shown in Figure 7 above.

Rims were included in this design and became the defining difference between the three sectors of the overall board. Studies have indicated that these holes provide not only similar function to that of the double-conical hole design of standard GEMs [3], but differences in rim annulus size can also affect the overall effective gain of the detector, as well as the time evolution of the gain [9]. Based on

the information in the aforementioned papers, it was decided that the rim annulus sizes would be zero (no rim), 0.1mm, and 0.18mm. This would enable us to do several different studies using the same 3D-printed board.

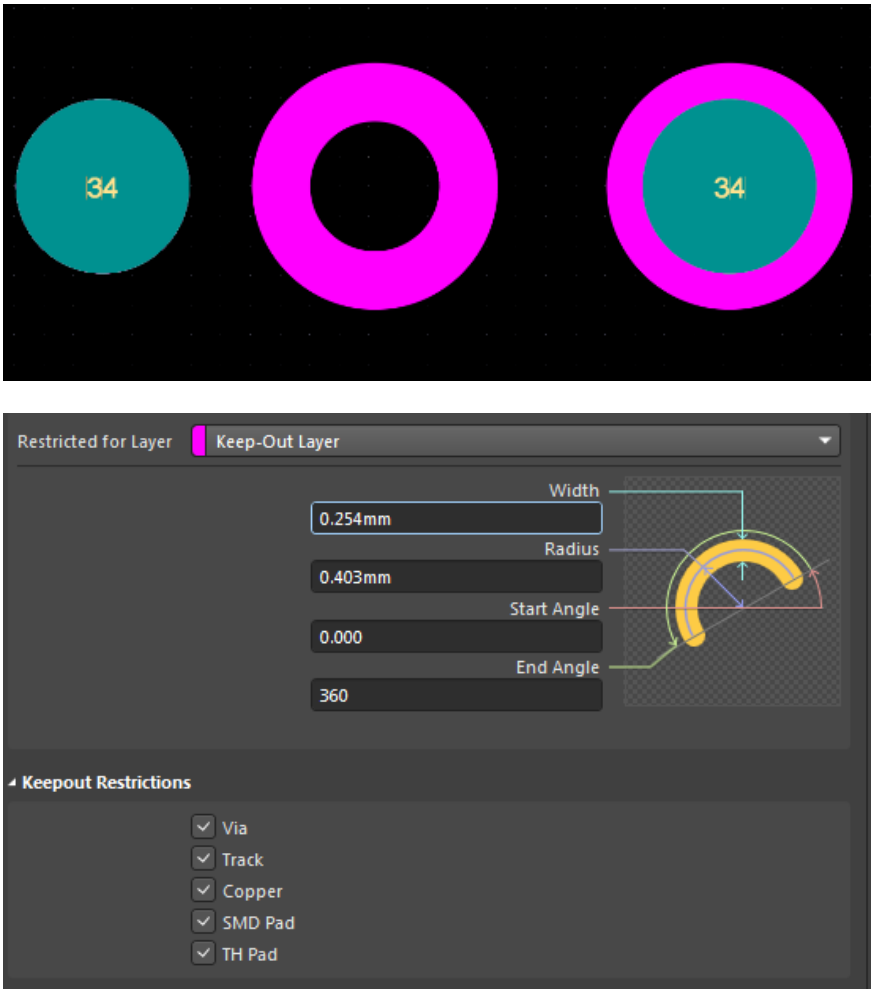

Figure 14: Method for producing rims within Altium Designer. The circle labeled 34 in the top image is the physical hole, the pink ring is the defined "keep-out" region. Its width is doubled in the definition, but the excess is consumed within the hole.

One issue in the designing phase of this version of the THGEM was how to produce these rims accurately within the software. Ultimately the method found was to pair the non-plated through-hole with an arc that existed on the "keep-out"

layer. This keep-out layer would define the region in which no metal would be deposited in printing. The radius of the arc was determined by the distance from the center point to the middle of the width of the arc line, so that, along with the thickness of the ring and the hole diameter, had to be taken into account in calculating the exact parameters which would ultimately define the rim annulus. This technique, as well as arc definitions leading to a 0.18 mm rim is illustrated in Figure 14 above. That method did indeed result in visible rims within the 3D view of the THGEM design in Altium, as seen in Figure 15 below. Unfortunately, with the arrival of the printed version of this design, it was found that the solder mask had still mistakenly been applied.

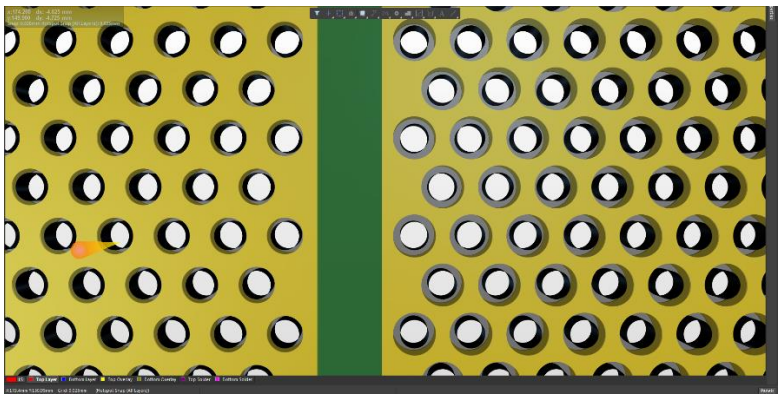

Figure 15: Rims now clearly visible within the design, and with different sizes: 0.1mm (0.18mm) on the left (right) sector

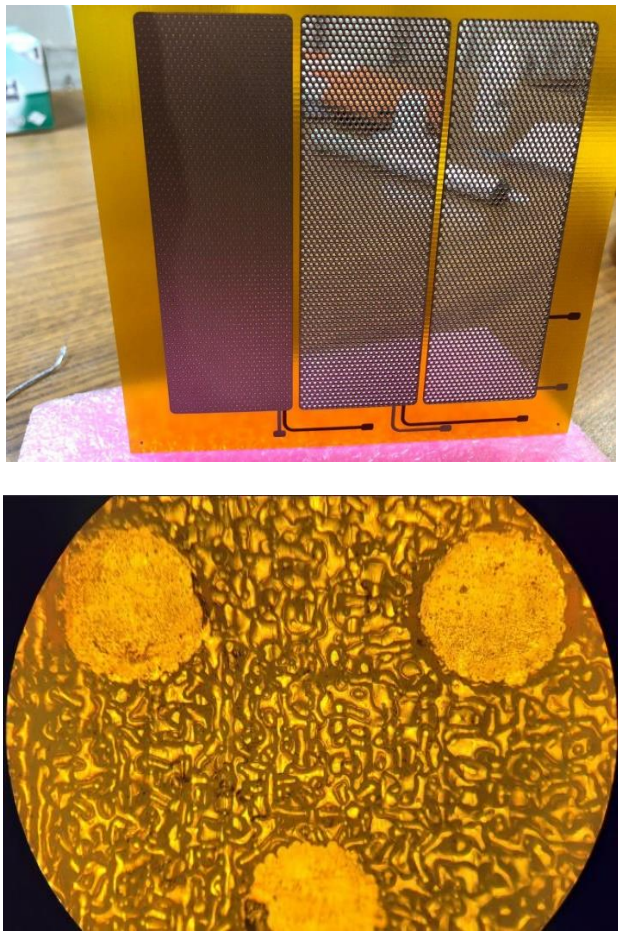

Figure 16: Room light as observed through the THGEM (top). Total clogging of no rim holes with insulating material (bottom).

This insulating layer was across the whole board, except curiously in occasional patches on the surface, as well as a scratch on one of the pads, where, using an ohmmeter, it could be shown that there was electrical connectivity. The problem was particularly extreme in the region with holes designed to have no rims. As can be seen in Figure 16, those holes were completely clogged with the insulating material. The manufacturer was then contacted and, working with them, it was explicitly ensured that no mask was called for in the design, and that they

understood not to add any in production. We then ordered another print out of this now corrected THGEM design, which can be seen in Figure 17 and Figure 18 below.

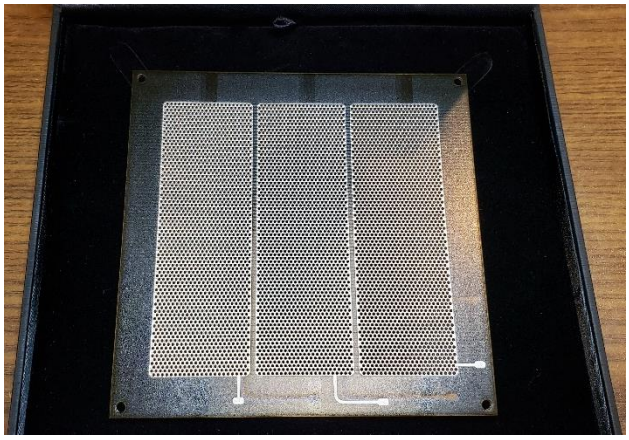

Figure 17: Mask-Free THGEM delivered

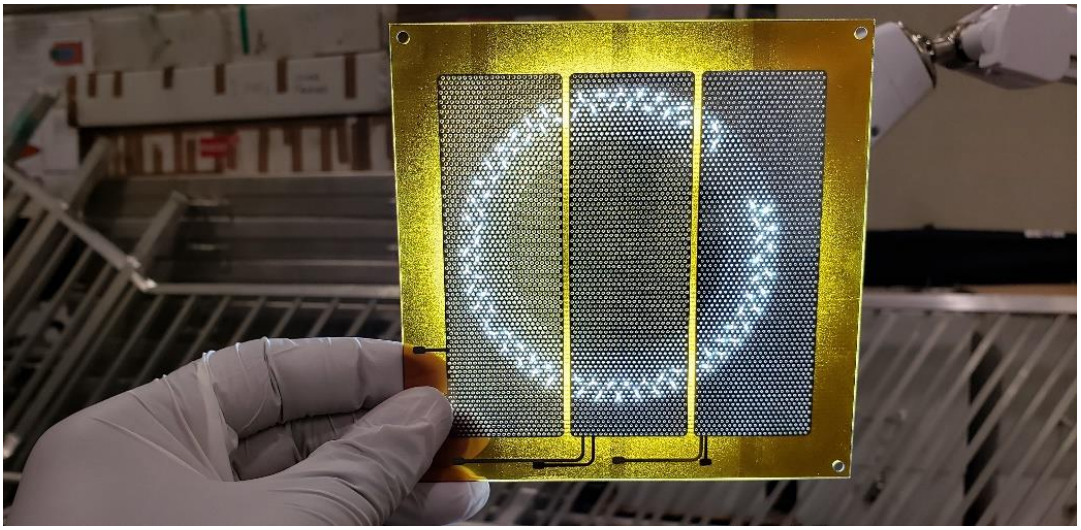

Figure 18: Light clearly passes through unhindered

Finally, a version had been produced which was conductive over the entire surface, front and back. With continued assistance from Omar Nour, an undergraduate member of the HEP research group, a microscopy investigation was

conducted on this board, to confirm adherence to the design specifications, as well as to quantify any discrepancies.

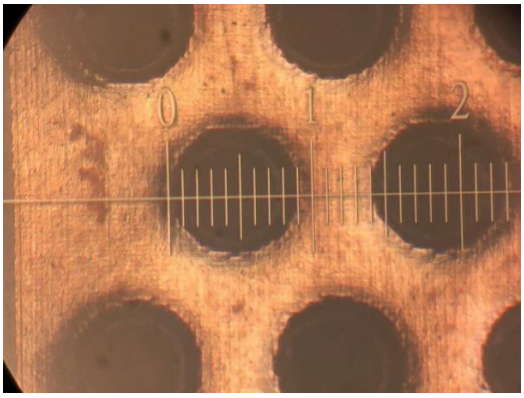

Figure 19: Holes designed to have no rims

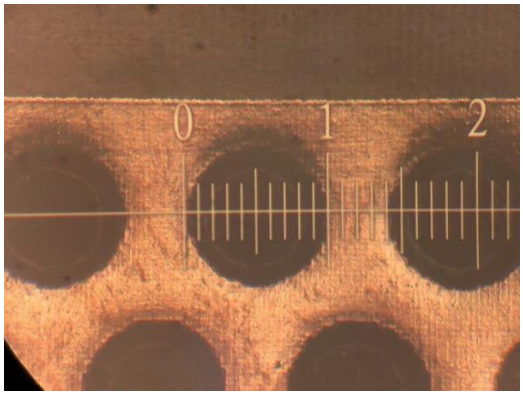

Figure 20: Holes designed to have 0.1 mm rim annulus

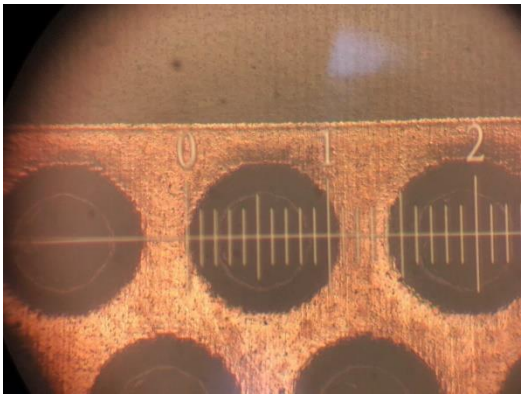

Figure 21: Holes designed to have 0.18 mm rim annulus

What can be immediately seen in the images of Figure 19-21 is the lack of any of the wavy material which was present in all previous microscope images. In addition to that, the holes, along with their distinctly visible rims, all appear to be fairly regular and free from any of the printing anomalies of previous versions, including the initial print of this same design. From that it can be concluded that the application of the solder mask played a significant role in producing many of the irregularities related to the holes and rims in previous versions. The silver layer is clearly visible with both the naked eye and in the microscope images. It was also confirmed with ohmmeter testing to be conductive everywhere.

As for the adherence of the hole and rim dimensions to the design parameters, each hole was found to be 0.7 mm as intended, however the rim sizes were not to specification. Instead of 0 mm, 0.1 mm, and 0.18 mm rim annuli, what was received was found to be 0.1 mm, 0.15 mm, and 0.2 mm rim annuli, respectively. A close up of the THGEM sectors which contain these holes with their associated rims is shown in Figure 22 below. Our investigation possibilities, chief of which was determining whether or not a 3D printed thick GEM could be used to produce a functioning particle detector, would not be significantly hindered; however, the parameters of the actual board would have to be taken into consideration instead of the design parameters.

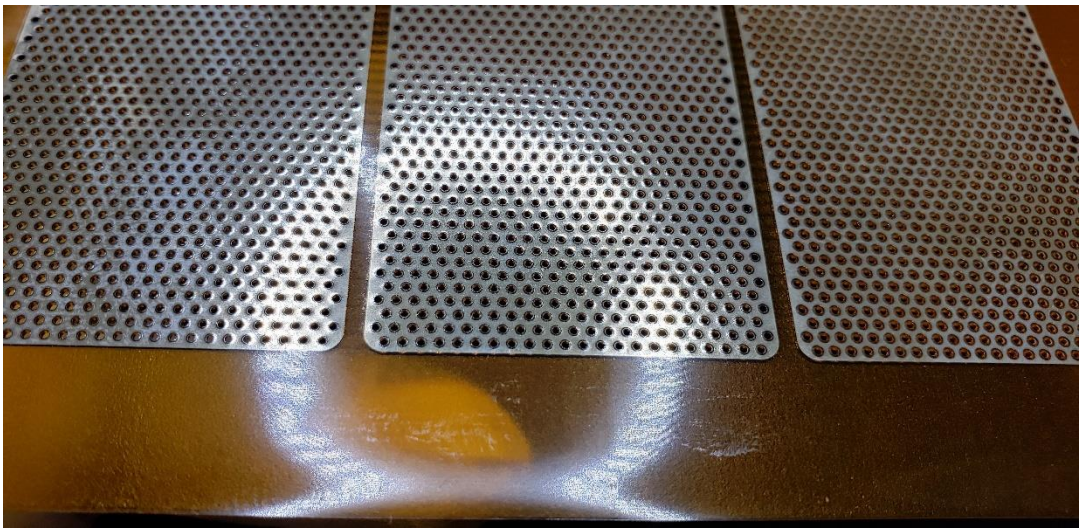

Figure 22: Close-up of three sectors with rim sizes (from left to right) of 0.1mm, 0.15mm, and 0.2mm.

Chapter 3

Assembly

The THGEM board itself is of course only one component of the overall system of equipment needed to produce a functioning detector. The required components, including the drift and readout boards, have been discussed in the introduction. In this section, the assembly of the full detector, which combines these components, will be discussed.

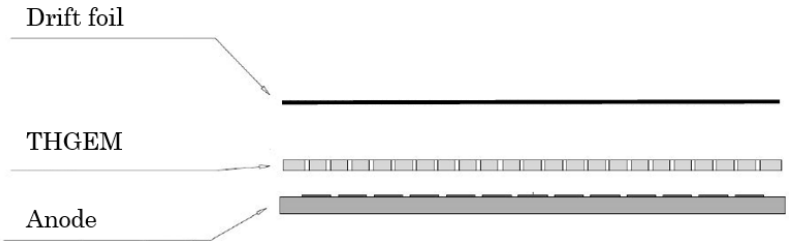

Figure 23: A graphic depicting a typical single THGEM detector setup [7]

Taking inspiration from the "3-1-2-1" configuration of the CMS GEM detectors, it was decided that the drift gap between the drift cathode and the top of the THGEM would be 3 mm. The induction gap between the anode and the bottom of the THGEM would be 1 mm. An example of a similar electrode stack can be seen in Figure 23 above.

A few mechanical challenges presented themselves during this stage of the process. One of the traces supplies HV to the top of the THGEM was determined to

be non-functional, so it was replaced with a copper tape version of the trace, as shown in Figure 24.

Figure 24: Copper tape trace in the center

Additionally, a method for physically connecting the THGEM to the HV system of the detector had to be found. Wires were considered to be too thick, so it was planned to use copper tape strips soldered onto the contact pads on the THGEM instead. Eventually it was discovered that, likely due to the thickness of the solder point, the heat required in its application, the thinness of the silver layer, the mechanical tension on that connected point, or some combination of those things, caused the connection to the THGEM board to break every time the detector was closed, particularly on the "THGEM Top" electrode. Specifically, the point where solder met the silver trace would break connection, often resulting in silver peeling off of the underlying dielectric material all together at that spot (see Figure 25 below). This also sometimes occurred with the application of heat or pressure.

In order to establish an electrical connection which could be trusted to be maintained even when the detector was fully closed, the use of solder directly on the THGEM board to connect the copper tape strips to the board pads and traces was abandoned. The connection would then be made purely by taking advantage of the copper tape and the conductivity of the associated adhesive. Kapton tape was added to reinforce the security of the copper tape, as well as to add additional insulation.

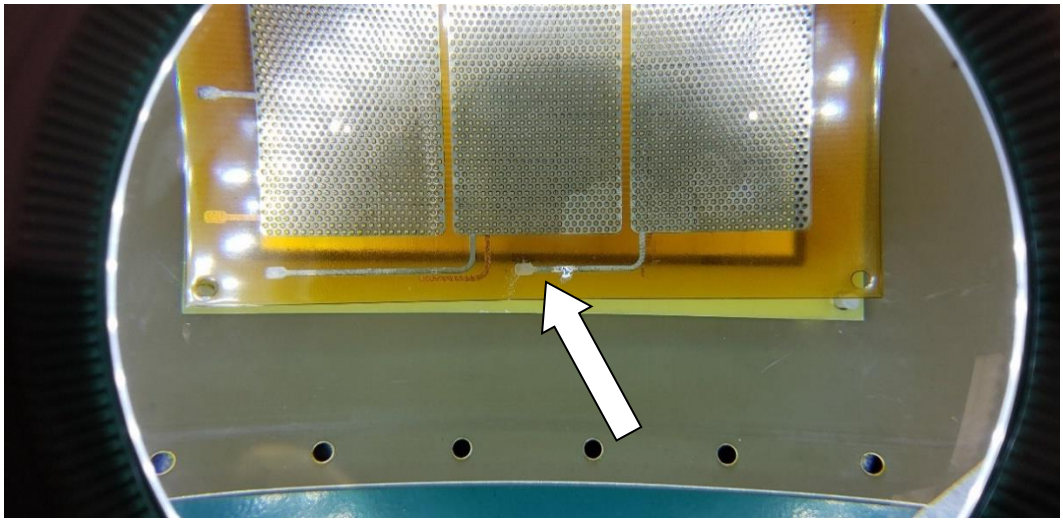

Figure 25: Exposed plastic material where there once was silver trace. Solder remaining after attempted removal can also be seen.

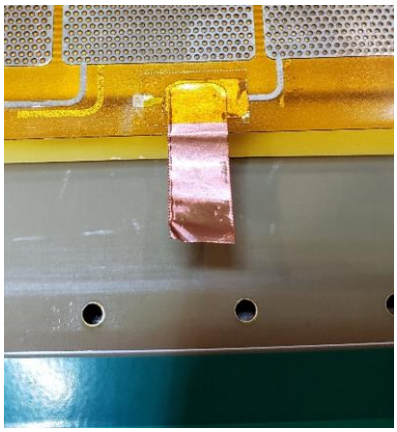

Figure 26: Adhesive copper tape strips covered with adhesive Kapton tape used to power the board

For the bottom of the intended 0.1 mm sector of the board, hereafter called Sector 1 or “small rim” sector, there remained still enough trace on which to mount the copper tape strip shown in Figure 26. As the trace for the top of Sector 1 was much shorter, and had several more issues than the bottom, this trace was all but gone completely. Therefore, in order to power this area, the copper tape strip had to be adhered directly onto a small portion of the active area of the board, as seen in Figure 28 below. All of these connections were tested and found to be in good condition regarding electrical conductivity.

Before the assembly, an “L-shaped” HV board was installed to the readout board, which allowed us to bypass any issues involving delivering high voltage to the equivalent HV pads and traces native to the readout board itself. Those portions of HV circuitry, as shown at the top of Figure 6, were deemed unreliable, so their use was avoided. By implementing the “L-shaped” board, the setup was functional, reliable, and made more convenient for mounting HV connections.

The assembly process was then relatively straightforward. The readout board contained the anode and all traces which led to the Panasonic connector which allows for measurements. On top of that, contained in the four corners by nylon threaded rods, a one-millimeter square spacer was placed, as shown in Figure 27. On top of this, the THGEM board was placed. The nylon rods had previously been shaved slightly to allow better fitting. On top of the THGEM board, three sets of 1 mm washers were placed in each of the four corners, around the nylon rods. This created the 3 mm gap between the THGEM Top and the Drift (Figure 29), which was installed next. These features can be seen in Figure 28. A red HV wire within the gas volume, as can be seen in Figure 27, connected the connection tab on the drift to its proper connection on the readout board, which was necessary due to design differences between this readout board and the one for which this drift foil was originally designed. Smaller red wires (Figure 31) then connected these traces on the readout board to their proper positions on the "L-shaped" HV Board where, through 10 MOhm protection resistors, we were able to power each electrode independently (meaning the Drift, THGEM Top, and THGEM Bottom). This ability to power each electrode independently gave us full control over each electric field. This stack was then locked down using nylon nuts on the nylon rods, and around the system was placed an outer frame (Figure 30), equipped on top and bottom with three-millimeter diameter Viton™ O-rings. The cover, which contains

built-in closing nuts, was then placed atop the outer frame, and the closing screws were installed (Figure 31). The parts were cleaned using a silicon roller at each step.

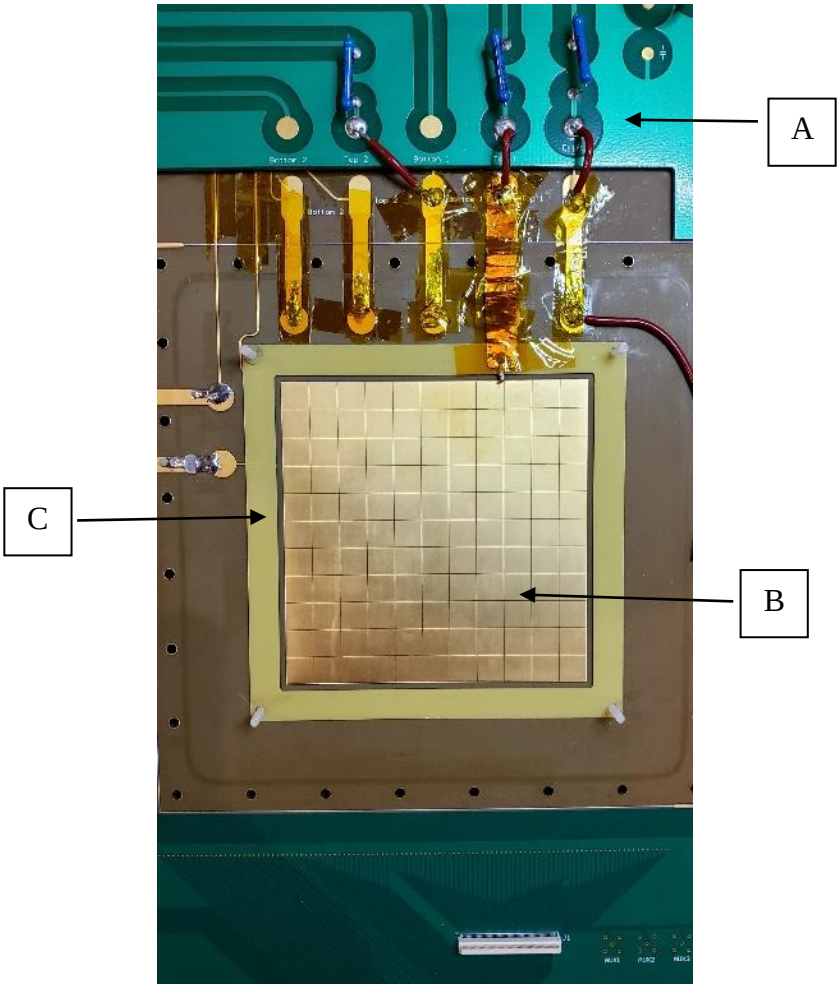

Figure 27: HV board (A), anode (B), and induction gap spacer (C) shown

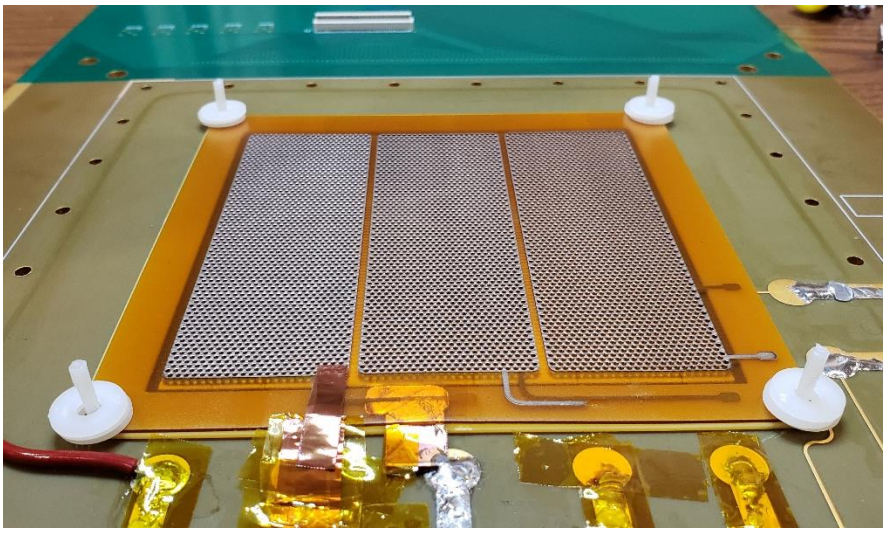

Figure 28: THGEM Board installed; three 1 mm washers placed in each corner that define the drift gap

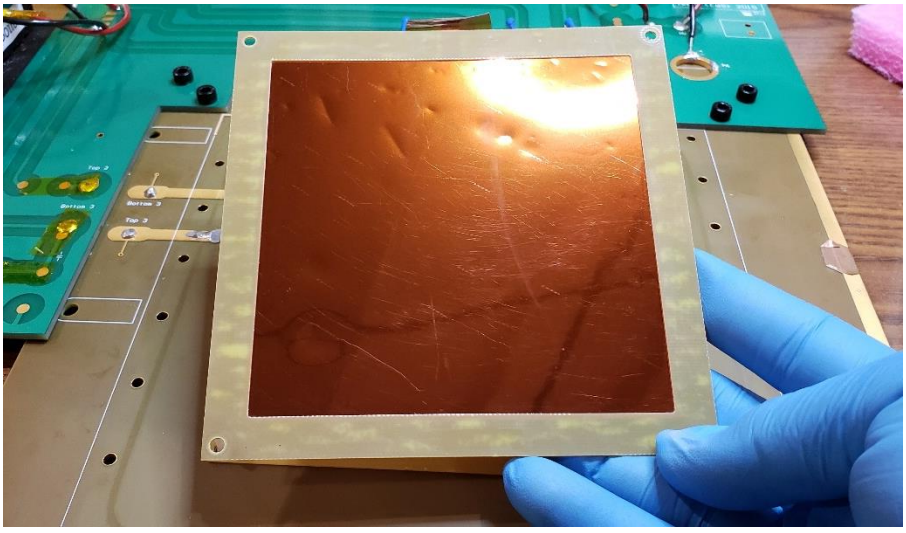

Figure 29: Drift Foil Cathode

Figure 30: Outer Frame with O-rings

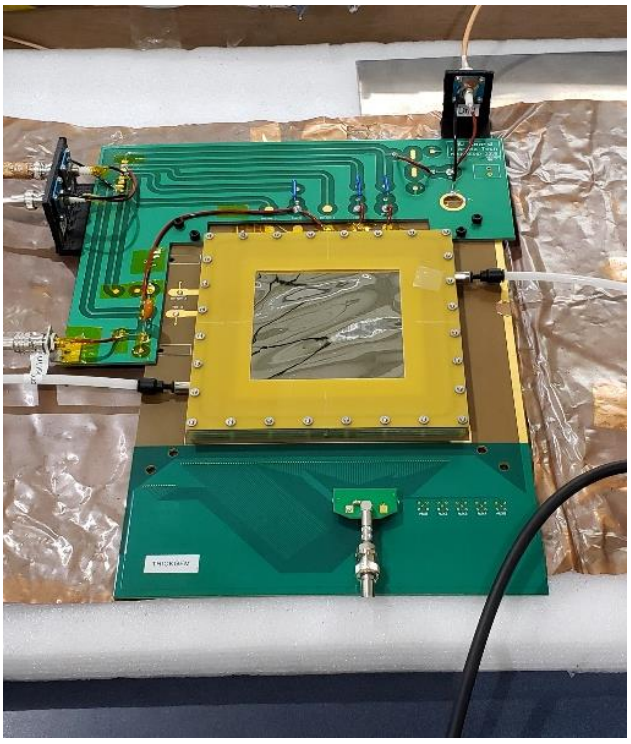

Figure 31: Fully assembled detector with various HV connections and gas inlet and outlet tubing

Readout Electronics Chain

With the detector fully assembled, the next step of the process was to begin testing. The schematic shown in Figure 32 below depicts the readout electronics chain used during testing. Note that being discussed is a straight strip readout model that will be shown in detail later. This is the model that was ultimately used during testing. The electronics chain for the square pad model is nearly identical.

Three HV channels power the three electrodes of the THGEM. The strips that make up the readout anode within the detector lead to the Panasonic connectors, 128 straight strips in each set, with two sets in the X direction and two sets in the Y direction. In each of these sets, the strips are ganged together in a Panasonic-to-Lemo adapter. For the square pad model, all pads on the readout anode led to a

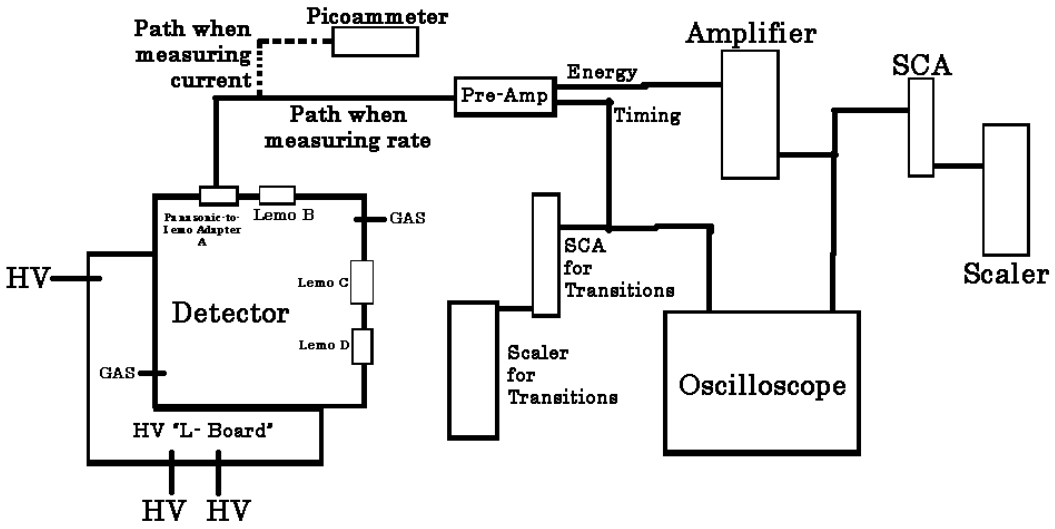

Figure 32: Readout electronics chain used during testing. Note: Energy and Timing outputs from the Pre-amp are just labels; the signal out of both is identical. SCA: Single Channel Analyzer.

single Panasonic, resulting in all pads ganged together in the Panasonic-to-Lemo adapter. For the straight strip model, an appropriate choice in which adapter to use is made, and a Lemo-to-BNC connection is added, carrying the signal to a pre-amplifier in the case of rate measurements, or to a picoammeter in case of current measurements. The pre-amplifier has two identical output channels called Timing and Energy. The timing channel is split and connected to an SCA leading to a scaler for counting large positive-to-negative transitions and potential sparks, and to the oscilloscope. The energy channel is sent to an amplifier, whose output is split to an SCA leading to a scaler for counting signal triggers, and to the oscilloscope.

Before any official HV testing can be conducted however, it is important to get the noise levels down below a certain level, typically with a trigger threshold under 190 mV as measured by an oscilloscope, in our case a LeCroy WaveRunner 104Xi-A. Various techniques are used to accomplish this, the primary one being to ensure proper grounding, and to utilize copper shielding. Sheet copper, copper tape with conductive adhesive, and braided metal strips were all used in the fight against the noise levels of the detector, and its associated pre-amplifier. Eventually it was considered that perhaps the cause was due to a high capacitance between adjacent square pads on the readout, or between the pads and the board. The total input capacitance, which was measured between the signal pin of the Panasonic-to-LEMO adapter and the ground of the board, was also tested. All the capacitance levels seemed reasonable, being tens of picofarads for the case of individual pads,

and under 200 pF for the input capacitance of all pads ganged together. Nonetheless, it was decided that it would be worthwhile to change the readout board associated with this detector, in order to reduce the noise levels further. The THGEM board and Drift foil were removed and assembled into a new detector (Figure 33). This detector had a readout composed of two each of X and Y directional straight strips, each set with an associated readout Panasonic for the connection of the electronics. For the purposes of these tests, only one Panasonic at a time would be needed for reading out information, the others would be terminated with 50 Ohm terminators to ground them.

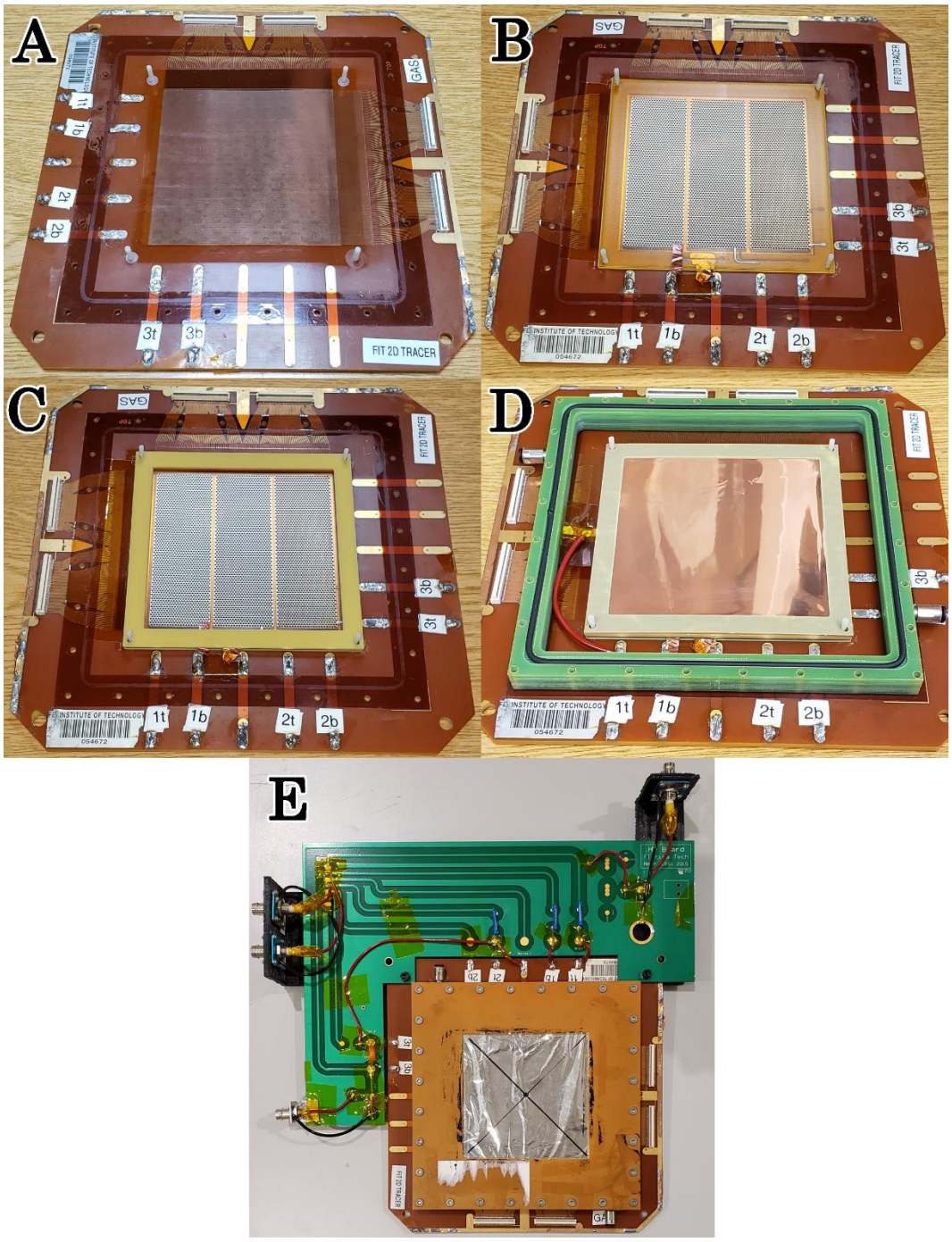

Figure 33: A) X and Y-directional straight strips serve as the readout anode and deliver the signal to the associated Panasonic connectors. B) The THGEM board is installed atop 1 mm washers in each corner defining the induction gap, suspended above the straight strips. C) Three 1 mm frames are placed above the THGEM, which define the drift gap. D) The drift is placed atop these frames, with closing nuts screwed about the nylon posts, thus completing the THGEM stack. E) The fully assembled detector.

These changes nevertheless still resulted in a detector which contained too much noise. The solution was found in switching out the ORTEC 142PC pre-amplifier for an ORTEC 142A. This model contains different capacitors, resulting in the ability of the 142A to accept higher input capacitances than the 142PC, while also having lower noise levels. The noise levels were also reduced by more directly grounding the surface of the pre-amplifier with a metal braid, wrapping it in copper shielding, creating a Faraday cage around it with aluminum foil, and finally, adding a weight on top to ensure good contact between these materials and the pre-amplifier itself. This resulted in noise levels that were well within acceptable range. It was later found that the noise levels could be further significantly reduced by elevating the detector from direct contact with the table on which it had been set, as in Figure 80.

In some cases, the noise levels were so low that they were too low to be picked up by our Ortec 551 Timing SCA. In these cases, such as those tests involving the small and large rim sectors under Fe-55, the gain setting on the amplifier had to be increased from 18 to 27. With the noise finally reduced sufficiently, HV testing could begin.

Chapter 4

Testing

For the purposes of this particular study, the testing of the THGEM Detector was broken down into three main tests: A test to determine if the board contained any shorts, a test to determine the gain for each THGEM sector (and long-term behavior where possible), and a test for any malfunctions regarding the operation of the detector.

To begin, the detector was tested to see if it was able to hold gas pressure at all. It was unable to maintain gas pressure more than a few seconds. It was, however, able to maintain decent output flow compared to input flow (Figure 34), so this would be sufficient when operated with a high gas flow in later tests.

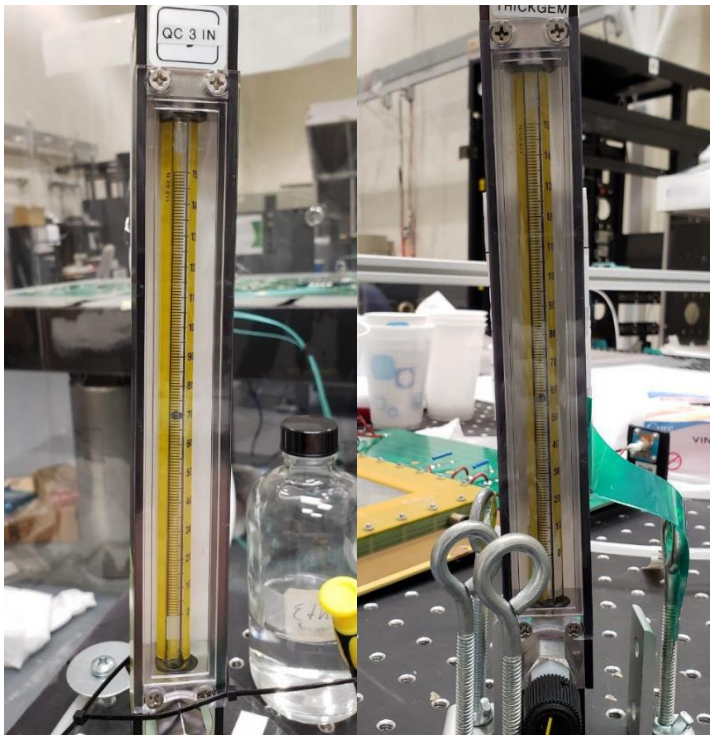

Figure 34: Flowmeters showing input (left) and output (right) flow of nitrogen gas

The test shown above was for the original chamber for this experiment. In the reassembly after the changing of the readout board, the chamber was able to hold gas pressure with similar efficiency as the prior assembly, under both CO_2 and Ar/CO_2.

The first of the main tests was then conducted. This was done with the cover off of the detector, in the original assembly. Using the GigaOhmmeter (Megger), the THGEM was tested across top and bottom, applying 504V for 9 minutes straight.

Foil Name	THGEM				
Test date					
RH %	54.5				
Place	FIT				
Foil Version	3				
Batch number					
User name	Jerry				
Action taken					
Comment	Pressure: 1012.5 hPa, Temp: 24.9C				
QC2 fast					
Time	*Voltage(Volts)*	*Impedance(Gohms)*	*Current(nA)*	*Sparks*	*Sparks*
30s	504	100.00	5.04	0	
1m	504	100.00	5.04	0	
2m	504	100.00	5.04	0	
3m	504	100.00	5.04	0	
4m	504	100.00	5.04	0	
5m	504	100.00	5.04	0	
6m	504	100.00	5.04	0	
7m	504	100.00	5.04	0	
8m	504	100.00	5.04	0	
9m	504	100.00	5.04	0	

Figure 35: Table of Results for Shorting Test

The results of this test, as shown by the data in Figure 35 above, indicate that there is indeed no short in the small rim sector of the board. 504 Volts were applied across the top and bottom THGEM electrodes, resulting in a resistance greater than 100 GOhms, which is the reading we would expect when no short is present.

With the reassembly of the detector, it was decided that this test would be repeated. The test was done for all three sectors of the THGEM board, so as to verify that they are free of shorts all at the same time. The results are shown in the tables of Figure 36 below.

Foil Name	THGEM Small Sector
Test date	
RH %	54.5
Place	FIT
Foil Version	3
Batch number	
User name	Jerry
Action taken	
Comment	Pressure: 1012.5 hPa, Temp: 24.9C

QC2 fast

Time	Voltage(Volts)	Impedance(Gohms)	Current(nA)	Sparks	Sparks
30s	504	100.00	5.04	0	0
1m	504	100.00	5.04	0	0
2m	504	100.00	5.04	0	0
3m	504	100.00	5.04	0	0
4m	504	100.00	5.04	0	0
5m	504	100.00	5.04	0	0
6m	504	100.00	5.04	0	0
7m	504	100.00	5.04	0	0
8m	504	100.00	5.04	0	0
9m	504	100.00	5.04	0	0
10m	504	100.00	5.04	0	0

Foil Name	THGEM Medium Sector
Test date	
RH %	41.7
Place	FIT
Foil Version	3
Batch number	
User name	Jerry
Action taken	
Comment	Pressure: 1007.6 hPa, Temp: 25.8C

QC2 fast

Time	Voltage(Volts)	Impedance(Gohms)	Current(nA)	Sparks	Sparks
30s	504	100.00	5.04	0	0
1m	504	100.00	5.04	0	0
2m	504	100.00	5.04	0	0
3m	504	100.00	5.04	0	0
4m	504	100.00	5.04	0	0
5m	504	100.00	5.04	0	0

Foil Name	THGEM Large Sector
Test date	
RH %	41.7
Place	FIT
Foil Version	3
Batch number	
User name	Jerry
Action taken	
Comment	Pressure: 1007.6 hPa, Temp: 25.8C

QC2 fast

Time	Voltage(Volts)	Impedance(Gohms)	Current(nA)	Sparks	Sparks
30s	504	100.00	5.04	0	0
1m	504	100.00	5.04	0	0
2m	504	100.00	5.04	0	0
3m	504	100.00	5.04	0	0
4m	504	100.00	5.04	0	0
5m	504	100.00	5.04	0	0

Figure 36: Results for all three board sectors indicate that there are no shorts across the THGEM board.

Following this test began a long series of testing to ensure the proper functioning of the board, that a reasonable gain could be observed, and to observe the long-term behavior. Various configurations were attempted in order to discover the various strengths and weaknesses of the detector, and to find the configuration which would deliver results.

In order to confirm that X-rays were getting through to the THGEM board, as well as test how greatly foils reduced the X-ray penetration, a test was conducted which created similar conditions as those of the fully assembled detector. The similarities include the use of the same cover and drift foils, irradiation conditions, and as close as possible matching of the gap distances, including between the sensitive detection region and the drift foil, the drift foil and the cover, and the cover and the irradiation source. This utilized a small portable Geiger counter underneath both the cover of the detector and a drift foil, with 80/20 bars and an outer frame used to recreate approximate the spacing conditions of the closed detector. The X-ray source was placed in a 3D-printed source holder atop the window of the cover and above the sensitive region of the Geiger counter to allow it to collect counts for one minute (Figure 37).

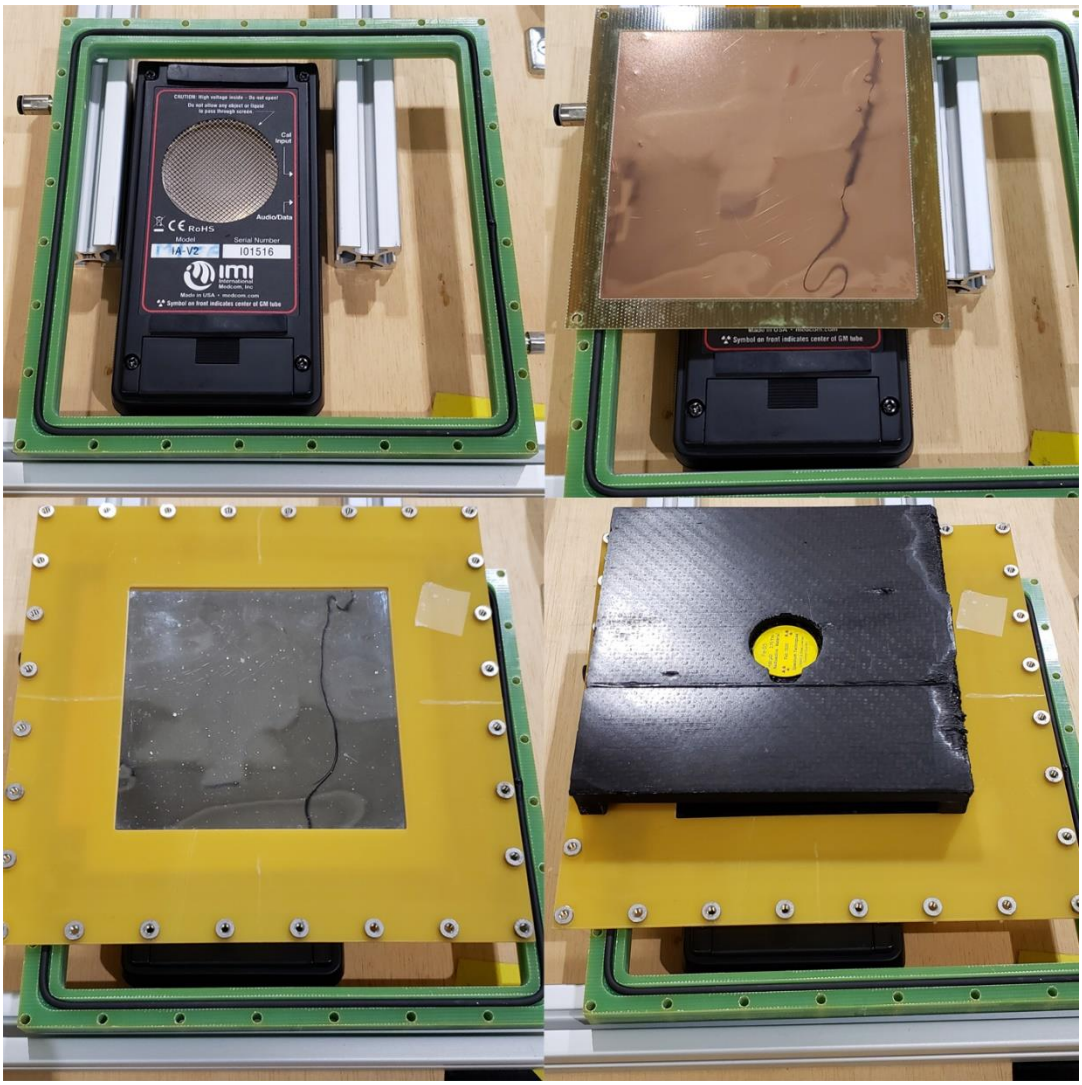

Figure 37: Geiger Counter Test of Cover Window setup

The results of this test showed that without foils, the rates were 31 counts/min (0.52 ± 0.10 Hz) without a source, 100,400 counts/min (1673.33 ± 19.23 Hz) under Fe-55, and 9,138 counts/min (152.30 ± 2.86 Hz) under Cd-109. With the foils the rates were 47 counts/min (0.78 ± 0.12 Hz) without a source, 35,520 counts/min (592.00 ± 8.07 Hz) under Fe-55, and 7,321 counts/min (122.02

± 2.44 Hz) under Cd-109. Therefore, it was found that the foils only allowed for 35.4% of Fe-55 X-rays to penetrate, while it allowed 80.1% of Cd-109 X-rays through. This is likely due to the fact that Cd-109 emits X-rays of significantly higher energy than those produced by Fe-55. As the detector upon examination was not producing a response near these rates, it was an indication that we had not yet achieved the appropriate gas gain conditions.

System Polarity Test

At a later time, motivated by the use of a dual amplifier which allowed for an inversion of polarity, it was decided to verify which parts of the system do or do not invert the signal, so as to confirm whether or not genuine pulses should appear as positive or negative on the scope (as there had been several cases of negative pulses being observed on the scope in addition to the positive pulses). The polarities of the system were tested after verifying that both the Timing and Energy output channels on the pre-amplifier produced the same signal on the oscilloscope.

In order to test this, a Hewlett Packard 8012B Pulse Generator was used, producing a small negative single pulse, taking the place of the THGEM detector in the system. For a majority of the tests, a 20 dB attenuator was attached to the output of the pulse generator in order to get the pulse to have a sufficiently low amplitude. The dual amplfier was set to a positive polarity, with a gain of 3.

The negative pulse with 20 dB attenuator (Figure 38) was then paired with a positive pulse from the always positive “trigger output (+)” function of the

generator (Figure 39). That negative pulse was then connected to the pre-amplfier, and one of the output channels of the pre-amplifier was connected directly to the scope as C2, and the other was connected to the amplfier, with the resulting signal being made C3 (Figure 40).

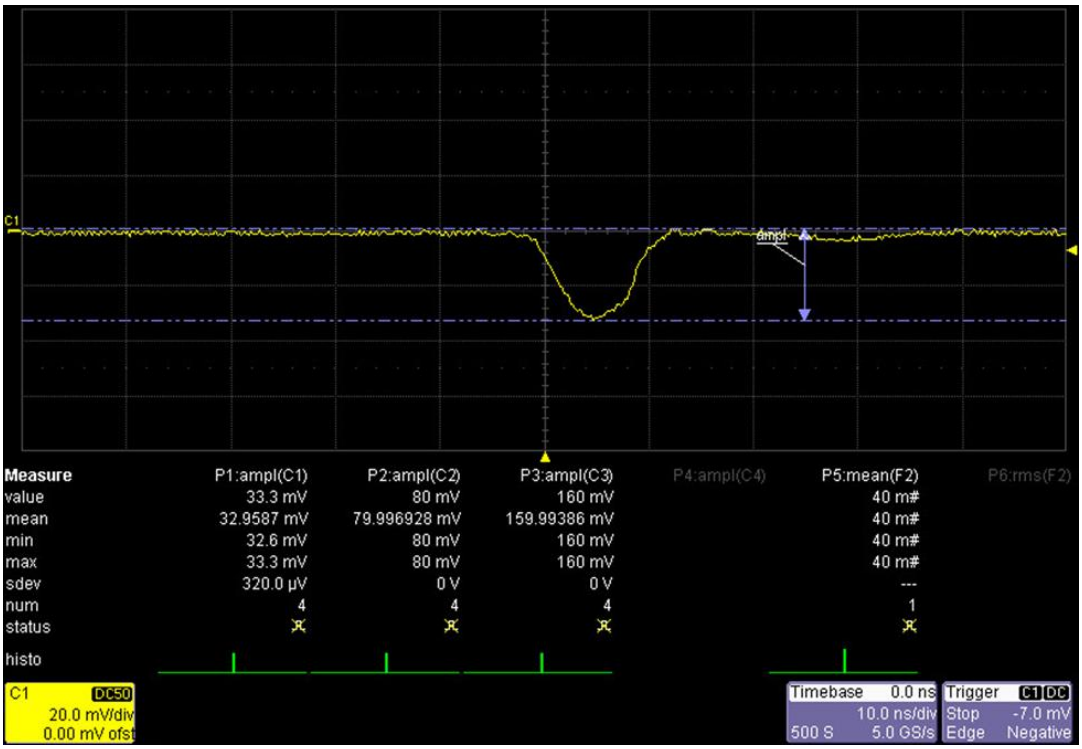

Figure 38: Negative pulse from pulse generator with 20dB attenuator

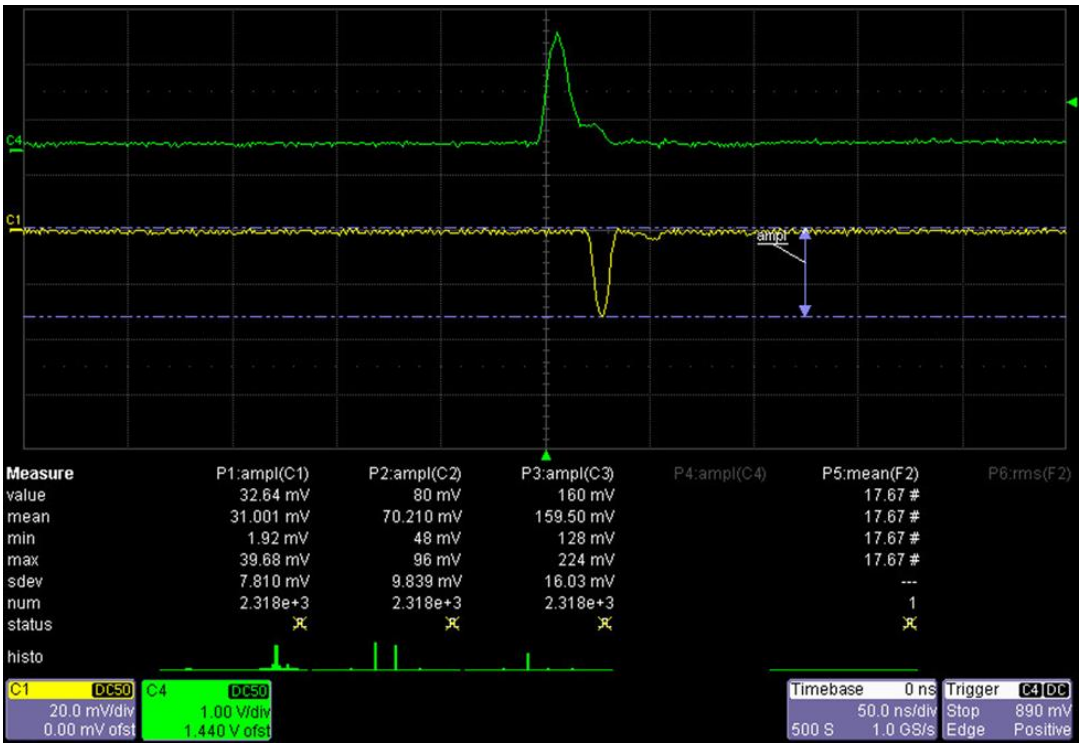

Figure 39: C4 (green) shows trigger output (+), a constant positive 1V across 50Ω pulse 16 ± 10 ns wide. C1 shows the same input negative pulse as Fig.38

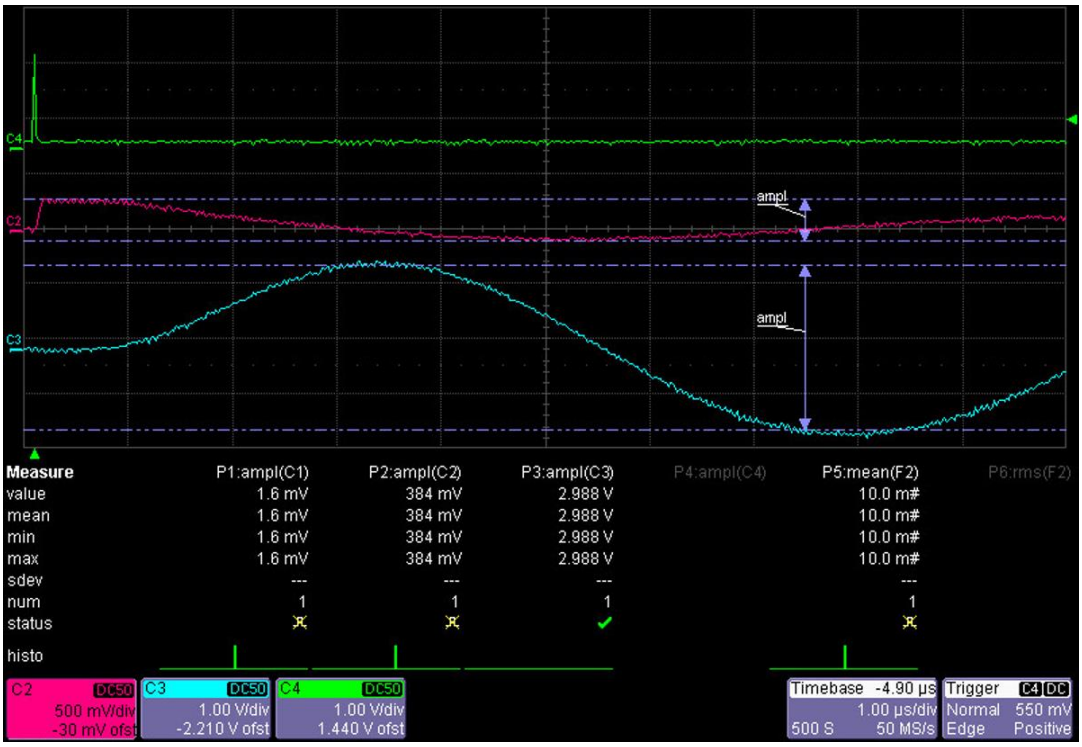

Figure 40: Trigger output (+) (C4, green), pre-amp signal (C2, magenta), amplifier signal (C3, cyan)

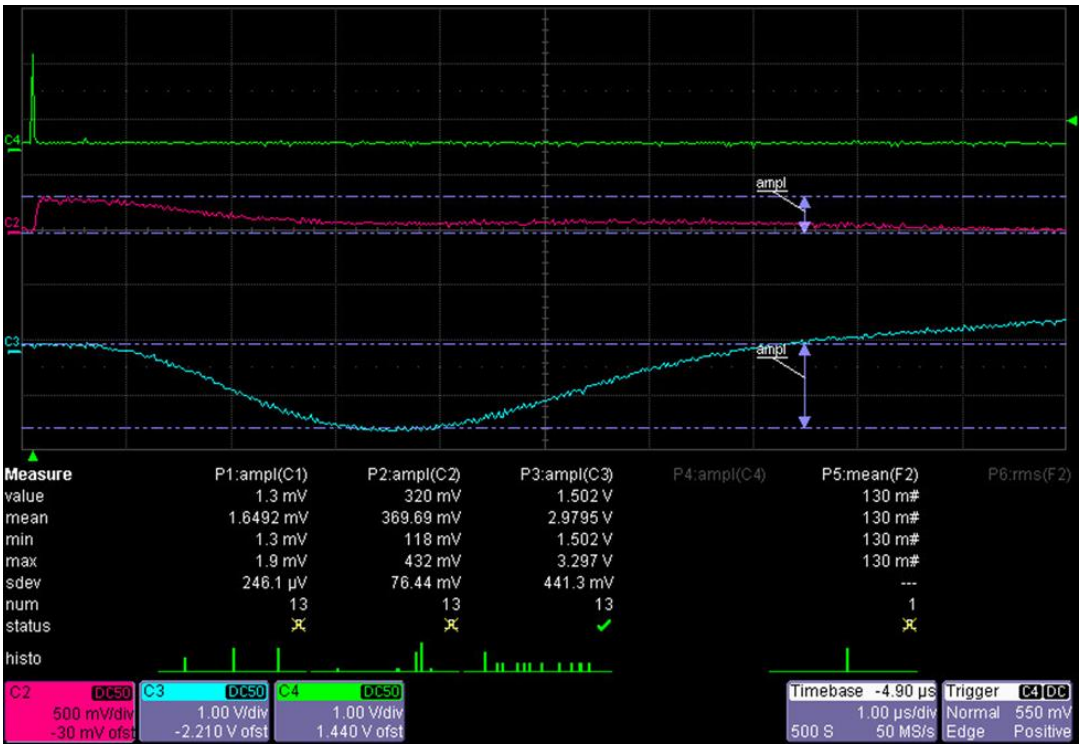

Figure 41: Trigger output (+) (C4), pre-amp (C2), reversed polarity amplifier signal (C3)

Based on Figure 40 we can see that the pre-amplifier (C2 in Figure 40) inverts the negative pulse (C1 in Figure 39). We see from C3 in Figure 40 that the amplifier then does not invert that pre-amp signal, leaving it positive, when set to a positive polarity. But when the polarity of the amplifier is switched to negative, the pulse flips as the signal is inverted (Figure 41). We can therefore say from these results that the output pulses we expect to see should indeed be in the positive region, and that the amplifier should be configured such that it does not further invert the signal, which in this case is when it is set to a positive polarity.

Test of Sector with 0.1 mm Rim

The tests on the detector began using the sector with the smallest rims. As a new pre-amplifier had been installed, the noise levels were much lower, and therefore it was possible to significantly lower the threshold. It was later discovered that the noise level was too low to register any response on the Timing SCA, therefore the amplifier gain had to be doubled to 36 in order to get accurate counts which could then be used to ensure that the trigger threshold levels of both the oscilloscope and the Timing SCA are the same. For the purposes of this stage of the study, counts using the scaler were not necessary, as the observations were primarily taken off of the scope and HV monitor.

Figure 42: GECO2020 HV Monitoring software (top) and scope traces (bottom) under Fe-55. The top scope trace is through the pre-amplifier followed by the amplifier, and the bottom trace is through only the pre-amplifier. In the GECO2020 software, from top to bottom, the electrodes shown are: THGEM Bottom, (Unused Channel), THGEM Top, Drift.

Figure 42 above shows the HV settings during the occurrence of the indicated pulse on the scope. From top to bottom, the electrodes shown are: THGEM Bottom, (Unused Channel), THGEM Top, Drift foil. Therefore, these particular settings indicate an induction field of 2kV/cm, a bias voltage across the THGEM of approximately 1800V and a field of approximately 25.7kV/cm in the

holes, and a drift field of approximately 3.83kV/cm. While the shape of these pulses were along the lines of what we would have expected, their rates were fairly low. Additionally, there were moments of poor behavior due to sparking, and electrodes (particularly the Bottom electrode) would register on the GECO2020 HV monitor as having gone overvoltage, which would create wild behavior on the scope temporarily.

Several tests were conducted after this, during which coupling as well as other parameters were changed, while histogram data of the amp and pre-amp signals was monitored. Additionally, hardware settings were adjusted, and the amp gain was again changed from 18 to 36. Occasionally during testing there were strange traces on the scope, odd current monitor values, and spark-like sounds, but it was found that these issues sometimes resolved themselves overnight.

Sparks could manifest themselves in a variety of ways. Manners include a sharp rapidly rising and falling trace on the scope, a sudden drop in the baseline of the pre-amp signal that rises back up over time, chaotic oscillations on the scope trace which is often paired with similarly chaotic behavior in the HV monitor (values, typically the potential of the Bottom electrode, would fluctuate, either going over or under voltage. Current would also be affected. Other electrodes sometimes fluctuated, but less often than the Bottom electrode), and audible sparking sounds coming from inside or outside of the chamber. Examples of these phenomena are shown in Figure 44 and Figure 44 below.

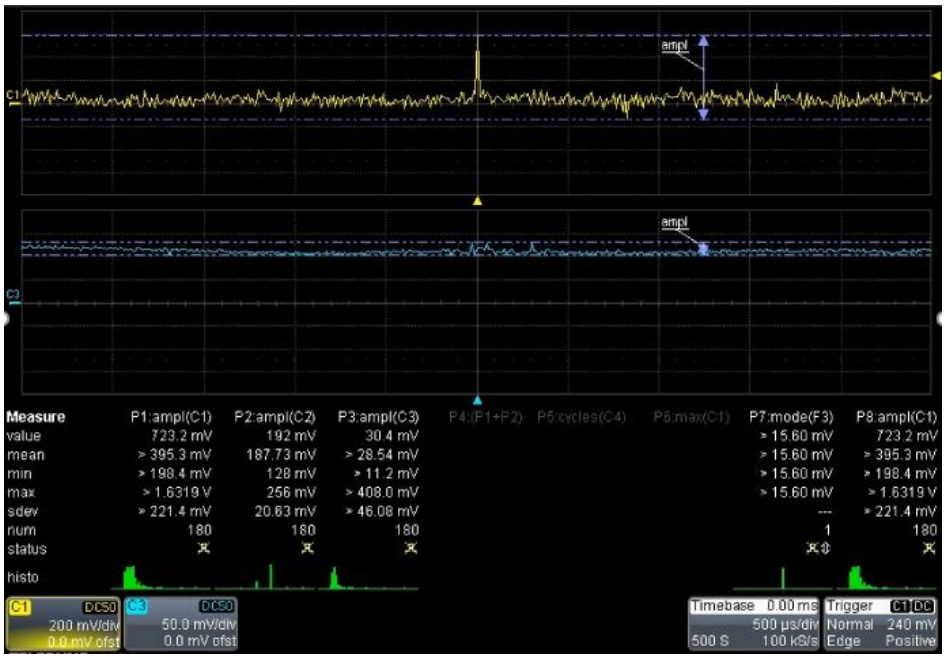

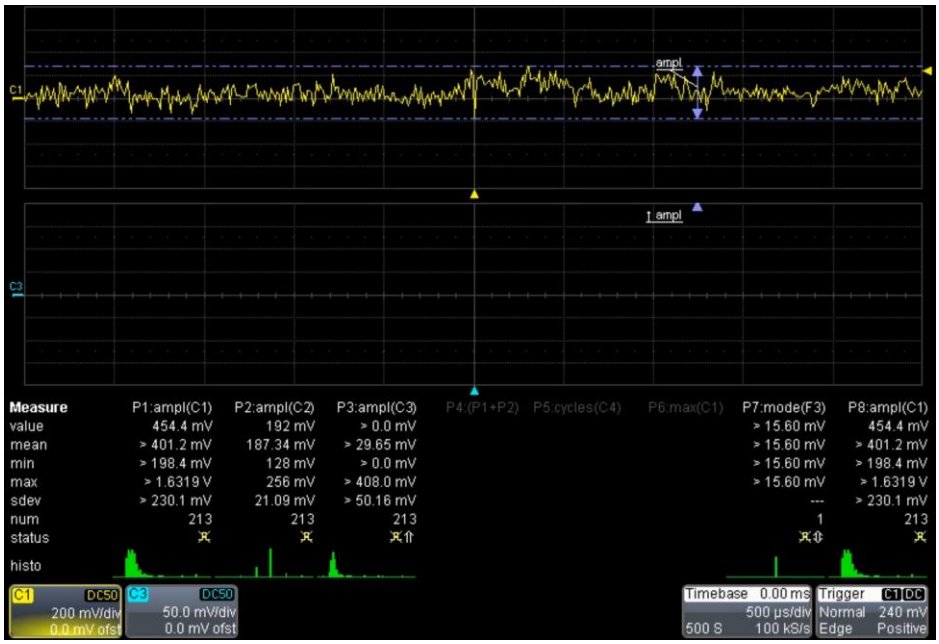

Figure 43: Scope images showing occurrences of some of the various forms of suspected discharges

Custom	ISet	VSet	VMon	Pw	hStati	RUp	RDwn	Trip	onRang	IMonL	IMonH	MaxV	PDwn	olarit
00.000	5.00 uA	200.0 V	**455.0 V**	On	**Ovv**	2 Vps	50 Vps	0.0 sec	Hi	**0.00 uA**	**0.00 uA**	1000 V	Kill	**NEG**
00.001	0.00 uA	0.0 V	**10.8 V**	Off	**Dis...**	5 Vps	50 Vps	0.0 sec	Hi	**0.00 uA**	**3.80 uA**	550 V	Kill	**NEG**
00.002	15.00 uA	2350.0 V	**2349.6 V**	On	**On**	2 Vps	50 Vps	0.0 sec	Hi	**0.00 uA**	**3.40 uA**	3000 V	Kill	**NEG**
00.003	10.00 uA	3100.0 V	**3099.6 V**	On	**On**	2 Vps	50 Vps	0.0 sec	Hi	**0.00 uA**	**2.30 uA**	4000 V	Kill	**NEG**

Custom	ISet	VSet	VMon	Pw	hStati	RUp	RDwn	Trip	onRang	IMonL	IMonH	MaxV	PDwn	olarit
00.000	5.00 uA	200.0 V	**454.8 V**	On	**Ovv**	2 Vps	50 Vps	0.0 sec	Hi	**0.00 uA**	**0.00 uA**	1000 V	Kill	**NEG**
00.001	0.00 uA	0.0 V	**10.8 V**	Off	**Dis...**	5 Vps	50 Vps	0.0 sec	Hi	**0.00 uA**	**3.75 uA**	550 V	Kill	**NEG**
00.002	15.00 uA	2350.0 V	**2350.0 V**	On	**On**	2 Vps	50 Vps	0.0 sec	Hi	**0.00 uA**	**2.40 uA**	3000 V	Kill	**NEG**
00.003	10.00 uA	3100.0 V	**3099.6 V**	On	**On**	2 Vps	50 Vps	0.0 sec	Hi	**0.00 uA**	**2.20 uA**	4000 V	Kill	**NEG**

Figure 44: HV monitor images during occurrences of suspected discharges

In order to check for real pulses in the negative region, the scope was set to trigger on a negative threshold on the negative edge, which revealed large saturating pulses (Figure 45).

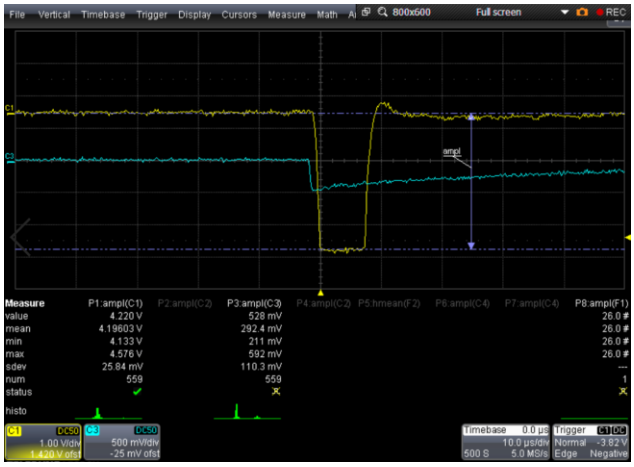

Figure 45: Large negative pulses, source on. HV settings were 3kV/cm Induction field, 1800V Bias across the THGEM, and 3.5kV/cm Drift field. Test conducted for the small rim board sector.

These pulses occurred at a high rate with no observable difference whether source was on or off. The HV conditions in the above image were 3kV/cm Induction field, 1800V Bias across the THGEM, and 3.5kV/cm Drift field.

To investigate this, the trigger counting feature of the oscilloscope was used in determining the rate of these negative pulses. The trigger threshold was set

to -170mV, and the detector was ramped up to have a 3kV/cm induction field, an 1800V bias across the THGEM, and a 3.5kV/cm drift field. With the source off the rate was 45.67 ± 2.65 Hz, and with the Fe-55 source added the rate was 41.83 ± 2.49 Hz, a non-significant difference. (With the absence of the original trigger count values, these errors as well as those in the remainder of this section are to the best approximation.) In order to isolate specifically those very large negative pulses, the trigger level was lowered down to -2.5V, which resulted in a rate of 6.05 ± 0.70 Hz with source off, and 5.48 ± 0.66 Hz with source on, again an insignificant difference. This test was tried again, this time using Cd-109 as the radiation source, which at a threshold of -170mV gave a source-on rate of 50.95 ± 2.87 Hz, and at a threshold of -2.5V, 0.33 ± 0.14 Hz.

Next the bias across the THGEM board was set to 1900V. At -170mV trigger threshold using Fe-55, there was a rate response of 47.48 ± 2.73 Hz with the source off, and 48.13 ± 2.75 Hz with the source on. Using the Cd-109, there was a source-off rate of 48.07 ± 2.75 Hz, and with source on, 48.87 ± 2.78 Hz, none of these differences being significantly different.

At a -2.5V threshold using Fe-55, there was a 0.57 ± 0.18 Hz rate response with source off, and 0.42 ± 0.15 Hz rate response with source on. Using Cd-109, there was a 0.23 ± 0.11 Hz rate response with source off, and 0.12 ± 0.08 Hz response with source on. Again, no significant difference.

Next the bias was increased to 2000V across the THGEM. At a threshold of -170mV under Fe-55 with source off there was a rate response of 45.93 ± 2.66 Hz, and with source on, 54.25 ± 3.00 Hz. The test was stopped here due to concerns over discharge. Curiously, when the -2.5V threshold case was attempted, there were almost no instances of the large negative pulses, and ones of this type were rarely if ever observed again.

Using the timing SCA and Scaler is the preferred method for rate calculations. However, through an observation of amplifier, pre-amplifier, and timing SCA signals on the scope, it was confirmed that the timing SCA is only reacting to positive pulses, and therefore the Scaler cannot count negative pulses.

In later stages of experimentation, the predominant form of negative pulses were ones over a larger timescale. These often presented with an overshoot into the positive region (see Figure 46). It was determined that these overshoots into the positive region were the reason behind some of the occasional counts on the Scaler when looking for negative pulses. The SCA is triggered by the overshoots, which are paired with a negative pulse, thus registering a count. When a negative pulse existed without a positive overshoot, the Scaler would not register a count.

To get around this inability to count negative pulses properly, we switched to a different amplifier (Figure 47).

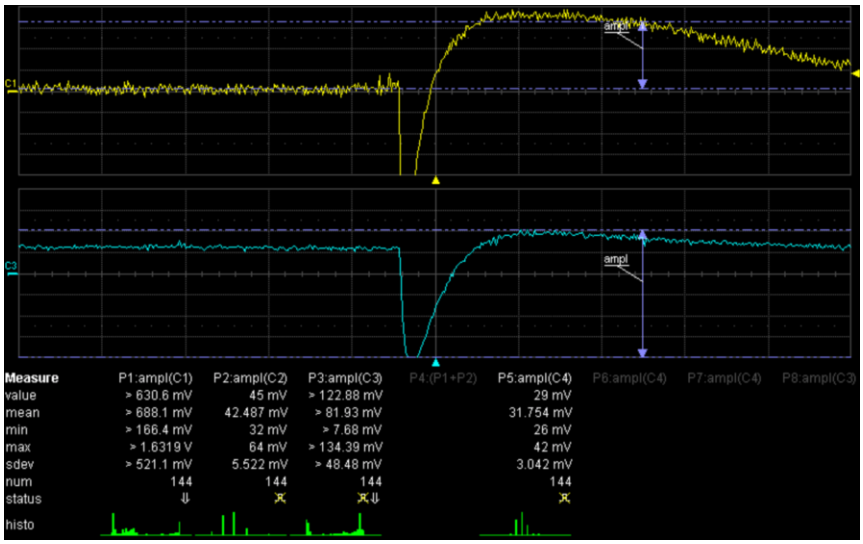

Figure 46: Pulses at a 500 µs timescale. Amp signal in yellow, pre-amp signal in blue.

Figure 47: Former amplifier (Tennelec TC 247) on the left, new one (Mech-Tronics Nuclear 519) on the right

This alternate Dual Amplifier model would allow us to reverse the polarity of the amplifier gain, turning the negative pulses into positive pulses, which could then be fed into the timing SCA, and thus be properly counted by the Scaler. (The

original Tennelec TC 247 Dual Amplifier would be used again in the final small and large rim tests).

Before changing tactics, one final test was conducted using the aforementioned method. The trigger threshold on the scope was set to 168mV, triggering on the positive edge. The rate was counted with and without source, then the threshold was switched to -168mV triggering on the negative edge, and the rate with and without source was measured again. This was done with a 3kV/cm induction field, and a Drift field of 3.5 kV/cm, and an Fe-55 source. The only difference in each trial was the bias voltage across the thick GEM.

For the 1800V bias case, on the positive threshold side, there was a rate of 1.40 ± 0.30 Hz with source off, and 0.87 ± 0.23 Hz with source on. In the negative threshold region, the source-off case had a rate of 0.90 ± 0.20 Hz, and with source on, a rate of 0.77 ± 0.22 Hz.

For the 1900V bias case, in the positive threshold region with source off, there was a count rate of 1.50 ± 0.30 Hz, and with source on, a rate of 1.23 ± 0.28 Hz. On the negative side, 1.40 ± 0.30 Hz for source-off, and 1.13 ± 0.27 Hz for source-on.

The 2000V case could not be completed due to discharging. None of these results indicated any significant differences in the rate under the presence of the Fe-55 or Cd-109 sources. This indicates that at the time of testing, the HV settings used were not sufficient to produce gas gain. Additionally, it is likely that the

pulses that were seen were likely due to noise or some sort of false signal occurring within the detector. One observation found was that when the longer timespan pulses occurred, several counts would be registered on the scaler at once. Initially these were thought to be discharges, so whenever noticed the test was redone to avoid discharges skewing the results. They were however a property which would later be investigated more thoroughly.

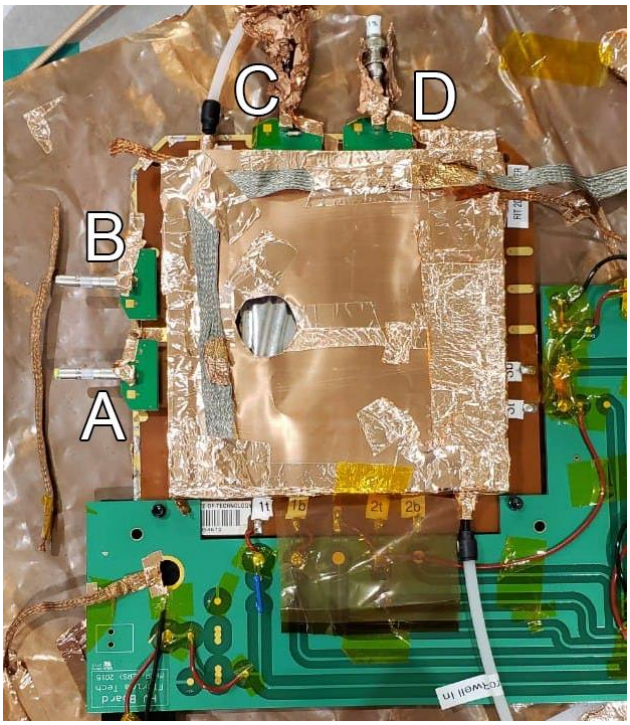

Figure 48: Detector with labels indicating the different Panasonic connectors

The readout board that was chosen to replace the original square pad version has two sets of 128 straight strips in both the X and Y directions, with each set given its own Panasonic connector, giving a total of four Panasonics. These Panasonics are the connector through which the signal charge induced by the

electrons collected by the straight strips is fed into the pre-amplifier input (after first ganging together all 128 of the strips represented on the Panasonic connector together using a Panasonic-to-Lemo adapter, resulting in a single signal, which then also passes through a Lemo-to-BNC adapter), which is then output to both the oscilloscope and the dual amplifier which also then connects to the oscilloscope. Using Panasonic-to-Lemo adapters, information is read off of different sections of the readout board. They are labeled in Figure 48 above as A, B, C, and D, and will be referred to in that manner hereafter. For the gain and long-duration tests, connection C was used for the small rim sector, connection B was used for the medium rim sector, and connection D was used for the large rim sector, unless otherwise indicated.

It is also possible, through a special BNC connection, to read off the information directly from the bottom electrode of the THGEM.

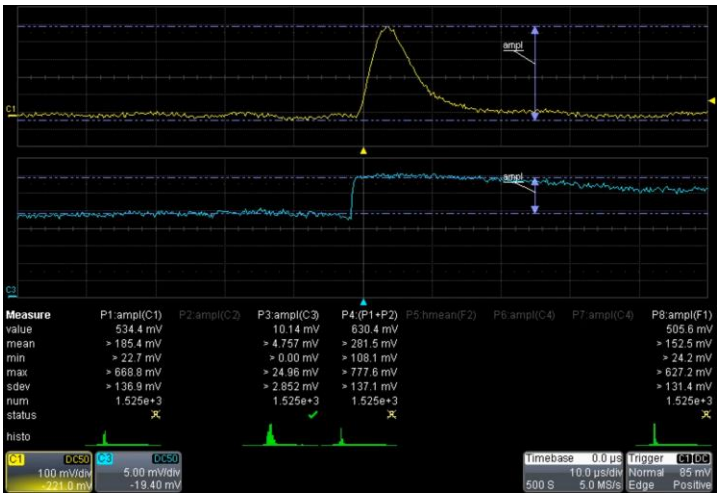

Figure 49: Pulse read off of THGEM Bottom under Ar/CO_2

Figure 49 above shows a pulse found when reading off of the bottom electrode of the THGEM with drift and induction fields of 3 kV/cm, and a bias across the small rim THGEM sector of 1800V. Panasonic connector locations A and B were used to check for rate response and pulse shape. Some strange shapes were occasionally found, and the rate response was not significantly different under an X-ray source.

A question therefore arose about the ability for X-rays to enter the window of the current detector, as the window which was previously tested was no longer in use. Using a similar setup as that in Figure 37, the Geiger counter test determined that with source off there was a count rate of 0.65 ± 0.20 Hz. With the Fe-55 source there was a count rate of 726.17 ± 24.18 Hz. With the Cd-109 source there was a count rate of 100.63 ± 4.76 Hz. With the Am-241 alpha source, there was a count rate of 107.93 ± 5.02 Hz, and 0.73 ± 0.21 Hz with the source off. The errors for these rate values were approximated. While this cover was therefore determined to be allowing proper penetration, the cover was nevertheless replaced with the original one.

Panasonic connection regions A and B (Lemo A and Lemo B, respectively) were tested again, now with utilizing the middle sector of the THGEM board. (The rate errors following are approximated.) 3kV/cm Drift and Induction fields, and an 1800V THGEM bias were used for each trial. For Lemo A, with the source off

there was a rate of 2.43 ± 0.41 Hz. With the Fe-55 source on, there was a rate of 3.10 ± 0.50 Hz.

The hole in the copper shielding was moved to place it more directly over the area of Lemo B, while all other parameters were kept the same. There was a source-off rate of 0.10 ± 0.10 Hz and a source-on (Fe-55) rate of 0.33 ± 0.14 Hz.

A primary concern throughout this process has been a so-called "bias voltage wall" of around 1900V across the THGEM. Based on literature and observation, we suspected that the reason we were not getting rate gains to the degree expected was because we were not achieving a high enough bias voltage across the THGEM. However, as we were able to view the potential and current on each electrode individually, we were able to see cases where the THGEM, particularly the Bottom electrode, went into a state of overvoltage or some other current draw phenomenon. Not wanting to risk damaging the detector due to sparking or some other event, this became a sort of limit on the fields we were able to reach, and thus the gains we were able to achieve.

Based on information in [7], we determined that the best course of action to get around this limit for now would be to use the sector of the THGEM board which contained the next largest rim anulus.

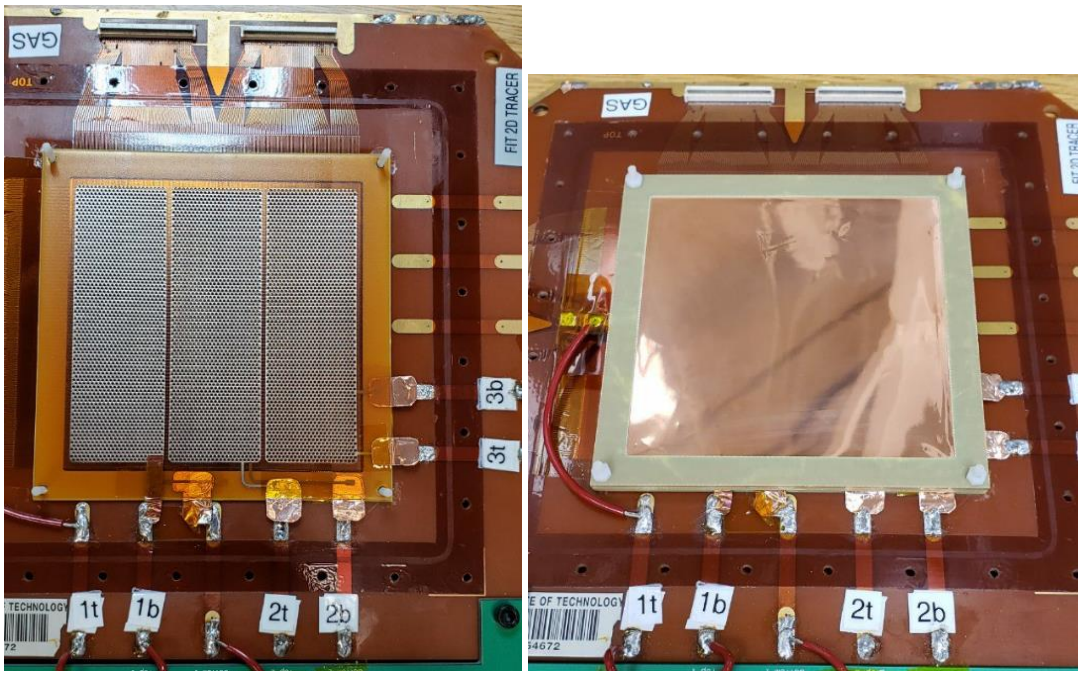

Figure 50: Internal HV connections formed from copper tabs to power each sector

Now the detector was opened back up and each remaining sector of the board was given new copper tape tabs to deliver potential to each side of their THGEM segments (see Figure 50 above). Copper tape was used for a few different reasons. Its thinness allows it to keep the flatness of the board as unperturbed as possible, unlike a wire would. Additionally, its conductive adhesive surface would allow it to be connected to the silver strips extended from the THGEM active area (aside from on the smallest rim sector, where the copper tape connection for the top electrode had to be made directly to the surface of the active area, as the extending strip had come apart due to previous handling, as can be seen in Figure 51) without the need for solder.

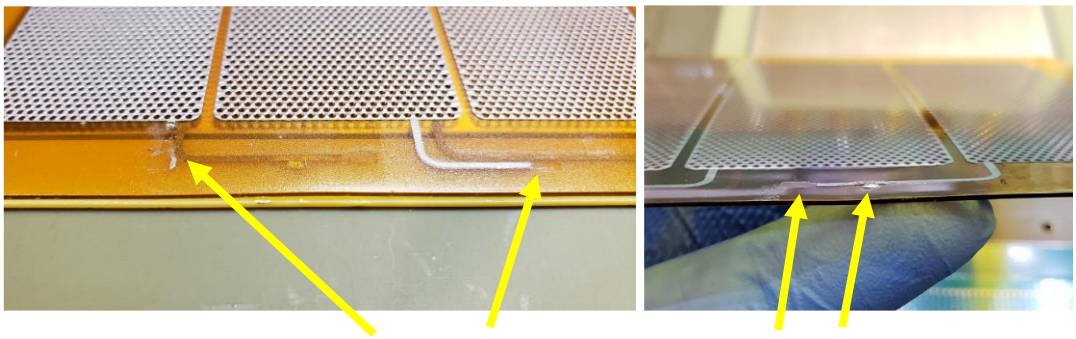

Figure 51: Various damages which can occur through soldering

Soldering directly to the board has proven dangerous, as the heat from the soldering iron can lift the silver layer off of the plastic surface, allowing it to then easily break. It can also cause distortions in the plastic as shown in Figure 51, and excess solder can remain on the surface, causing potential flatness concerns. The use of copper tape alleviates these and other potential issues.

With these internal HV connections established it was now possible to use any sector of the board simply by switching which pads the other electrical connections are soldered to outside of the THGEM chamber.

Test of Sector with 0.15 mm Rim

The next several tests were then conducted using the middle sector, which has rim annuli of 0.15mm. The errors on rate values in this section are approximated. For the initial tests, the source was changed to the alpha source Am-241, with induction and drift fields of 3kV/cm.

Reading off of THGEM Bottom with a bias across the THGEM of 1800V, there was a source-off rate of 16.10 ± 1.30 Hz, and a source-on rate of 14.10 ± 1.20 Hz, an insignificant difference. Reading off of Lemo C (Figure 48) there was a source-off rate of 5.60 ± 0.70 Hz, and a source-on rate of 5.40 ± 0.70 Hz. With a 1900V bias there was a source-off rate of 17.73 ± 1.38 Hz, and a source-on rate of 18.60 ± 1.40 Hz.

It was at a 2000V bias reading off of Lemo C where we saw the first evidence of a genuine rate increase with this detector. With the source off there was a rate response of 25.77 ± 1.78 Hz, and with the alpha source on, 60.40 ± 3.30 Hz, a 134.38% increase. The bias was then increased to 2100V, and with source off there was a rate response of 34.27 ± 2.17 Hz, and with source on, a rate response of 92.20 ± 4.50 Hz. A few instances of discharge as evidenced by the dropping of the pre-amp trace, as well as audible indications, occurred here and similarly with Fe-55. There was no effect shown on the HV monitor, however.

Next Lemo D was tested in a similar fashion as Lemo C. With an 1800V bias, there was a source-off rate of 4.20 ± 0.60 Hz, and a source-on rate of 4.73 ±

0.60 Hz. With a 1900V bias there was a source-off rate of 4.50 ± 0.60 Hz, and a source-on rate of 10.40 ± 1.00 Hz. Once again the 2000V mark indicated a significant change. At this bias voltage, there was a source-off rate of 4.00 ± 0.60 Hz, and a source-on rate of 34.53 ± 2.18 Hz.

As there was no sign of what was considered to be the "bias voltage discharge wall," we continued further. At a 2100V bias, there was a source-off rate of 6.43 ± 0.73 Hz, and a source-on rate of 87.73 ± 4.29 Hz. At a 2200V, the source-off rate was 6.10 ± 0.70 Hz, and the source-on rate was 74.60 ± 3.80 Hz. Occasional discharges were detected at this point. The 2300V bias case could not be completed, as there were frequent instances of discharge in the presence of either Am-241 or Fe-55. The point of significant discharges now appeared to have gone from around 1950-2000V to around a 2300V bias voltage across the THGEM with the switching over to a 50% larger rim sector.

Working with the middle THGEM sector, it was discovered that many of the irregular looking traces were due to the clearer shape at a larger timescale. Switching to a 500-microsecond timescale (as in Figure 46) revealed the true nature of these pulses, which were large negative spikes with large and long-lasting tails which overshot into the positive region.

We then began to conduct more "long-term" studies, where the detector would be powered for several hours, in order to better understand its behavior over longer time periods. In order to account for this issue of overshooting pulses, the

amplifier gain was switched to a negative polarity, so that the rate of negative pulses could be counted, and subtracted from the total number of positive pulses, to in theory give the number of positive pulses without the influence of those overshoots of negative spikes. For each of these tests, Fe-55 was used as the X-ray source, and the drift and induction fields were both set to 3kV/cm, with a bias across the THGEM of 2100V.

Initially in the positive polarity state, the source-off rate (errors on rates here are approximated) was 62.90 ± 3.40 Hz, and the source-on rate was 2340.00 ± 69.30 Hz. In the negative polarity state, the source-off rate was 170.50 ± 7.20 Hz, and the source-on rate was 230.80 ± 9.20 Hz. Applying our overshoot correction method, subtracting the negative polarity rate from the positive polarity rate, we see that the source-off rate was -107.60 ± 10.50 Hz, while the source-on rate was 2109.20 ± 78.50 Hz.

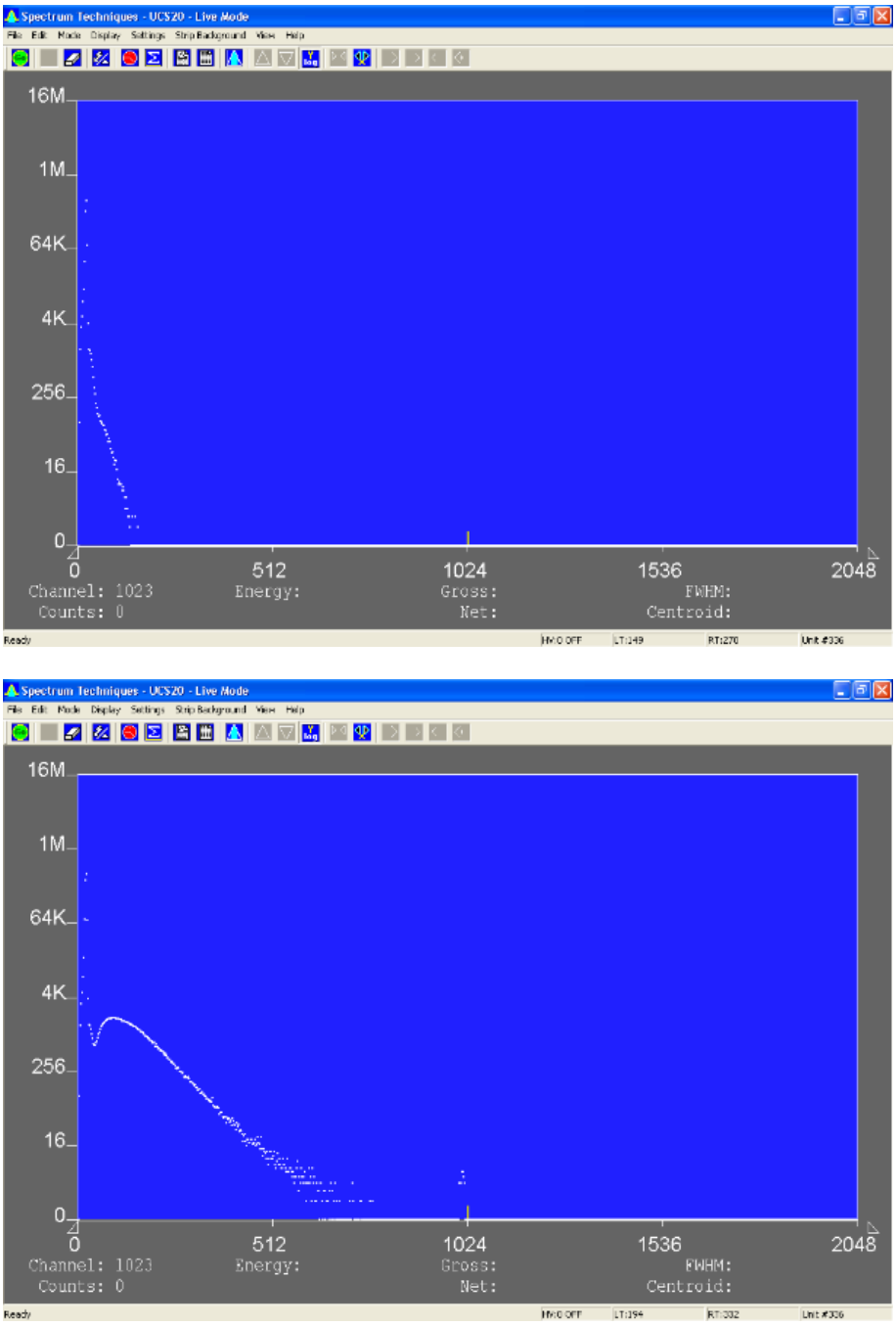

Figure 52: Initial pulse-height measurements taken using an MCA source-off (left) and source-on (right)

The pulse height plotting functionality of a multichannel analyzer (Figure 52) was used to monitor the behavior for both source-off and source-on cases, as well as for each polarity.

At a later time, after lowering the bias voltage to 2000V due to discharge concerns, the rate was checked again, and performing the calculation corrections, there was a source-off rate of -0.65 ± 0.20 Hz, and a source-on rate of 880.40 ± 28.60 Hz (errors on rates are approximated). In the next sections, the results for gas gains tests, a check of the HV response, and subsequent long-term tests will be discussed.

Chapter 5

Results

Measurement of Gas Gain

The next phase of experimentation was to gather gain curves for each of the thick GEMs. These tests included ones that utilized an Amptek Mini-X X-ray gun (Figure 54-55) as the X-ray source.

To set up for irradiation, the detector was placed inside a lead-lined box which housed the X-ray gun (example Figure 53). The X-ray gun was suspended approximately 1 cm over the opening in the shielding above the window of the detector. The X-ray gun is then operated via a laptop set outside of the box. The included interlock system ensures that if the box is accidentally opened while the X-ray is on, the gun is powered down.

Figure 53: Gain testing setup within a lead-lined X-ray Box. Arrow indicates the X-ray gun. The purpose of the fan is to keep the X-ray gun cool and maintain operating temperature.

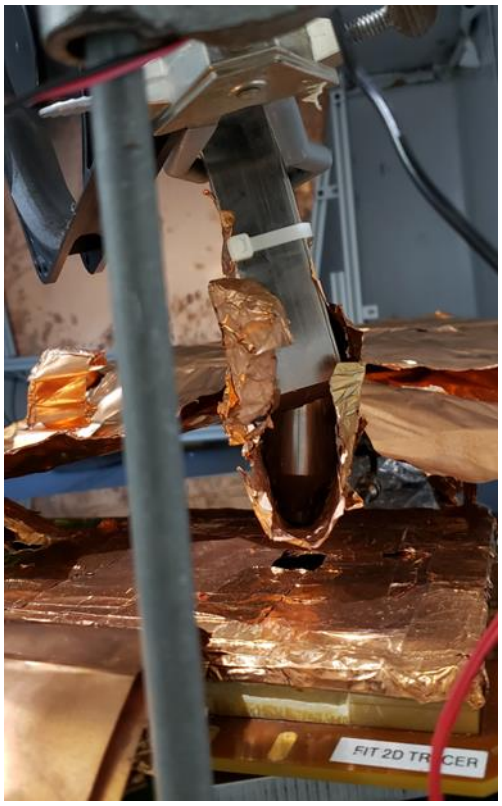

Figure 54: X-ray gun with copper foil filter pointed down at detector.

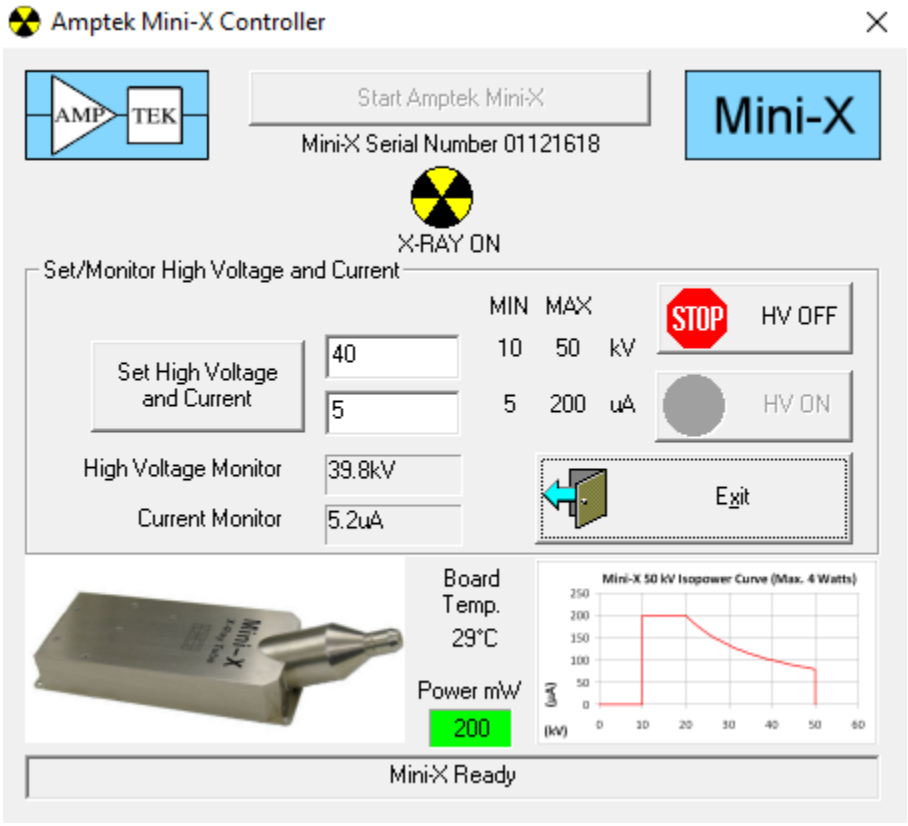

Figure 55: Amptek Mini-X Controller operating screen used to control the X-ray gun used during experimentation

Based on trials involving powering the detector to different field strengths and factoring in the potential difference levels across the THGEM we could achieve before discharges, we sought to optimize the choice of induction and drift field strengths, so that they could remain constant while gathering information on the gain, allowing for the only changing variable to be the bias voltage across the THGEM. HV settings of 1703V for the bias voltage across the THGEM, 2.16 kV/cm induction field, and 1.8 kV/cm drift field were used based on the best observed conditions from the data gathered. (This involved selecting from

datapoints taken during a gain test that had non-constant fields and bias voltages a point which could maximize the HV settings and avoid heavy discharges, thus the HV settings of which being the basis for tests going forward.) From this basis, two tests were conducted in order to observe the detector gain while varying only either the drift field or the induction field, while maintaining a constant bias across the THGEM of 1703V. For the gain calculations, the incident rate of the X-ray gun as calculated from use of the Geiger counter with approximations to account for use of the various foils of 1879.41 ± 289.23 Hz was used (error includes an added systematic error of 10% of the incident rate based on presumed differences in foil penetration under the use of the X-ray gun instead of Fe-55, as the foil penetration test was only done based on the use of Fe-55, yet those values were used in the propagated error calculation). The medium rim THGEM sector was used for these tests.

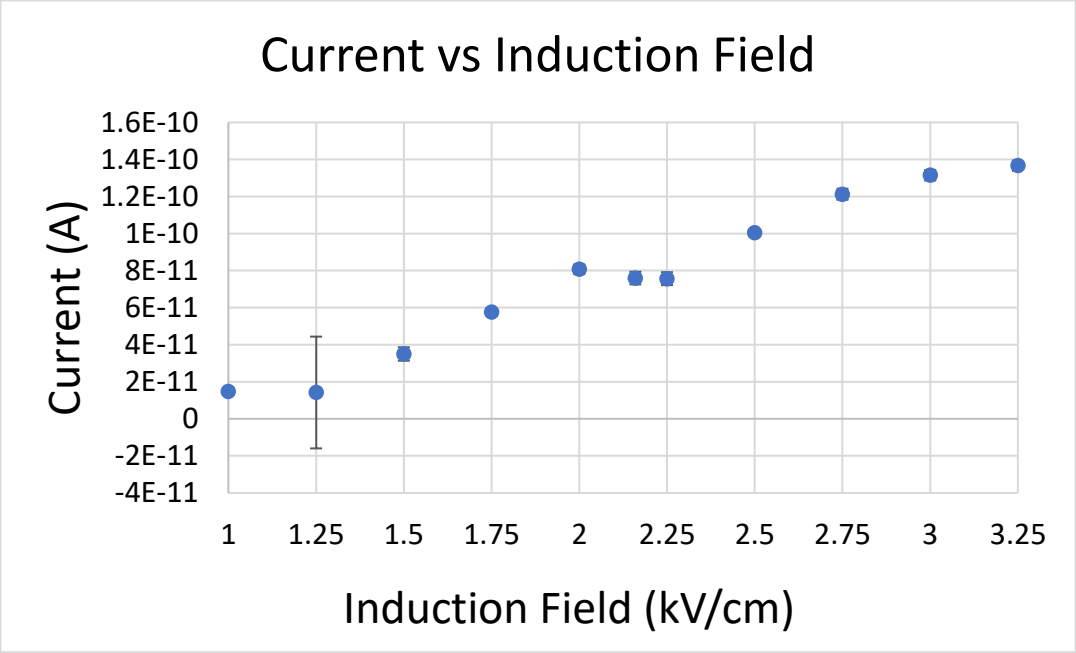

Figure 56: Signal current of the detector vs. induction field, with constant 1.8 kV/cm Drift field and 1703 V THGEM Bias. Error at the 1.25 kV/cm data point is an order of magnitude larger than the next largest error, causing it to have the only clearly visible error bar. This was likely due to a temporary current fluctuation registered by the picoammeter. Error bars are present for all points but, in some cases, small compared to axis units.

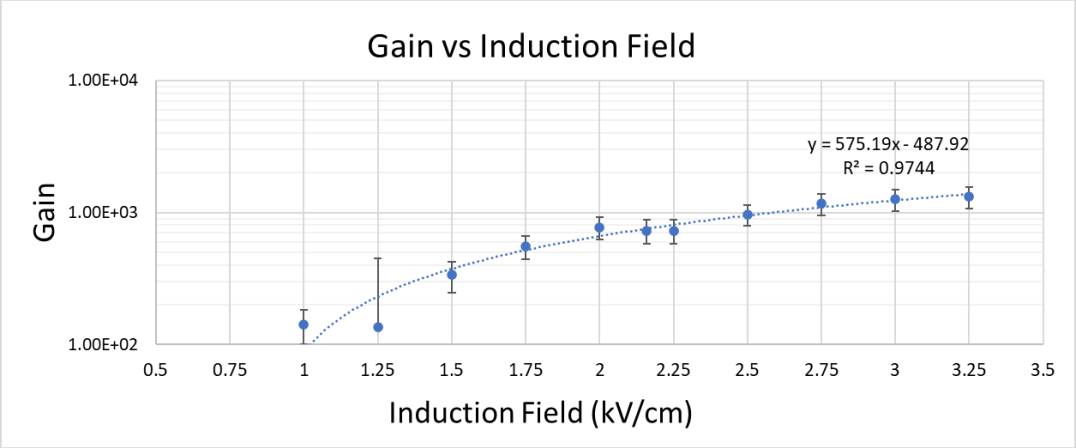

Figure 57: Gain vs. induction field, with constant 1.8 kV/cm Drift field and 1703 V THGEM Bias. Missing lower bars are due to not being able to cross 0 on a log plot.

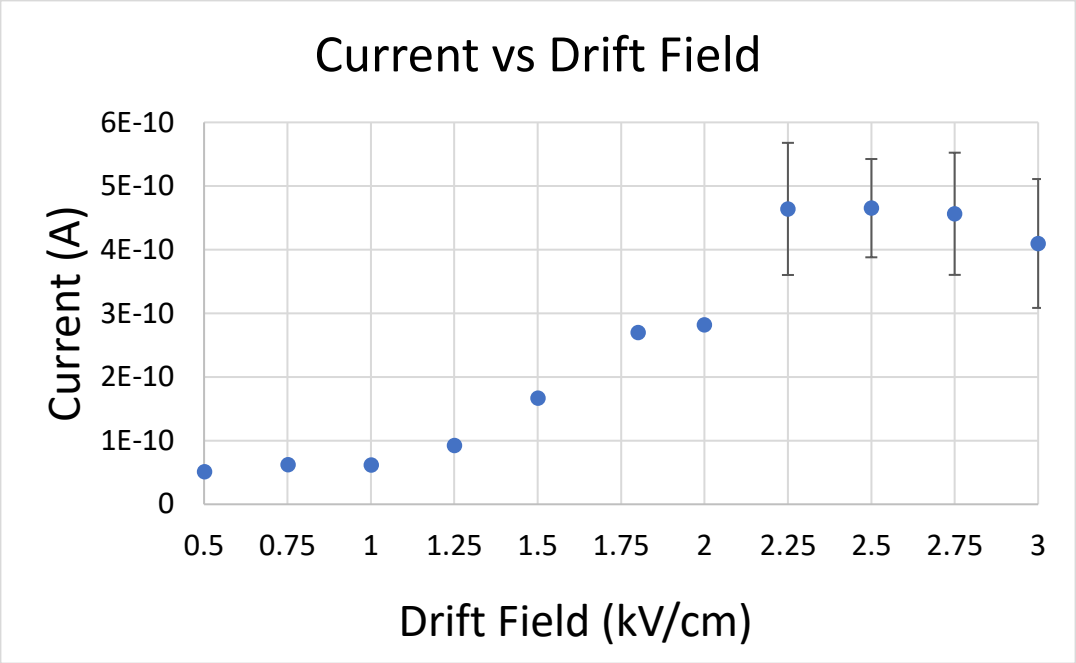

Figure 58: Signal current of the detector vs. drift field, with constant 2.16 kV/cm induction field and 1703 V THGEM Bias. Error bars are significantly larger for the final points due to heavy current fluctuations caused by discharges. Error bars are present for all points but in some cases small compared to axis.

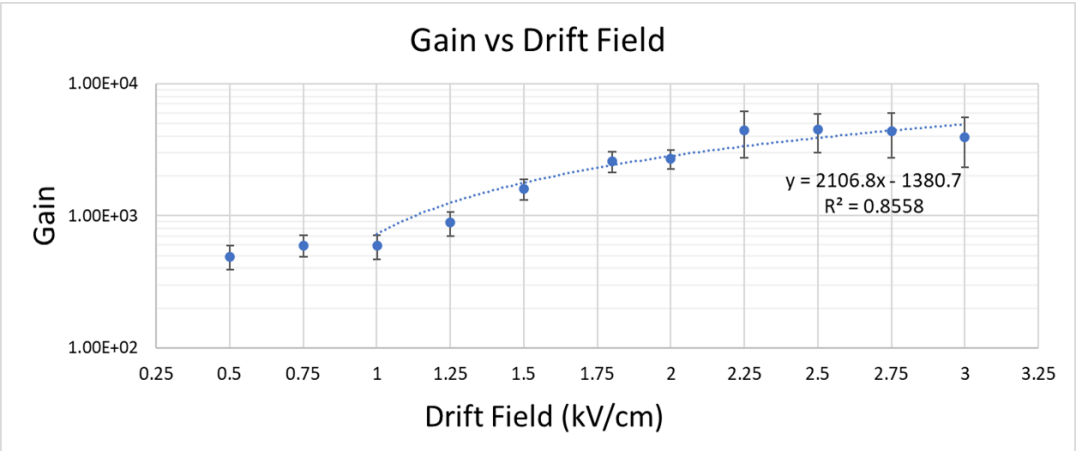

Figure 59: Gain vs. drift field, with constant 2.16kV/cm induction field and 1703V THGEM Bias. Error bars increase in size toward the end of the plot due to increased current fluctuation caused by discharges.

We see from these tests (including Figure 56-59) that choice of induction and drift field strengths does indeed play a role in the gain the detector achieves.

Maintaining the 2.16 kV/cm and 1.8 kV/cm induction and drift fields, respectively, the gas gain curves of the different sectors of the THGEM were found. For collecting the gain curve for this first test of the middle sector, the detector was kept off for greater than 24 hours. The procedure of this test was to conduct X-ray-off and X-ray-on current and rate measurements, with the bottom, top, and drift electrodes set to HV levels such that the induction and drift fields were constant, while the bias across the THGEM increased. The X-ray gun when in use was operated at 40 kV with the current set to 5 μA (Figure 60).

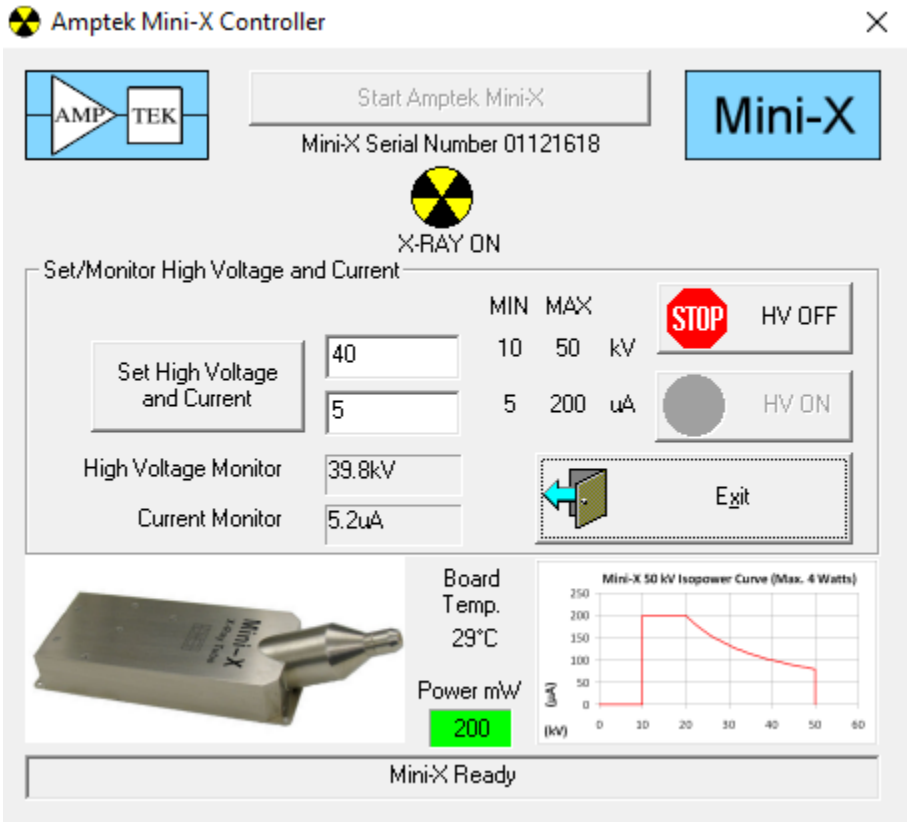

Figure 60: Amptek Mini-X Controller operating screen used to control the X-ray gun used during experimentation

Table 1: Results of Gain test

THGEM BIAS (V)	Xray Off Counts	Off Duration (s)	Xray On Counts	On Duration (s)	Rate (Hz)	Rate Error (Hz)	Avg Current Off (A)	Avg Current On (A)	Current (A)	Gain
1399.2	0	20	2	20	0.10	0.07	5.73E-12	-5.90E-10	5.95E-10	5.72E+03
1449.4	5	20	6	20	0.05	0.25	2.36E-11	-6.85E-10	7.09E-10	6.80E+03
1499.2	0	20	14	20	0.70	0.20	3.10E-11	-7.14E-10	7.44E-10	7.15E+03
1549.2	1	20	61	20	3.00	0.52	3.54E-11	-7.87E-10	8.23E-10	7.90E+03
1599	1	20	443	20	22.10	1.66	2.85E-11	-8.90E-10	9.18E-10	8.82E+03
1609	3	20	552	20	27.45	1.96	2.66E-11	-9.01E-10	9.28E-10	8.91E+03
1619	5	20	659	20	32.70	2.23	3.33E-11	-9.15E-10	9.49E-10	9.11E+03
1629	1	20	773	20	38.60	2.41	2.97E-11	-9.31E-10	9.61E-10	9.23E+03
1639.2	1	20	883	20	44.10	2.64	3.16E-11	-9.62E-10	9.94E-10	9.54E+03
1649	0	20	971	20	48.55	2.77	3.60E-11	-9.98E-10	1.03E-09	9.93E+03
1659.4	0	20	1226	20	61.30	3.28	3.82E-11	-1.01E-09	1.05E-09	1.01E+04
1669.2	6	20	1557	20	77.55	4.05	4.09E-11	-1.03E-09	1.07E-09	1.03E+04
1679.2	1	20	1184	20	59.15	3.25	3.33E-11	-1.04E-09	1.07E-09	1.03E+04
1689.4	5	20	2094	20	104.45	5.02	3.57E-11	-1.06E-09	1.10E-09	1.05E+04
1699.2	2	20	2280	20	113.90	5.31	4.34E-11	-1.10E-09	1.14E-09	1.10E+04
1709.4	2	20	2683	20	134.05	6.02	4.40E-11	-1.13E-09	1.17E-09	1.13E+04
1719.4	6	20	3191	20	159.25	6.94	3.51E-11	-1.16E-09	1.20E-09	1.15E+04
1729.2	7	20	3544	20	176.85	7.55	4.54E-11	-1.19E-09	1.23E-09	1.18E+04
1739.4	7	20	3698	20	184.55	7.80	4.40E-11	-1.27E-09	1.31E-09	1.26E+04
1749.4	9	20	4660	20	232.55	9.40	3.45E-11	-1.28E-09	1.31E-09	1.26E+04

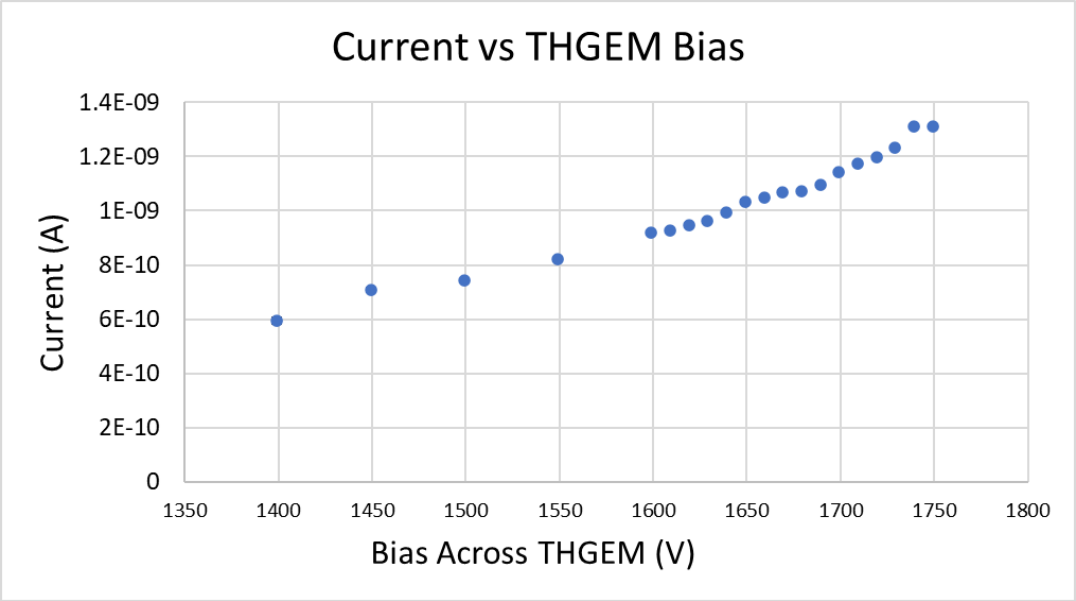

Figure 61: Absolute value of current difference between X-ray on and off vs bias voltage across the THGEM. Error bars are present but small compared to the size of the data point.

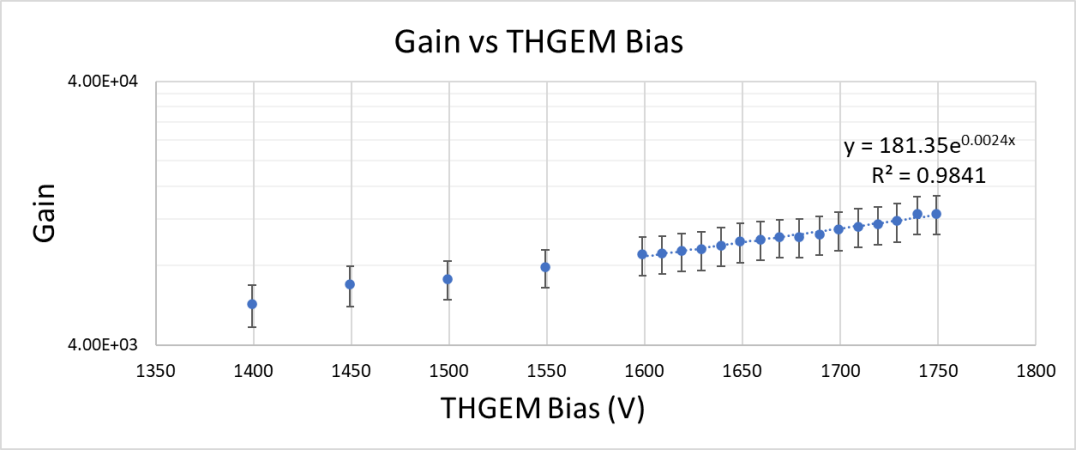

Figure 62: Gain vs Bias across THGEM. Rate of 1879.41 Hz from Geiger Counter used

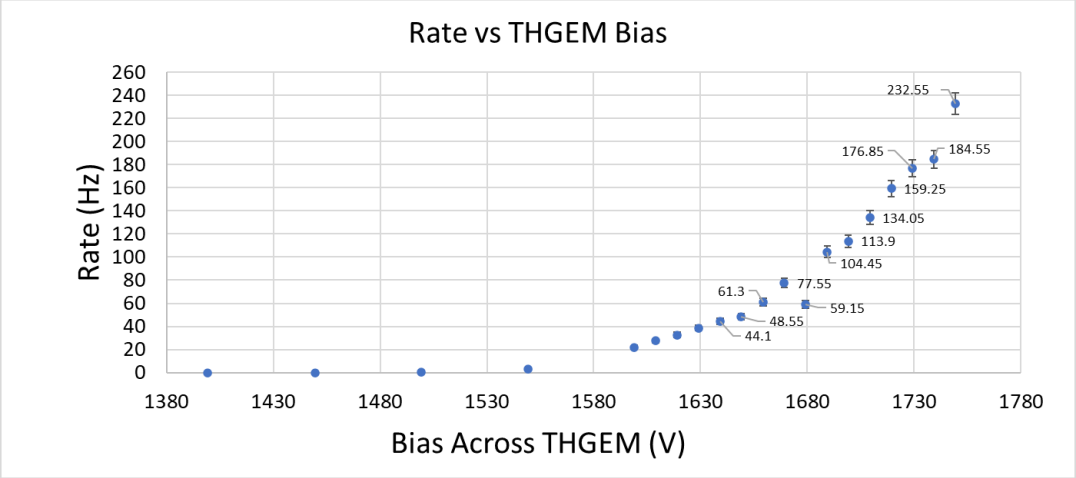

Figure 63: Difference in Rate between X-ray on and off vs Bias across THGEM. Error bars are present but small compared to axis units.

As can be seen in the plots (Figure 61-63) above, the results indicate that the gain is between upper 10^3 and 10^4 for the tested voltage region, which had a bias voltage across the THGEM from 1400-1750V. 1750V was the maximum during this test, to avoid any region with heavy discharges, which at this time was seen to be typical beyond 1800V, and sometimes before, especially when the X-ray gun was in use. As can be seen in Figure 63, the measured rate increases with bias

voltage. This is due to the increase in electric field in the holes causing increased levels of ionization within the detector. Typically, the measured rate will eventually plateau, and that rate becomes known as the incident rate, which is the rate used for gain calculations. For our case, as the rate of the plateau was often located in regions of heavy discharge, the rates given by the Geiger counter under similar conditions was used as the incident rate for gain calculations. This test was later repeated, but with a wider range of THGEM bias voltages tested.

Table 2: Gain calculations and related values

THGEM BIAS (V)	X-ray Off Counts	Off Duration (s)	X-ray On Counts	On Duration (s)	Rate (Hz)	Rate Error (Hz)	Avg Current Off (A)	Avg Current On (A)	Current (A)	Gain
200	226	20	247	20	1.05	1.09	2.97E-11	-4.01E-11	6.98E-11	6.70E+02
399.6	58	20	108	20	2.5	1.11	3.04E-11	-1.00E-10	1.30E-10	1.25E+03
599.6	58	20	274	20	10.8	1.17	3.13E-11	-1.24E-10	1.56E-10	1.49E+03
799.4	56	20	197	20	7.05	1.39	3.92E-11	-2.96E-10	3.35E-10	3.22E+03
999.6	32	20	179	20	7.35	1.22	3.59E-11	-4.65E-10	5.01E-10	4.81E+03
1199.6	28	20	130	20	5.1	1.03	3.34E-11	-5.02E-10	5.35E-10	5.14E+03
1399.4	33	20	189	20	7.8	1.25	3.27E-11	-5.97E-10	6.29E-10	6.04E+03
1449.4	44	20	315	20	13.55	1.67	4.00E-11	-6.28E-10	6.68E-10	6.42E+03
1499.4	50	20	309	20	12.95	1.68	-1.31E-10	-7.21E-10	5.90E-10	5.67E+03
1549.4	66	20	565	20	24.95	1.89	4.45E-11	-7.88E-10	8.32E-10	7.99E+03
1599.2	8	20	1225	20	60.85	3.28	4.73E-11	-8.62E-10	9.10E-10	8.73E+03
1619.2	61	20	1920	20	92.95	5.06	4.33E-11	-8.97E-10	9.41E-10	9.03E+03
1639.4	100	20	2718	20	130.9	6.63	4.09E-11	-9.50E-10	9.91E-10	9.51E+03
1659.2	44	20	2243	20	109.95	5.56	4.08E-11	-9.94E-10	1.03E-09	9.93E+03
1679.4	102	20	375	20	13.65	2.07	3.90E-11	-1.08E-09	1.12E-09	1.07E+04
1699.2	85	20	546	20	23.05	2.42	3.77E-11	-1.15E-09	1.18E-09	1.14E+04
1709.2	86	20	956	20	43.5	3.31	4.75E-11	-1.14E-09	1.19E-09	1.14E+04
1719.2	25	20	999	20	48.7	3.11	4.69E-11	-1.21E-09	1.26E-09	1.21E+04
1729.2	74	20	1053	20	48.95	3.46	4.51E-11	-1.22E-09	1.26E-09	2.01E+03
1739.2	64	20	981	20	45.85	3.27	3.83E-11	-1.23E-09	1.26E-09	2.02E+03

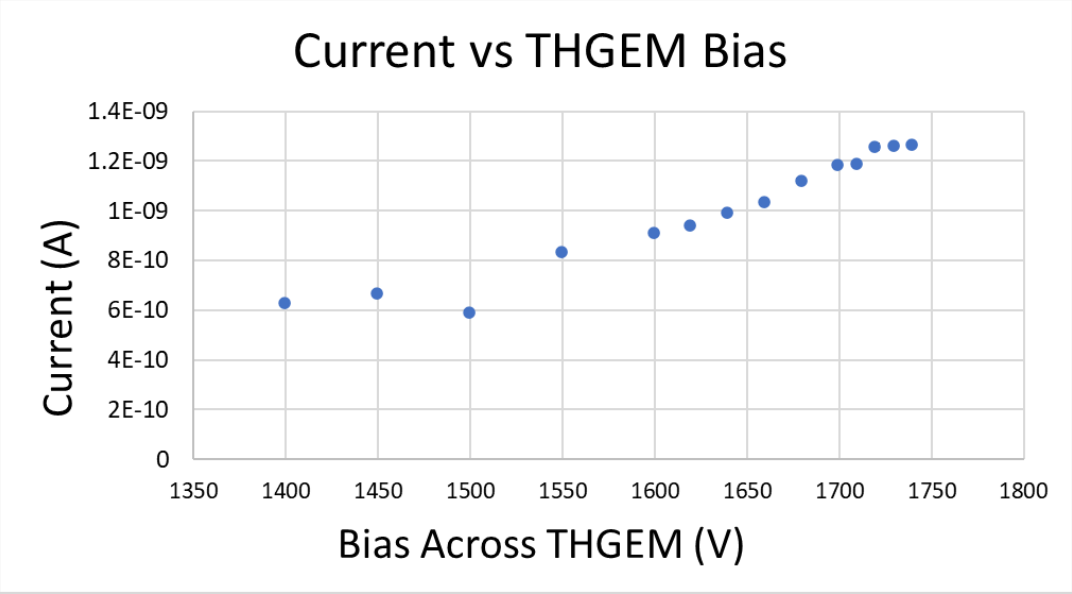

Figure 64: Current values vs bias across the THGEM. Note: error bars are present, but relatively small compared to axis units.

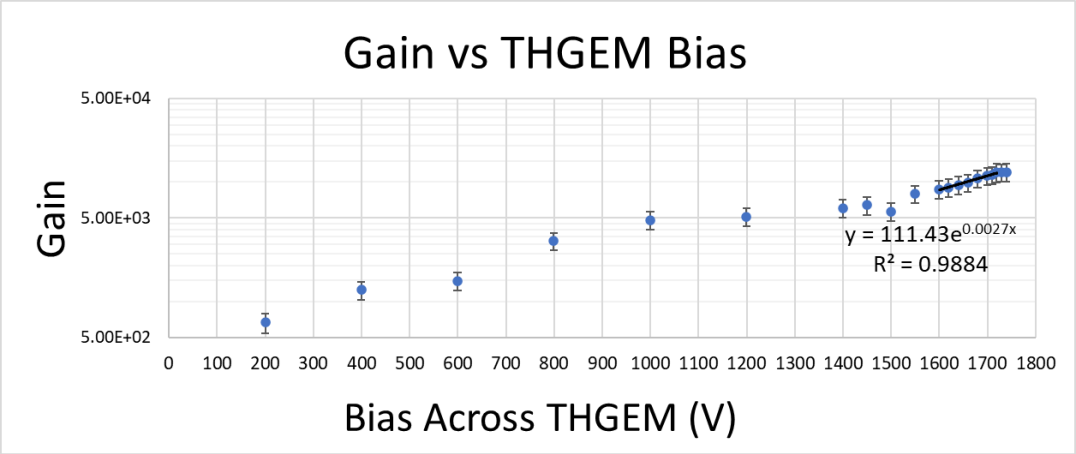

Figure 65: Gain vs bias voltage across the THGEM

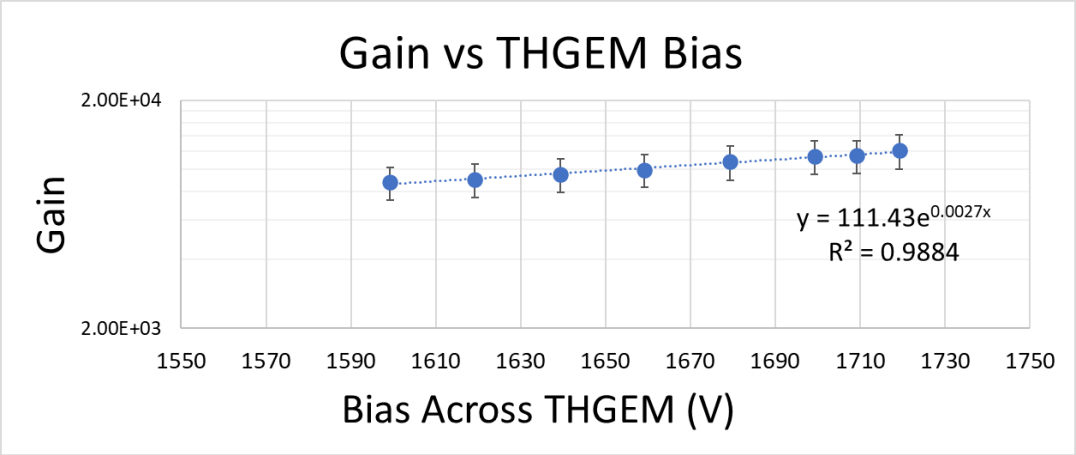

Figure 66: Gain vs bias voltage across the THGEM (zoom on high gain region)

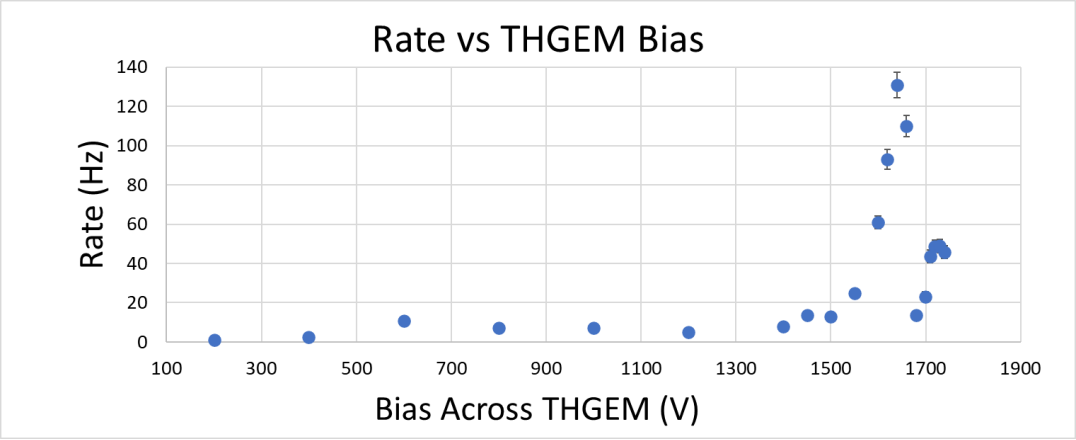

Figure 67: Difference in Rate between X-ray on and off vs bias voltage across THGEM. Error bars are present but small compared to axis units.

There was a curious and sudden drop in the count rate during testing around the 1670 bias voltage mark, as can be seen in the rate plot (Figure 67) above. It is unknown what caused this to occur. However, as the values of the Geiger counter were used for determining the incident rate (1879.41 Hz), the gain curve (Figure 65-66) appears reasonable and stays largely within 10^3 and 10^4 as in the previous test.

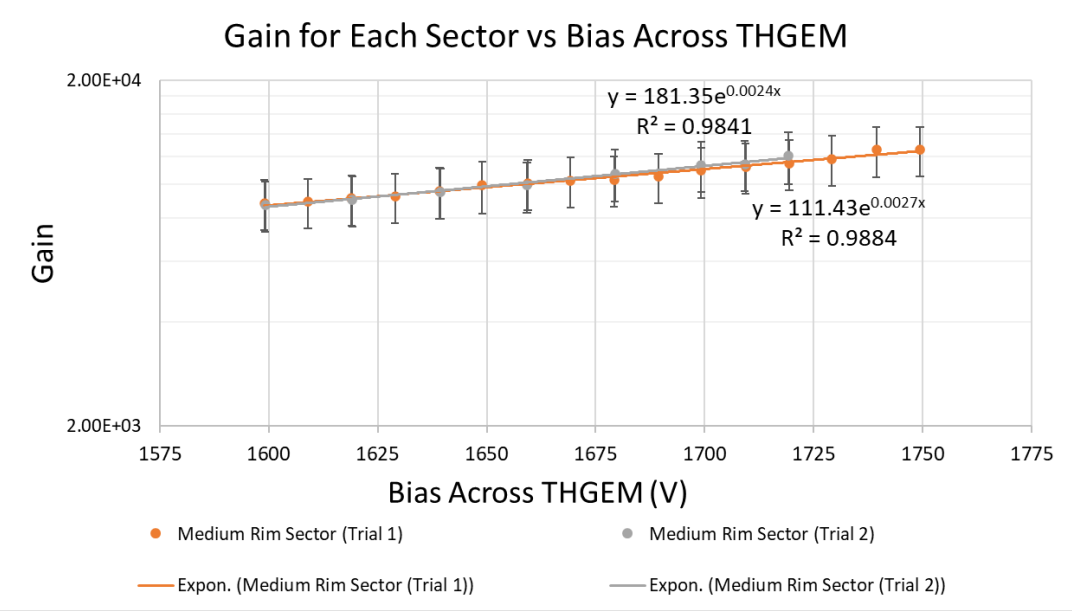

Figure 68: Gain vs Bias across the THGEM for both middle sector trials

As can be seen in Figure 68 above, the gas gain response is nearly identical between the two trials. After this series of tests with the middle sector, it was decided that the other two THGEM sectors would be tested as well, this time using Fe-55 as the X-ray source instead of the X-ray gun.

The switch to Fe-55 was made in part out of an abundance of caution regarding the use of the X-ray gun on the THGEM board. The region with holes having a 2 mm rim annulus, or, large rim sector, was tested next.

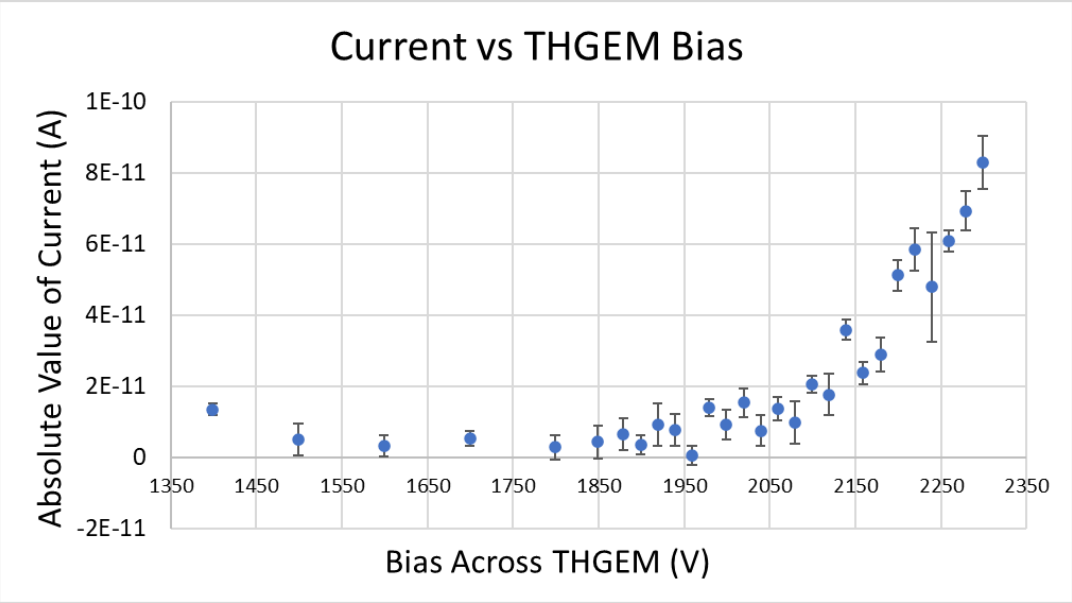

Figure 69: Absolute value of the current readings vs the bias voltage across large rim THGEM under Fe-55

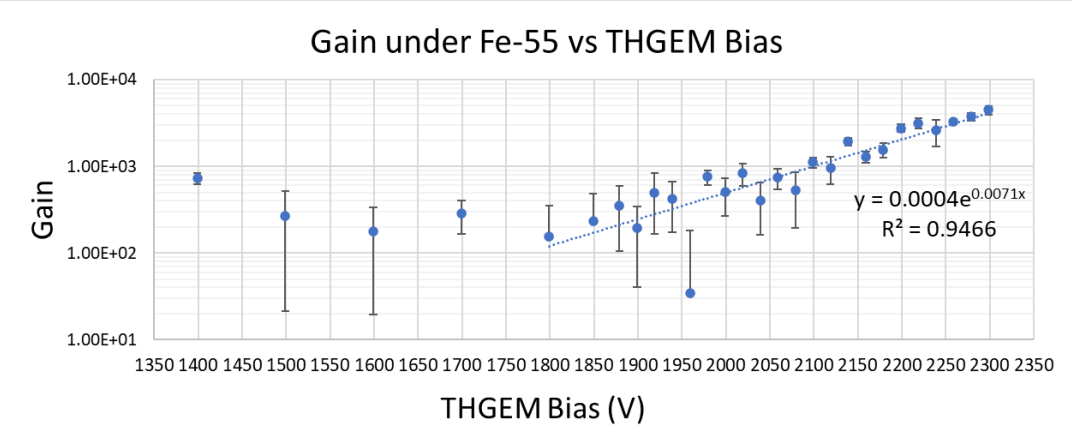

Figure 70: Gain vs bias voltage across the large rim THGEM under Fe-55. Error bars are present but small compared to axis units. Missing lower bars are due to not being able to cross 0 on a log plot.

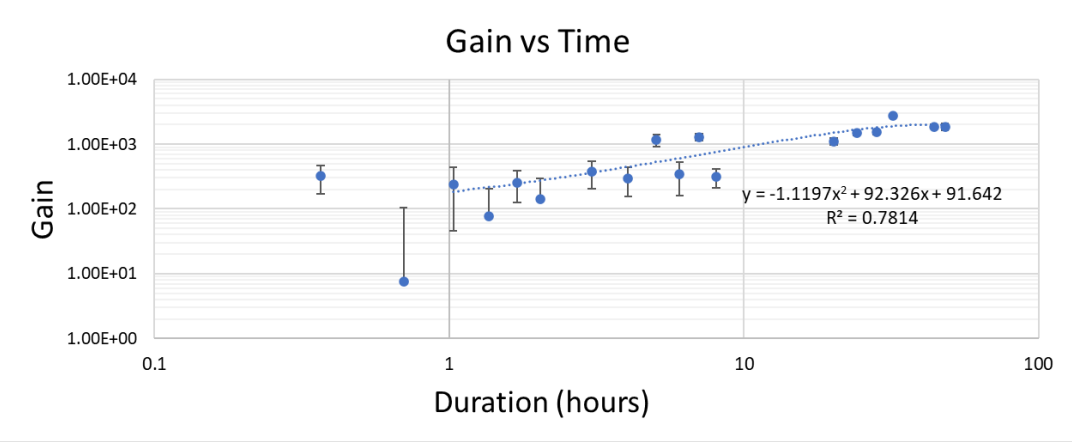

Figure 71: Evolution of the gain in the large rim sector over a 48-hour period under Fe-55 at a 2120V bias across the THGEM. Error bars are present but, in some cases, small compared to axis units. Missing lower bars are due to not being able to cross 0 on a log plot.

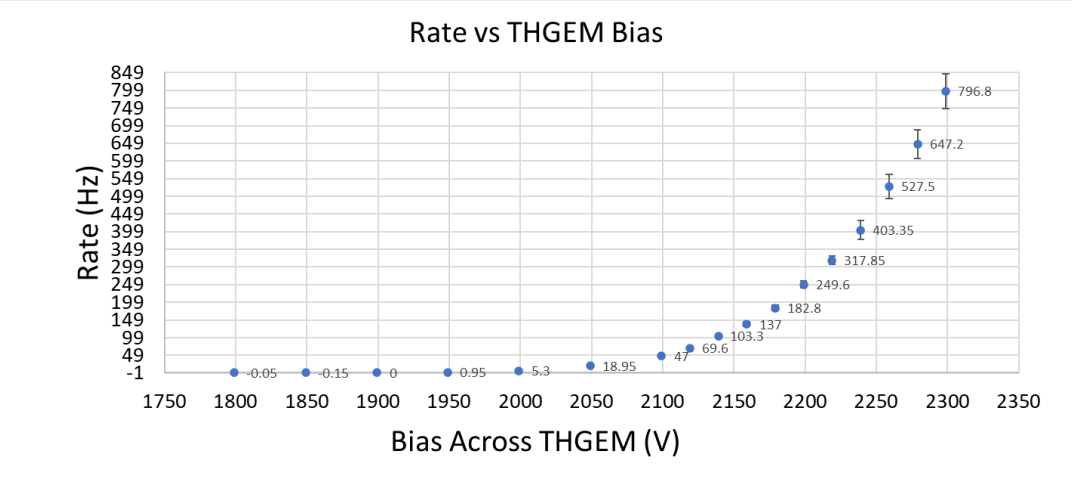

Figure 72: Rate vs Bias Voltage across large rim THGEM under Fe-55. Error bars are present but small compared to axis units.

The incident rate used in the gain calculations for this large rim annulus sector irradiated using Fe-55 was taken to be 591.22 ± 8.20 Hz using the method shown in Figure 37. Figure 69 and Figure 72 show the current and rate responses, respectively. These values were found by testing with source on and with source off and taking the difference. In the case of the current measurements, the absolute

values of the differences in current was used. The gain was then calculated and plotted, and as can be seen in Figure 70, increases exponentially above 1799V in the manner shown in the plot. The highest gain level found for this sector of the detector under these conditions was on the order of 2×10^3.

As shown in Figure 71, the gain of the detector while held at a THGEM bias voltage of 2120V under Fe-55 across a 48-hour period drops from its initial level for at least the first 42 minutes, but by the end of the first hour, it has increased once more to close to its original level, and then begins to increase over time to a gain on the order of 2×10^3 (note that both axes are on a logarithmic scale).

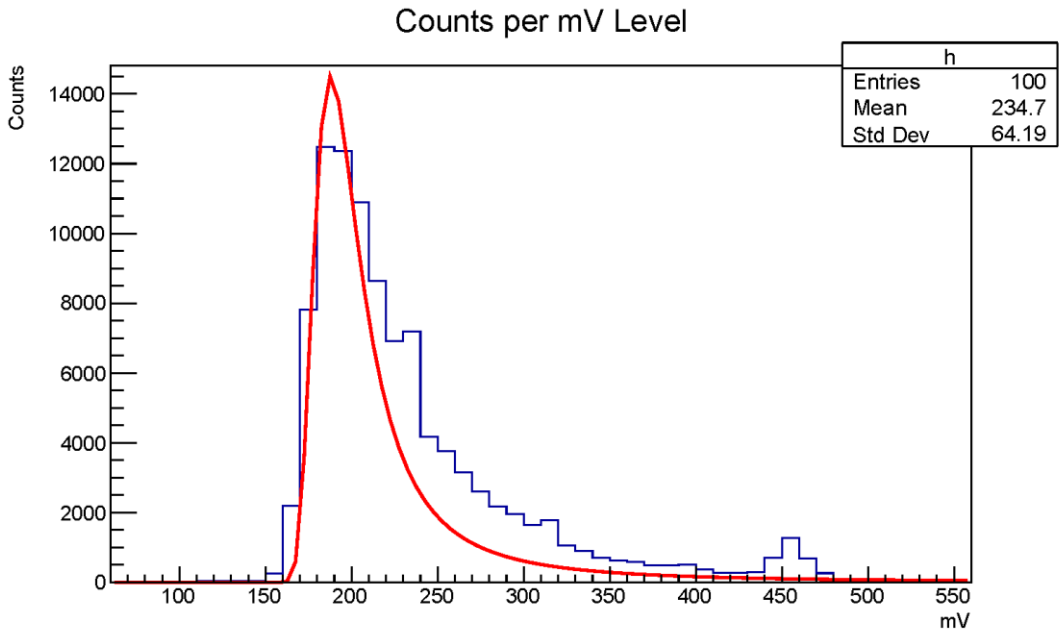

Figure 73: Pulse height distribution for the large rim board sector under Fe-55 taken at a bias voltage of 2200V. The most probable value given by the Landau fit was 189.83 ± 0.10 mV.

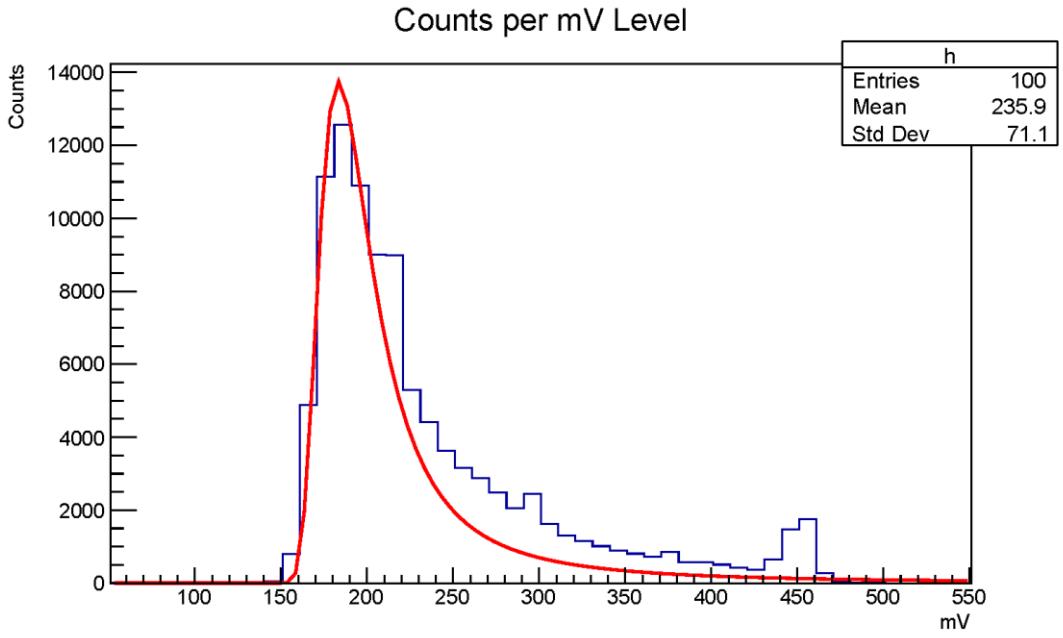

Figure 74: Pulse height distribution for the large rim board sector under Fe-55 taken at a bias voltage of 2120V toward the end of the 48-hour test. The most probably value given by the Landau fit was 185.54 ± 0.09 mV.

The histograms in Figure 73 and Figure 74 were taken during gain testing and 48-hour testing of the large rim sector, respectively. They both have a primary peak around 190 mV, and fit, as expected, to a Landau distribution.

After this test, the detector was configured to test the small rim sector, which has 1 mm rims. The same test to investigate the gain was conducted for this sector.

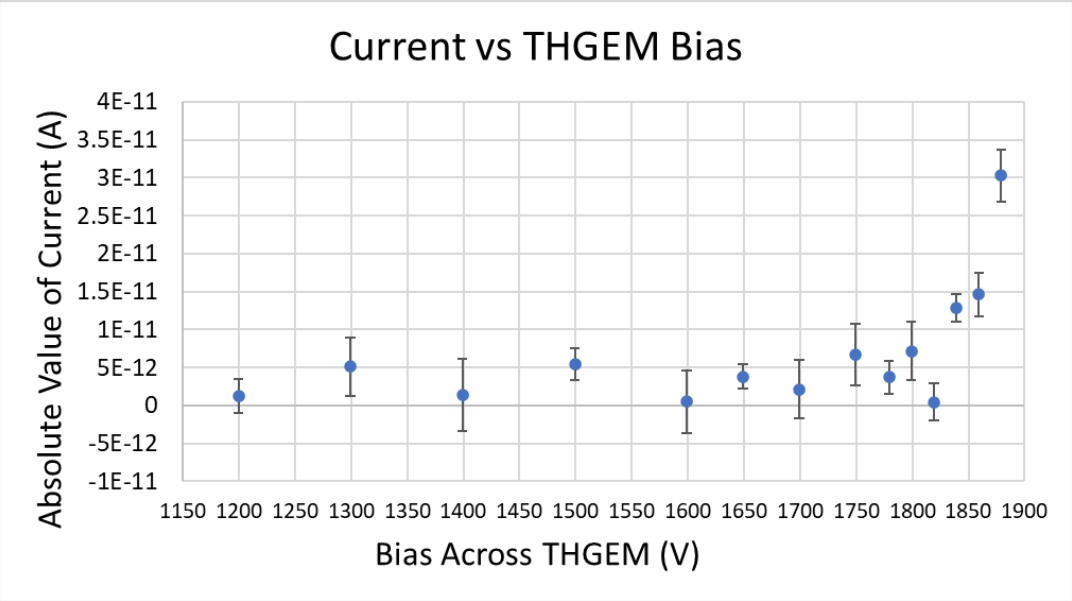

Figure 75: Absolute value of the difference in current between source-on and source-off vs the bias voltage across the small rim sector of the THGEM under Fe-55.

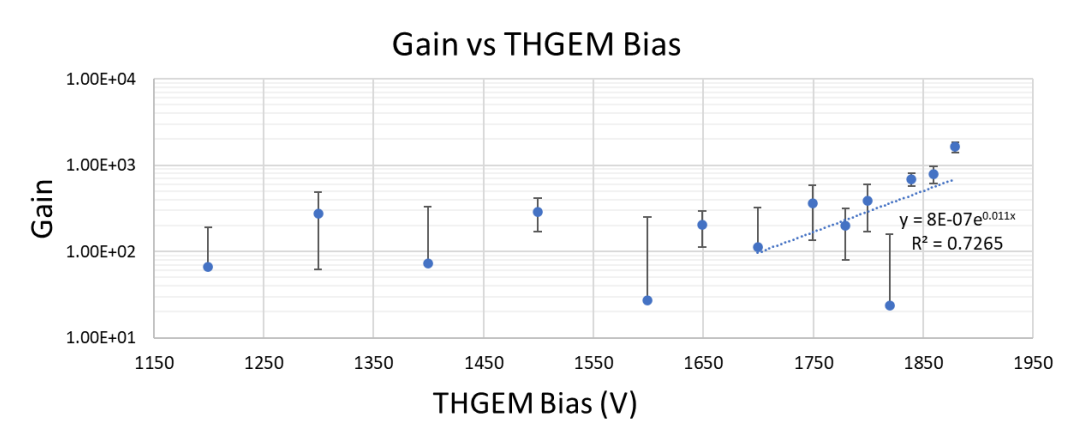

Figure 76: Gain vs bias across the small rim sector of the THGEM under Fe-55. Missing lower error bars are due to not being able to cross 0 on a log plot.

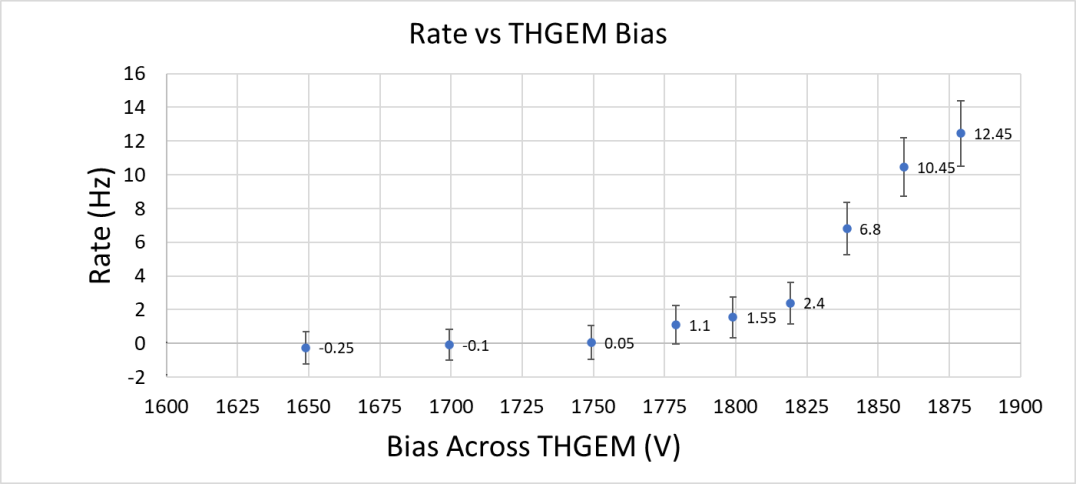

Figure 77: Count rate vs bias across the small rim sector of the THGEM under Fe-55

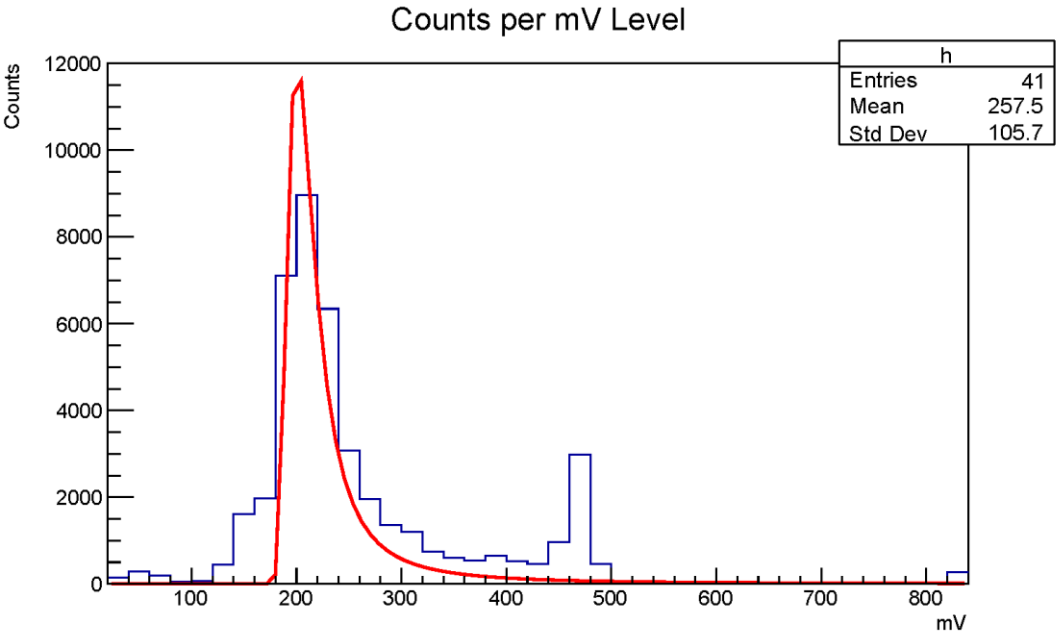

Figure 78: Pulse height distribution for the small rim board sector under Fe-55 taken at a bias voltage of 1840V. The most probably value given by the Landau fit was 202.41 ± 0.11 mV

As we can see in Figure 76 above, the gain for this sector of the board was found to be lower than the other sectors, only reaching 10^3 gain at the final data point. The most probable value given by the Landau fit of the histogram

representing the pulse height distribution for the small rim sector operated under Fe-55 at 1840V, shown in Figure 78, was 202.41 ± 0.11 mV.

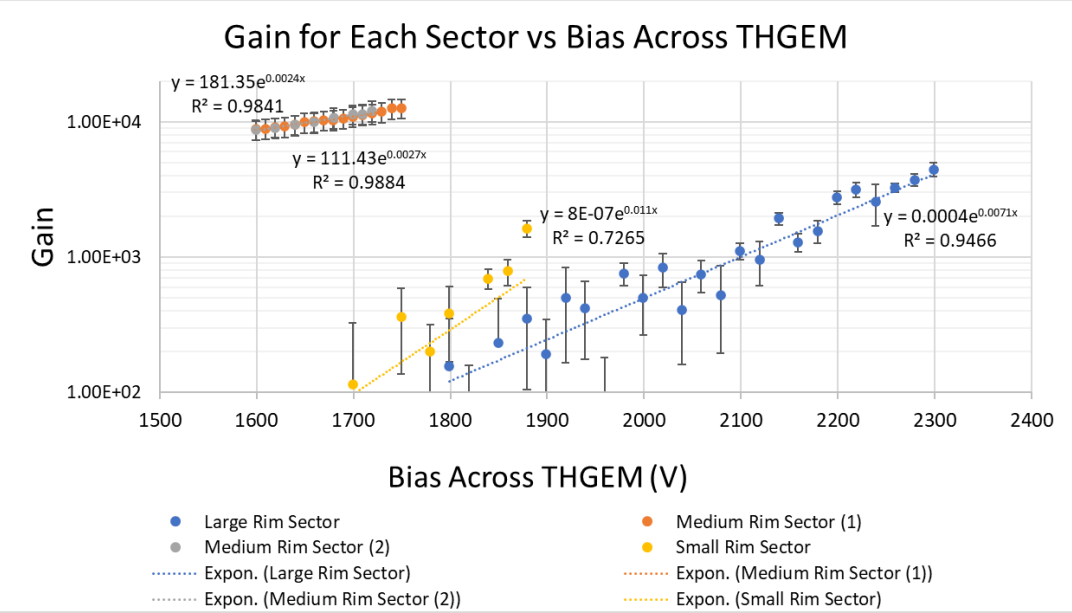

Figure 79: Gain curves for each region of the board. The small and large rim sectors were tested using Fe-55, while the medium rim sector was tested using the X-ray gun. Missing lower error bars are due to not being able to cross 0 on a log plot.

After these tests were completed, each of the gain curves were trimmed down to the voltage regions which demonstrated their exponential gain response and then compiled into one plot, as can be seen in Figure 79 above.

We see that the medium rim THGEM sector was able to achieve higher gains than the other two sectors, being the only one to achieve 10^4 gain. It must be noted however that this sector utilized the X-ray gun as the X-ray source instead of Fe-55, which could be a partial explanation for why this region achieved higher gain and at lower voltages than the other sectors, as the X-ray gun emits higher energy X-rays.

The small rim sector and the large rim sector did, however, both use Fe-55 as the X-ray source, and we see that the small rim sector did have somewhat higher gain at lower voltages than the large rim sector, but the large rim sector was overall able to achieve much higher voltages than the small rim sector, and therefore was able to achieve a higher gain in the long run. Another factor at play may be the long-term functionality of the detector.

Each THGEM sector was then tested under pure CO_2 (Figure 80) in order to observe the functionality of the detector without any effect of amplification due to electron avalanche. To do this, the detector was reconfigured to read off of the bottom electrode of the THGEM instead of the readout board. This was necessary because when reading off of the readout, the sensitive area of the THGEM was not fully covered due to the positions of the strips and associated Panasonic connectors relative to the placement of the THGEM itself. By reading off of the bottom electrode, data was gathered for the full sensitive area of the THGEM. The small sector was tested first, powered to constant 2.6 kV/cm and 1.8 kV/cm induction and drift fields, respectively, and taken through several THGEM bias voltage levels. A rate of 0 Hz was found regardless of the bias voltage across the THGEM, which is reasonable as under CO_2 there will be no electron avalanche. The medium and large rim sectors at this time however, did not function as smoothly. The medium rim sector, at just 1000V THGEM bias and a lower than standard drift field showed instability on both the bottom THGEM electrode, causing it to go overvoltage, as

well as on the scope. The large rim sector performed better than the medium rim sector, but still at 1000V THGEM bias had large and long-lasting pulses which prevented reasonable measurement of the rate response. These final observations suggest that there is some physical issue with these THGEM sectors after completion of the tests, which may have been exacerbated by electron amplification under Ar/CO_2.

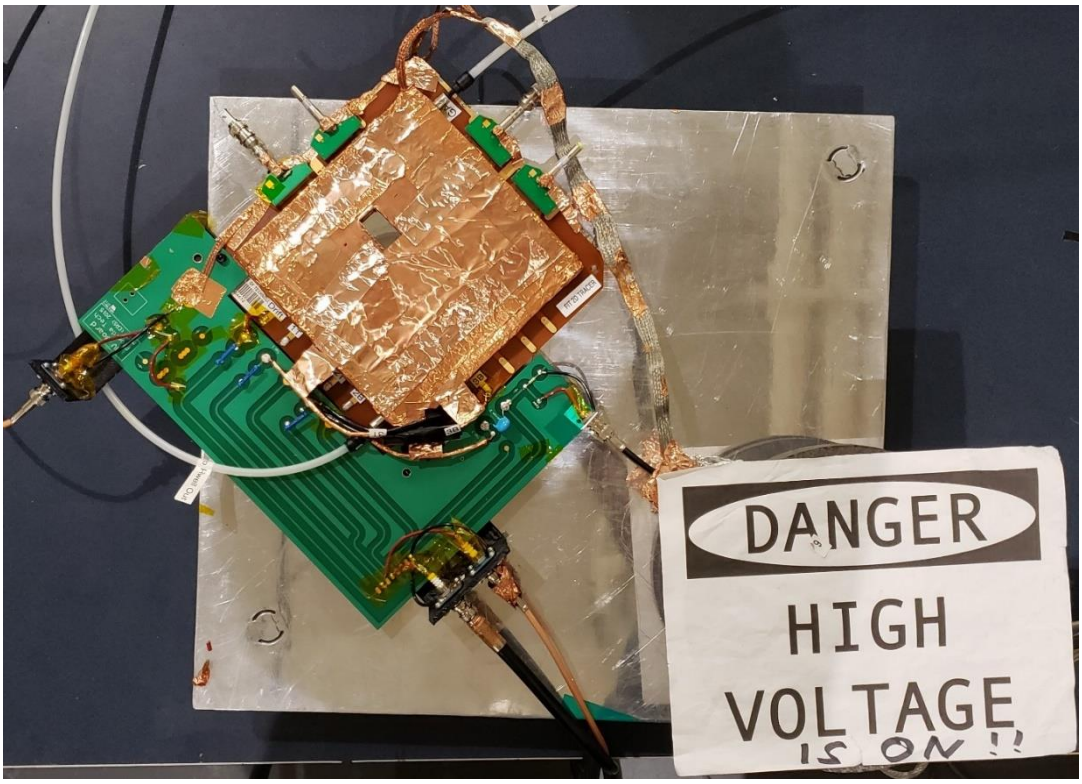

Figure 80: Detector in large rim sector testing configuration for testing functionality under pure CO_2, being read off of the THGEM Bottom electrode directly.

Long-term Tests

At this stage, several “long-term tests” were conducted. These were tests that typically had the THGEM under Fe-55 irradiation for a period of 5-48 hours. Observations were made regarding the HV stability, the long-term evolution of the trigger count rate and the gain, as well as the behavior of positive-to-negative “transitions,” which were moments of large pulses often with negative components, primarily read off of the pre-amp signal and considered potential sparks. Depending on the particular test, trigger count rate, current, and transition rate were measured or calculated at regular intervals. In order to count the transitions, a second timing SCA (ORTEC 550) was added and connected to the timing channel of the pre-amplifer. When setting up for a test, the threshold of this SCA was set to a value high enough that it was considered unlikely to come from genuine signals or noise, but from the positive component of these large transitions (the timing SCA is unable to measure negative pulses). This configuration resulted in a counter for the transitions, which could include sparks or other phenomena. For this first long-term test, drift and induction fields of 3kV/cm and a bias voltage across the THGEM of 2000V were used in all trials, as well as Fe-55 being the X-ray source. This test was also conducted on the middle sector, read using Lemo D.

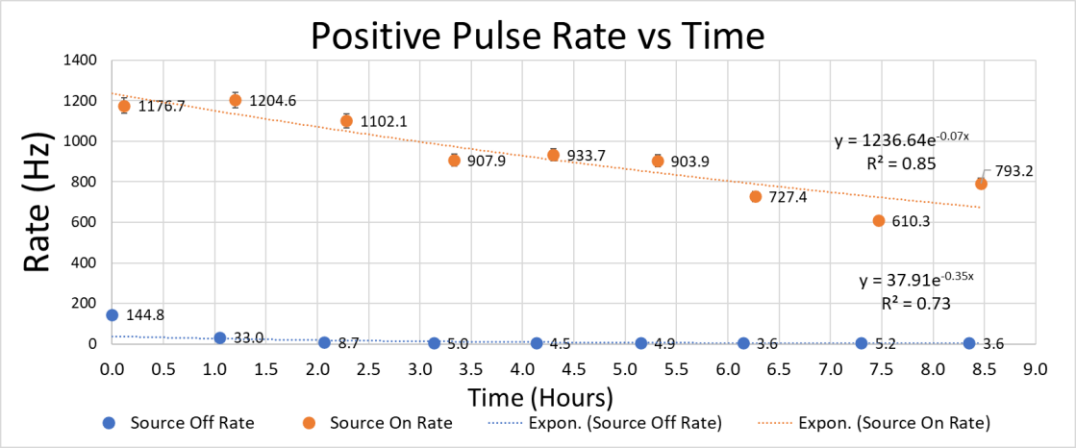

Figure 81: Rate of positive pulses over time. Note: error bars are present, but relatively small compared to axis units. Test done on Middle sector, read via Lemo D.

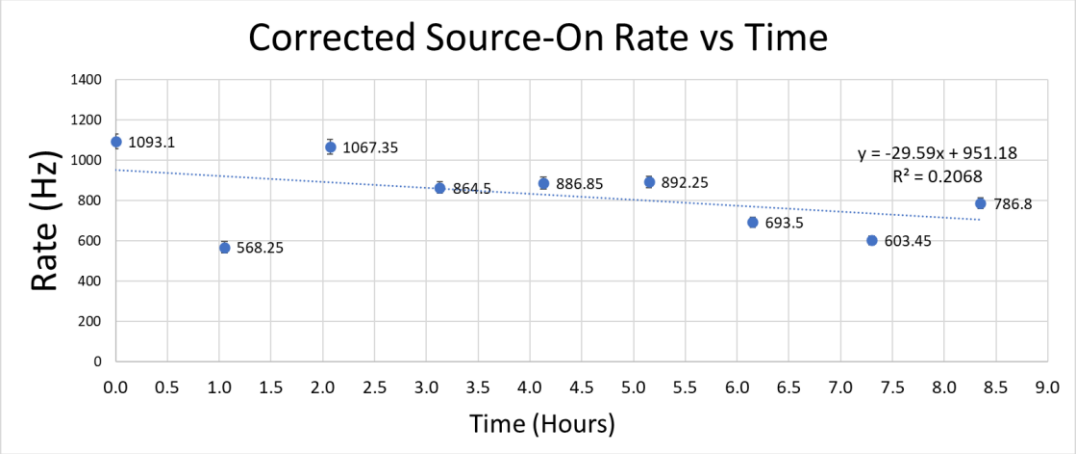

Figure 82: "Corrected" rate of source-on counts vs trial number. Note: error bars are present, but relatively small compared to axis units. Test done on Middle sector, read via Lemo D.

As can be seen in the plots (Figure 81-82) above, based on this first long-term study of the THGEM detector behavior, there is a general trend of the count rate decreasing over time. This trend seems to fit a slightly exponential decrease moreso than a linear one (Figure 81).

The long term test was done again, this time with the Fe-55 source being kept on the entire time. This was important because monitoring the long-term

behavior of the gas gain with the charging up of the insulating material of the THGEM caused by constant irradiation was one purpose of our investigation. The current and potential monitor information was also kept. Due to the nature of this HV module, there was always at least a bit of leakage current registered as long as HV was turned on (see Figure 84), regardless of any configuration of the THGEM. These values remained fairly constant the entire time, besides minor momentary fluctuations. The primary times when these values weren't constant were in the moments of a discharge, which would cause the monitors to fluctuate, particularly for the Bottom electrode, but also somewhat for the Top electrode. The drift was only minorly affected. These occurances are not represented in the plots regarding the HV monitor (Figure 83 and Figure 84), but information regarding discharges is contained within the plot shown in Figure 85 regarding positive-to-negative transitions, which can be seen below.

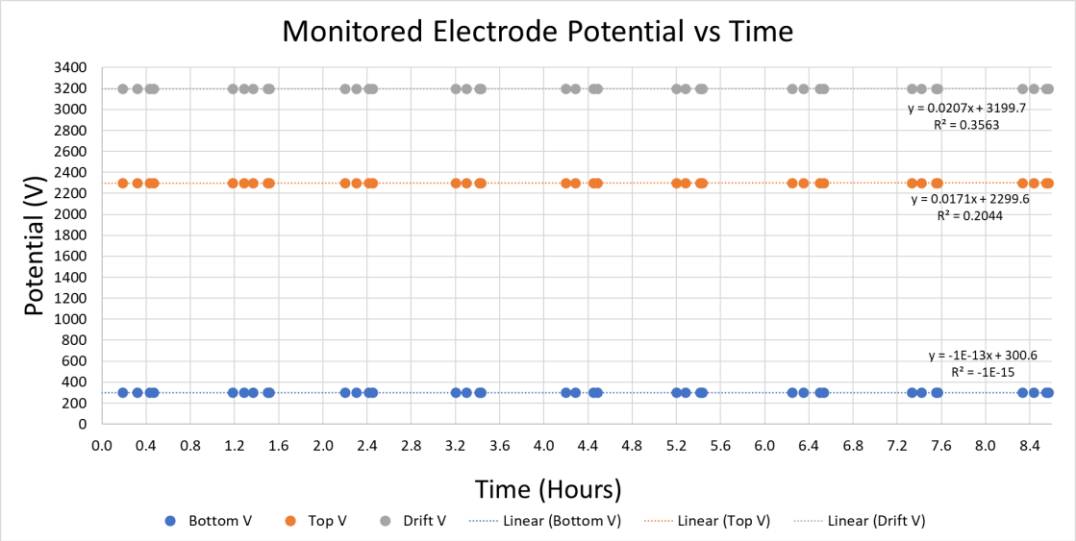

Figure 83: Monitored stable electrode potentials over time. Error bars are present but small compared to axis units.

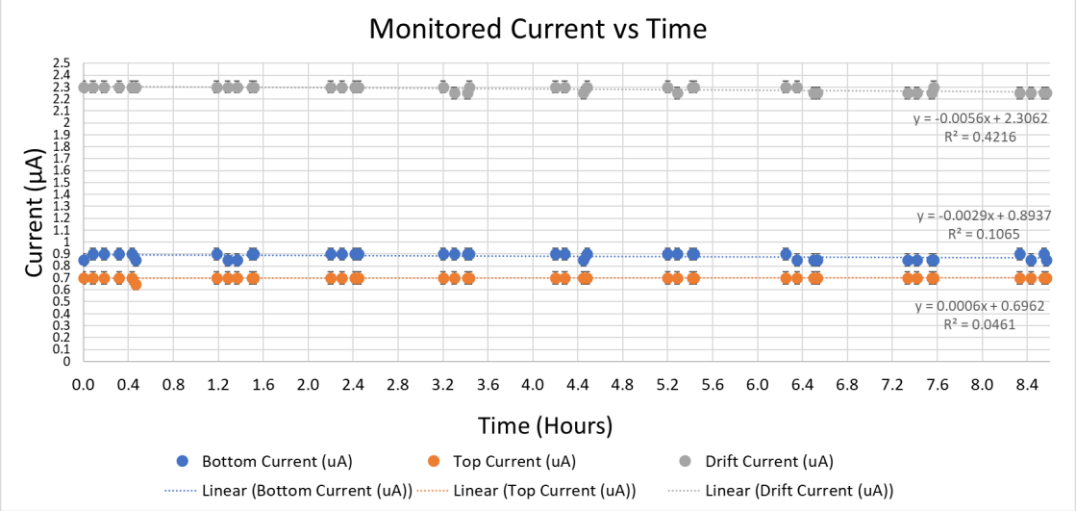

Figure 84: Stable leakage currents on the current monitor of the HV electrodes over time. Error bars are present but small compared to axis units.

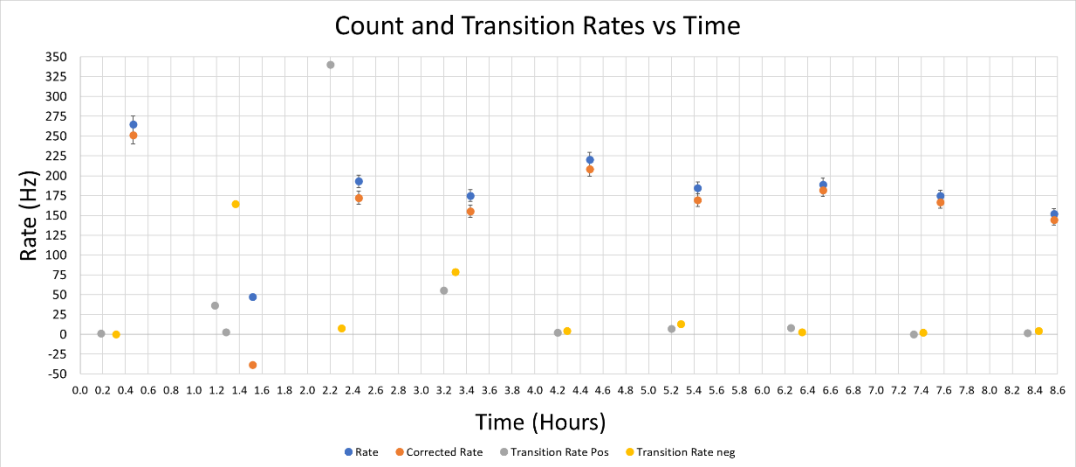

Figure 85: Rates of counts and large transitions, as well as corrected rate over time. When corrected rate is negative, this means that there was a greater rate found with the amplifier set to the negative polarity than when set to the positive polarity. Note: error bars are present, but relatively small compared to axis units.

As can be seen by the plot of the second long-term test above (Figure 85), there is generally a downward trend of the values in count rate, as well as transitions, though transitions appear to plateau. Transitions did rise signficantly early in the test before falling again. The count rate also had a significant drop before rising back again and beginning a fairly stable downward slope.

The third long-term test to be conducted was one over an approximately 48-hour period, where the detector would be constantly powered at 3kV/cm drift and induction fields, and 2000V bias across the THGEM, and irradiated with Fe-55. Trials were conducted more frequently for approximately the first two hours, then once per hour for the next six hours. The following day trials were conducted every four hours until the late evening, and the last two trials were completed the day after.

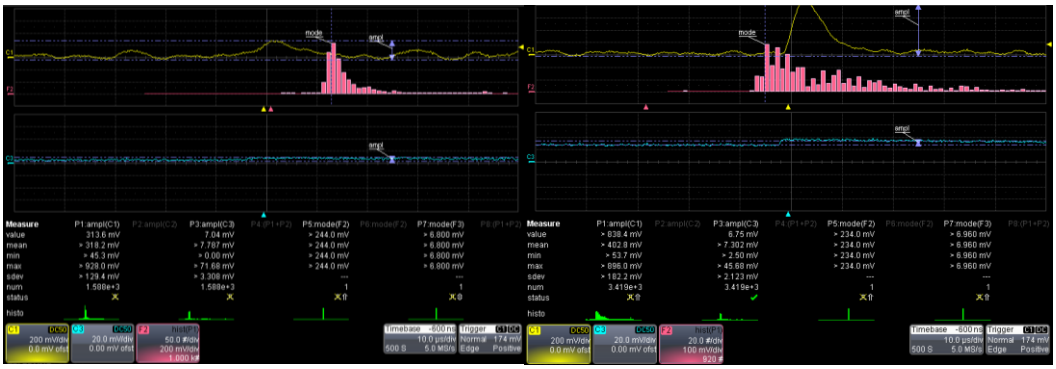

Figure 86: Scope shots of the signal through the pre-amp and amplifier (C1, yellow) and through just the pre-amp (C3, cyan). Histograms of the amplitudes of C1 shown at the beginning of the two-day study (left) and at the end of the two-day study (right), positive polarity

Figure 87: Scope shots of the signal through the pre-amp and amplifier (C1, yellow) and through just the pre-amp (C3, cyan). Histograms of the amplitudes of C1 shown at the beginning of the two-day study (left) and at the end of the two-day study (right), negative polarity

Above (Figure 86-87) are histograms of the amplitudes of the signal given by C1, which is the detector output read through the panasonic-to-lemo adapter, then through the pre-amplifier, then through the dual amplifer. They were taken at the beginning and end of the two-day study. The mode for each histogram is similar at the end as it was in the beginning for both positive and negative amplifier polarities, meaning the most frequent pulse height stayed similar, though not identical. There was an approximately 60% decrease in the counts at the mode for the positive polarity, and about a 47% decrease for the negative polarity. This,

along with the increased time required to collect samples, indicates a rate decrease, as well as a decrease in the proportion of the pulse heights near those of the mode relative to other detected pulse heights over time.

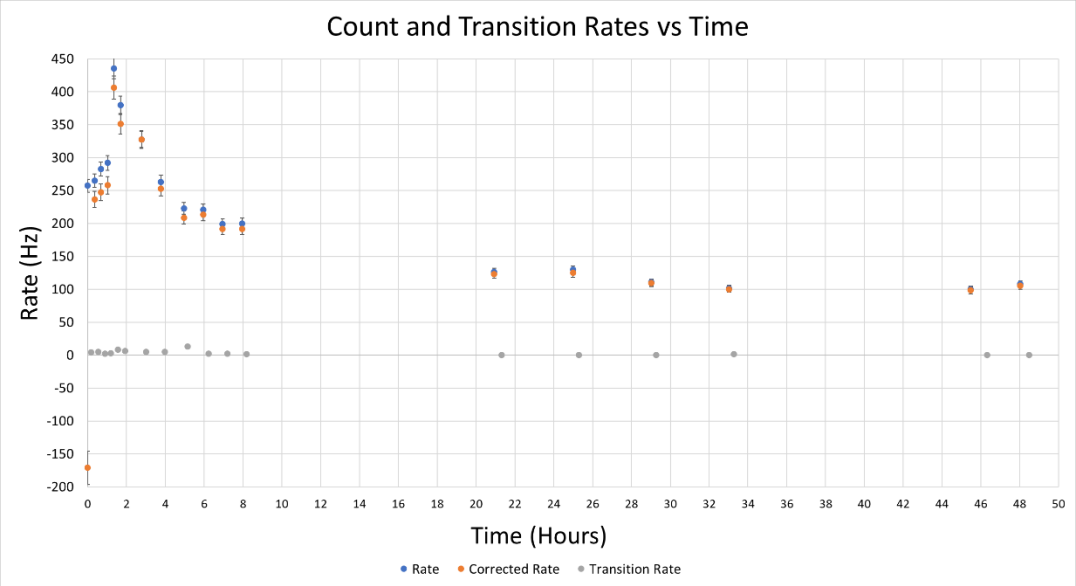

Figure 88: Count and transition rate behavior over a 48-hour period. Note: some error bars may be hard to see due to size relative to axis scale.

As can be readily seen in the plot (Figure 88) above, the count rate has a quick rise before beginning to fall for the remainder of the testing period. There also appears to be a plateau in the rate of around 100 Hz after approximately 24 hours. It can also be seen on the plot that the difference between the rate and the corrected rate, which is the rate of negative pulses, appears to get smaller over time, until around the time of the plateau region, they are approximately the same value. This means the rate of those negative pulses decreases over time. This is in line with what was noticed from observing the scope trace: that the number of visible encounters with the large, long-lasting overshoots into the positive region of

negative pulses tends to decrease over time, which implies that the negative pulses would be decreasing as well. The rate of transitions also follows a similar shape as those of Figure 85, but at much lower magnitudes. We were curious if this peak and then fall in the rates was a genuine manner of behavior, or just something observed at that time, so the experiment was repeated in order to confirm.

As the primary objective was to investigate the initial behavior under high voltage, the duration of this fourth long-term test was reduced to a few hours. However, unlike the previous studies, the signal current was also monitored throughout testing using a Keithley Picoammeter (Figure 89) so that, by utilizing a reference source-off current and rate from the end of the trial, combined with the average count rate of those taken during the study, an approximation of the detector gain over time at these HV settings could be determined.

Figure 89: Keithley Picoammeter used for signal current measurements

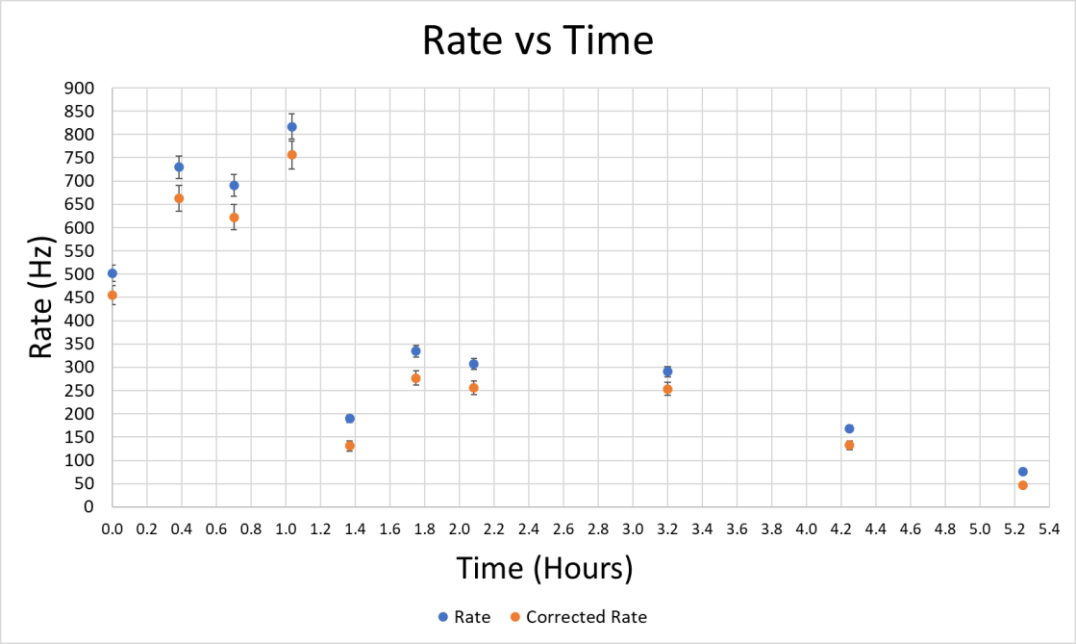

Figure 90: Count Rate (and corrected version) vs Time for second test. Error bars are present but, in some cases, small compared to axis units.

As can been seen in Figure 90 above, the behavior of the count rate is indeed very similar to that seen in Figure 88 during the 48-hour study. This confirms that for approximately the first hour under HV and irradiation, the rate increases, and then afterward it begins to decrease until reaching a plateau. This could be due to the charging up of the insulating THGEM material over time.

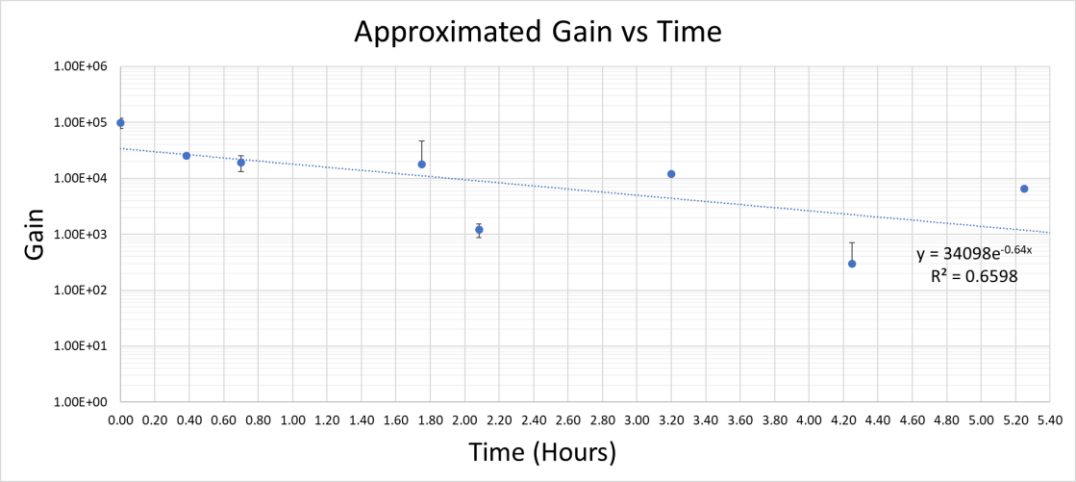

Figure 91: Approximated Gain over time during the fourth long-term study. Error bars are present but, in some cases, small compared to axis units. Missing lower bars are the result of not being able to cross 0 on a log plot.

Due to the nature of the calculations, the margin of error is somewhat high in the plot (Figure 91) above. A reference "source-off" set of values was taken for use in the calculation of Gain. Specifically, the source-off signal current value was subtracted from each measured source-on signal current, forming the current values "I" in the gas gain equation. Additionally, for the incident rate value (Equ.1), the rate calculated from counts given by the Geiger counter while under the detector cover and a drift foil was used (see discussion surrounding Figure 37). That rate, subtracting the source-off value from the source-on value, was 591.22 ± 8.20 Hz. We see that the gain appears to decrease exponentially over time when held at a constant voltage, decreasing over an order of magnitude throughout the course of the study.

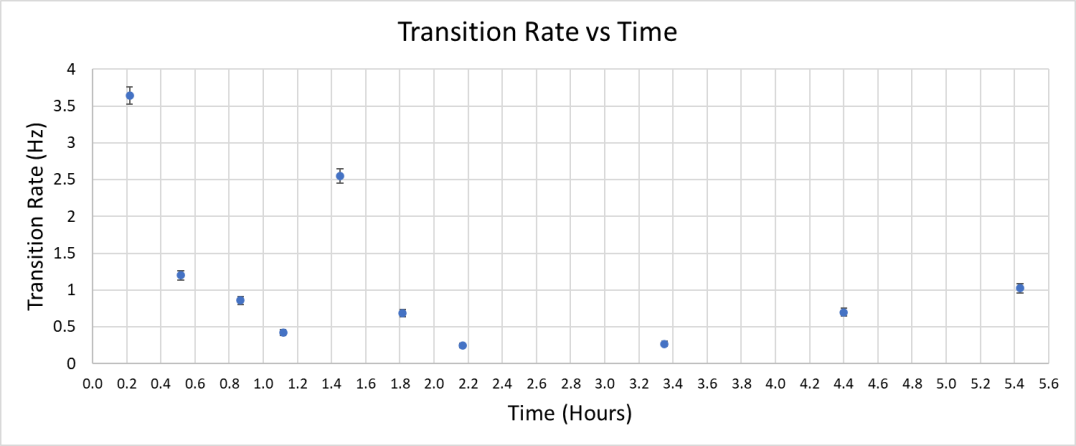

Figure 92: Rate of transitions over time. Error bars are present but small compared to axis units.

As for the transition count rate (Figure 92) as registered by our second timing-SCA setup, the rate was fairly low throughout the study. It does appear to have a linear decrease in rate over the first two hours, though there was a somewhat upward trend toward the end.

Chapter 6

Summary and Conclusions

All of the data collected would indicate that in optimal conditions, the maximum functional bias voltage the detector is able to achieve increases as the rim annulus increases. While the small rim sector was able to achieve higher voltage levels than the medium rim sector in the final gain curve tests (although when a 48-hour test was attempted on the small rim sector after its gain measurement test, it was no longer able to go beyond 1730V), it should be noted that toward the beginning of the usage of the detector, the small rim sector was able to achieve up to approximately 1900V-2000V before heavy discharges occurred. Due to this limitation, the detector was then switched over to using the medium rim sector, and was thus now able to achieve up to approximately 2200-2300V. In fact, recall that the detector was held stably at 2100V with higher 3 kV/cm drift and induction fields in the early “long-term” studies. Conditions which were no longer possible by the time the gain curves were found.

The Fe-55 study shows that the large rim sector can be operated at even 2300V, indicating greater stability at that voltage level than the other sectors. These results indicate that the detector is able to achieve higher bias voltages across the THGEM with larger rim sizes, however, the detector also seems to reduce in functionality over time. In fact, by the end of this period of research, the middle

sector, which was most heavily used, was no longer able to achieve the bias voltages which represent the areas where we see gain. In testing under pure CO_2 at the end of the study, while the small rim sector performed well, the other two did not. These final observations suggest that there is some physical issue with those THGEM sectors after completion of the tests, which may have been exacerbated by the electron amplification that occurs under Ar/CO_2.

As for the gain, we see that 10^2 to 10^3 gains are the most common levels. However, the medium rim sector was able to briefly achieve 10^4 gain, with both trials showing nearly identical results. It should be noted that that sector alone was tested using our Mini-X X-ray gun, which has higher energy X-rays, which likely played a role in how that sector was able to achieve higher gains at far lower voltages than the other two sectors. The small rim sector, which was tested using Fe-55 along with the large rim sector, was able to achieve higher gains at lower voltages than the large rim sector. However, the maximum bias voltage the large rim sector was able to achieve safely was far greater than that of either of the other two sectors, so it was ultimately able to achieve higher gain than the small rim sector.

The estimated gain for the middle sector over approximately 5.2 hours shows a decreasing trend. The gain vs. time plot for the large rim sector however shows an increasing trend over time that flattens out after approximately the 10-hour mark, which is similar to the results of a Sauli study shown in [4] (aside from

the initial drop in gain before rising back up by the first hour mark). This suggests that in order to have the most stability in the gain, it would be best to allow the detector to remain powered for at least 10 hours. This could be an effect of the charging up of the dielectric material in the rims.

While there are some concerns with its long-term functionality, it can be seen from the research presented that a 3D-printed Thick GEM can serve as a functioning GEM in a detector.

References

[1] Sauli, F. (2016). The gas electron multiplier (GEM): Operating principles and applications. *Nuclear Instruments and Methods in Physics Research Section A: Accelerators, Spectrometers, Detectors and Associated Equipment, 805,* 2-24. doi:10.1016/j.nima.2015.07.060

[2] Sauli, F. (2021). *Micro-pattern gaseous detectors principles of operation and applications.* Singapore: World Scientific.

[3] Sauli, F. (2014). *Gaseous Radiation Detectors: Fundamentals and Applications*. Cambridge: Cambridge University Press.

[4] Chechik, R. *et al* (2006, April). *Progress in Thick GEM-like (THGEM)-based Detectors* [PPT]. SLAC.

[5] Rahmani, M. (2017). *Quality Control of the Large-area GEM Detectors at Production Sites for the CMS Muon Endcap Upgrade*. APS April Meeting 2017. Retrieved from https://meetings.aps.org/Meeting/APR17/Session/S9.8

[6] Detecting radioactivity – the Geiger Muller Tube – Pass My Exams: Easy exam revision notes for GSCE Physics. (n.d.). Retrieved from http://www.passmyexams.co.uk/GCSE/physics/detecting-radioactivity-the-geiger-muller-tube.html

[7] Alexeev, M. *et al* (2015). The gain in Thick GEM multipliers and its time evolution. *Journal of Instrumentation, 10*(03). doi:10.1088/1748-0221/10/03/p03026

Appendix

Tables for First Long-term Test

Table 3: First Long-term Test Trial 1, Fe-55 on and off

Time (hours)	Source On/Off	Trial	Amp Polarity	Counts	Transitions	Duration (s)	Count Rate (Hz)	Transitions Rate (Hz)	Count Rate Error (Hz)	Transitions Rate Error (Hz)
0.00										
0.12	off	1	positive	2896		20	144.8		6.31	
0.18	off	1	negative	1270		20	63.5		3.37	
0.23	on	1	positive	23534		20	1176.7		37.09	
0.27	on	1	negative	1672		20	83.6		4.13	
0.45	on	1	positive		4	30		0.13		0.07
0.48	on	1	positive		10	30		0.33		0.11
0.50	on	1	negative		2	30		0.07		0.05
0.53	off	1	positive		0	30		0.00		0.00
0.55	off	1	negative		0	30		0.00		0.00

Table 4: First Long-term Test Trial 2, Fe-55 on and off

Time (hours)	Source On/Off	Trial	Amp Polarity	Counts	Transitions	Duration (s)	Count Rate (Hz)	Transitions Rate (Hz)	Count Rate Error (Hz)	Transitions Rate Error (Hz)
1.17	off	2	positive	659		20	33.0		2.11	
1.22	off	2	negative	961		20	48.1		2.75	
1.30	on	2	negative	12726		20	636.3		21.55	
1.32	on	2	positive	24091		20	1204.6		37.87	
1.37	on	2	positive		3	30		0.10		0.06
1.40	on	2	negative		4	30		0.13		0.07
1.42	off	2	negative		0	30		0.00		0.00
1.43	off	2	positive		0	30		0.00		0.00

Table 5: First Long-term Test Trial 3, Fe-55 on and off

Time (hours)	Source On/Off	Trial	Amp Polarity	Counts	Transitions	Duration (s)	Count Rate (Hz)	Transitions Rate (Hz)	Count Rate Error (Hz)	Transitions Rate Error (Hz)
2.18	off	3	positive	174		20	8.7		0.88	
2.27	off	3	negative	673		20	33.7		2.14	
2.35	on	3								
2.40	on	3	positive	22041		20	1102.1		34.97	
2.42	on	3	negative	694		20	34.7		2.18	
2.50	on	3	negative		3	30		0.10		0.06
2.52	on	3	positive		3	30		0.10		0.06
2.57	off	3	positive		0	30		0.00		0.00
2.60	off	3	negative		0	30		0.00		0.00

Table 6: First Long-term Test Trial 4, Fe-55 on and off

Time (hours)	Source On/Off	Trial	Amp Polarity	Counts	Transitions	Duration (s)	Count Rate (Hz)	Transitions Rate (Hz)	Count Rate Error (Hz)	Transitions Rate Error (Hz)
3.25	off	4	positive	99		20	5.0		0.62	
3.28	off	4	negative	291		20	14.6		1.22	
3.45	on	4	positive	18158		20	907.9		29.44	
3.48	on	4	negative	268		20	13.4		1.15	
3.52	on	4	negative		5	30		0.17		0.08
3.55	on	4	positive		7	30		0.23		0.09
3.58	off	4	positive		0	30		0.00		0.00
3.60	off	4	negative		0	30		0.00		0.00

Table 7: First Long-term Test Trial 5, Fe-55 on and off

Time (hours)	Source On/Off	Trial	Amp Polarity	Counts	Transitions	Duration (s)	Count Rate (Hz)	Transitions Rate (Hz)	Count Rate Error (Hz)	Transitions Rate Error (Hz)
4.25	off	5	positive	89		20	4.5		0.58	
4.30	off	5	negative	204		20	10.2		0.97	
4.37	on	5								
4.42	on	5	positive	18673		20	933.7		30.17	
4.43	on	5	negative	936		20	46.8		2.70	
4.52	on	5	positive		2	30		0.07		0.05
4.53	on	5	negative		1	30		0.03		0.03
4.58	off	5	negative		0	30		0.00		0.00
4.60	off	5	positive		0	30		0.00		0.00

Table 8: First Long-term Test Trial 6, Fe-55 on and off

Time (hours)	Source On/Off	Trial	Amp Polarity	Counts	Transitions	Duration (s)	Count Rate (Hz)	Transitions Rate (Hz)	Count Rate Error (Hz)	Transitions Rate Error (Hz)
5.27	off	6	positive	98		20	4.9		0.62	
5.33	off	6	negative	104		20	5.2		0.64	
5.38	on	6								
5.43	on	6	positive	18077		20	903.9		29.32	
5.48	on	6	negative	232		20	11.6		1.05	
5.55	on	6	negative		4	30		0.13		0.07
5.60	on	6	positive		3	30		0.10		0.06
5.62	off	6	positive		0	30		0.00		0.00
5.63	off	6	negative		0	30		0.00		0.00

Table 9: First Long-term Test Trial 7, Fe-55 on and off

Time (hours)	Source On/Off	Trial	Amp Polarity	Counts	Transitions	Duration (s)	Count Rate (Hz)	Transitions Rate (Hz)	Count Rate Error (Hz)	Transitions Rate Error (Hz)
6.27	off	7	positive	71		20	3.6		0.51	
6.28	off	7	negative	54		20	2.7		0.43	
6.32	on	7								
6.38	on	7	positive	14547		20	727.4		24.21	
6.42	on	7	negative	677		20	33.9		2.15	
6.55	on	7	negative		2	30		0.07		0.05
6.55	on	7	positive		3	30		0.10		0.06
6.60	off	7	postitive		0	30		0.00		0.00
6.62	off	7	negative		0	30		0.00		0.00

Table 10: First Long-term Test Trial 8, Fe-55 on and off

Time (hours)	Source On/Off	Trial	Amp Polarity	Counts	Transitions	Duration (s)	Count Rate (Hz)	Transitions Rate (Hz)	Count Rate Error (Hz)	Transitions Rate Error (Hz)
7.42	off	8	positive	104		20	5.2		0.64	
7.43	off	8	negative	24		20	1.2		0.27	
7.47	on	8								
7.57	on	8	negative	137		20	6.9		0.76	
7.58	on	8	positive	12206		20	610.3		20.78	
7.68	on	8	positive		1	30		0.03		0.03
7.70	on	8	negative		4	30		0.13		0.07
7.75	off	8	negative		0	30		0.00		0.00
7.77	off	8	positive		0	30		0.00		0.00

Table 11: First Long-term Test Trial 9, Fe-55 on and off

Time (hours)	Source On/Off	Trial	Amp Polarity	Counts	Transitions	Duration (s)	Count Rate (Hz)	Transitions Rate (Hz)	Count Rate Error (Hz)	Transitions Rate Error (Hz)
8.47	off	9	positive	72		20	3.6		0.51	
8.50	off	9	negative	128		20	6.4		0.73	
8.52	on	9								
8.58	on	9	positive	15864		20	793.2		26.13	
8.58	on	9	negative	128		20	6.4		0.73	
8.68	on	9	negative		0	30		0.00		0.00
8.73	on	9	positive		2	30		0.07		0.05
8.75	on	9								
8.87	off	9	positive		0	30		0.00		0.00
8.88	off	9	negative		0	30		0.00		0.00

Tables for Second Long-term Test:

Table 12: Second Long-term Test Trial 1, Fe-55 on

Time (Hours)	Bottom Current (uA)	Top Current (uA)	Drift Current (uA)	Bottom V	Top V	Drift V	Trial	Amp Polarity	Counts	Count Rate (Hz)	Transitions	Transitions Rate (Hz)	Duration (s)	Count Rate Error (Hz)	Transitions Rate Error (Hz)
0.00	0.85	0.7	2.3												
0.08	0.9	0.7	2.3												
0.18	0.9	0.7	2.3	300.6	2299.6	3199.6	1	positive			354	1.2	300		0.06
0.32	0.9	0.7	2.3	300.6	2299.6	3199.6	1	negative			0	0.0	300		0.00
0.43	0.9	0.7	2.3	300.6	2299.6	3199.6	1	negative	264	13.2			20	1.14	
0.47	0.85	0.65	2.3	300.6	2299.6	3199.6	1	positive	5293	264.7			20	10.25	

Table 13: Second Long-term Test Trial 2, Fe-55 on

Time (Hours)	Bottom Current (uA)	Top Current (uA)	Drift Current (uA)	Bottom V	Top V	Drift V	Trial	Amp Polarity	Counts	Count Rate (Hz)	Transitions	Transitions Rate (Hz)	Duration (s)	Count Rate Error (Hz)	Transitions Rate Error (Hz)
1.18	0.9	0.7	2.3	300.6	2299.6	3199.6	2	positive			10998	36.7	300		0.41
1.28	0.85	0.7	2.3	300.6	2299.8	3199.8	2	positive			928	3.1	300		0.11
1.37	0.85	0.7	2.3	300.6	2299.6	3199.6	2	negative			49405	164.7	300		1.02
1.50	0.9	0.7	2.3	300.6	2299.8	3199.8	2	negative	1719	86.0			20	4.22	
1.52	0.9	0.7	2.3	300.6	2299.6	3199.6	2	positive	950	47.5			20	2.73	

Table 14: Second Long-term Test Trial 3, Fe-55 on

Time (Hours)	Bottom Current (uA)	Top Current (uA)	Drift Current (uA)	Bottom V	Top V	Drift V	Trial	Amp Polarity	Counts	Count Rate (Hz)	Transitions	Transitions Rate (Hz)	Duration (s)	Count Rate Error (Hz)	Transitions Rate Error (Hz)
2.20	0.9	0.7	2.3	300.6	2299.8	3199.8	3	positive			102094	340.3	300		1.63
2.30	0.9	0.7	2.3	300.6	2299.8	3199.8	3	negative			2321	7.7	300		0.17
2.42	0.9	0.7	2.3	300.6	2299.6	3199.8	3	negative	417	20.9			20	1.54	
2.45	0.9	0.7	2.3	300.6	2299.6	3199.8	3	positive	3862	193.1			20	7.93	

Table 15: Second Long-term Test Trial 4, Fe-55 on

Time (Hours)	Bottom Current (uA)	Top Current (uA)	Drift Current (uA)	Bottom V	Top V	Drift V	Trial	Amp Polarity	Counts	Count Rate (Hz)	Transitions	Transitions Rate (Hz)	Duration (s)	Count Rate Error (Hz)	Transitions Rate Error (Hz)
3.20	0.9	0.7	2.3	300.6	2299.8	3199.6	4	positive			16619	55.4	300		0.52
3.30	0.9	0.7	2.25	300.6	2299.8	3199.8	4	negative			23623	78.7	300		0.64
3.42	0.9	0.7	2.25	300.6	2299.8	3199.6	4	negative	395	19.8			20	1.49	
3.43	0.9	0.7	2.3	300.6	2299.8	3199.6	4	positive	3501	175.1			20	7.33	

Table 16: Second Long-term Test Trial 5, Fe-55 on

Time (Hours)	Bottom Current (uA)	Top Current (uA)	Drift Current (uA)	Bottom V	Top V	Drift V	Trial	Amp Polarity	Counts	Count Rate (Hz)	Transitions	Transitions Rate (Hz)	Duration (s)	Count Rate Error (Hz)	Transitions Rate Error (Hz)
4.20	0.9	0.7	2.3	300.6	2299.6	3199.8	5	positive			732	2.4	300		0.09
4.28	0.9	0.7	2.3	300.6	2299.6	3199.8	5	negative			1312	4.4	300		0.13
4.45	0.85	0.7	2.25	300.6	2299.6	3199.8	5	negative	241	12.1			20	1.08	
4.48	0.9	0.7	2.3	300.6	2299.6	3199.8	5	positive	4410	220.5			20	8.83	

Table 17: Second Long-term Test Trial 6, Fe-55 on

Time (Hours)	Bottom Current (uA)	Top Current (uA)	Drift Current (uA)	Bottom V	Top V	Drift V	Trial	Amp Polarity	Counts	Count Rate (Hz)	Transitions	Transitions Rate (Hz)	Duration (s)	Count Rate Error (Hz)	Transitions Rate Error (Hz)
5.20	0.9	0.7	2.3	300.6	2299.6	3199.6	6	positive			2145	7.2	300		0.17
5.28	0.9	0.7	2.25	300.6	2299.8	3199.8	6	negative			3968	13.2	300		0.23
5.42	0.9	0.7	2.3	300.6	2299.6	3199.8	6	negative	306	15.3			20	1.26	
5.43	0.9	0.7	2.3	300.6	2299.8	3199.8	6	positive	3691	184.6			20	7.65	

Table 18: Second Long-term Test Trial 7, Fe-55 on

Time (Hours)	Bottom Current (uA)	Top Current (uA)	Drift Current (uA)	Bottom V	Top V	Drift V	Trial	Amp Polarity	Counts	Count Rate (Hz)	Transitions	Transitions Rate (Hz)	Duration (s)	Count Rate Error (Hz)	Transitions Rate Error (Hz)
6.25	0.9	0.7	2.3	300.6	2299.6	3199.8	7	positive			2453	8.2	300		0.18
6.35	0.85	0.7	2.3	300.6	2299.8	3199.8	7	negative			889	3.0	300		0.10
6.50	0.85	0.7	2.25	300.6	2299.8	3199.8	7	negative	139	7.0			20	0.76	
6.53	0.85	0.7	2.25	300.6	2299.6	3199.8	7	positive	3780	189.0			20	7.80	

Table 19: Second Long-term Test Trial 8, Fe-55 on

Time (Hours)	Bottom Current (uA)	Top Current (uA)	Drift Current (uA)	Bottom V	Top V	Drift V	Trial	Amp Polarity	Counts	Count Rate (Hz)	Transitions	Transitions Rate (Hz)	Duration (s)	Count Rate Error (Hz)	Transitions Rate Error (Hz)
7.33	0.85	0.7	2.25	300.6	2299.8	3199.8	8	positive			6	0.0	300		0.01
7.42	0.85	0.7	2.25	300.6	2299.8	3199.8	8	negative			659	2.2	300		0.09
7.55	0.85	0.7	2.25	300.6	2299.8	3199.8	8	negative	162	8.1			20	0.84	
7.57	0.85	0.7	2.3	300.6	2299.8	3199.8	8	positive	3494	174.7			20	7.32	

Table 20: Second Long-term Test Trial 9, Fe-55 on

Time (Hours)	Bottom Current (uA)	Top Current (uA)	Drift Current (uA)	Bottom V	Top V	Drift V	Trial	Amp Polarity	Counts	Count Rate (Hz)	Transitions	Transitions Rate (Hz)	Duration (s)	Count Rate Error (Hz)	Transitions Rate Error (Hz)
8.33	0.9	0.7	2.25	300.6	2299.8	3199.8	9	positive			575	1.9	300		0.08
8.43	0.85	0.7	2.25	300.6	2299.8	3199.8	9	negative			1292	4.3	300		0.13
8.55	0.9	0.7	2.25	300.6	2299.8	3199.8	9	negative	150	7.5			20	0.80	
8.57	0.85	0.7	2.25	300.6	2299.8	3199.8	9	positive	3043	152.2			20	6.56	

Tables for Third Long-term Test

Table 21: Third Long-term Test Trials 1-3, Fe-55 on

Time (Hours)	Trial	Polarity	Counts	Pos Transitions	Neg Transitions	Corrected Counts	Duration (s)	Rate (Hz)	Corrected Rate (Hz)	Transition Rate Pos (Hz)	Transition Rate Neg (Hz)	Rate Error (Hz)	Corrected Rate Error (Hz)
0.00	1	pos	5147			-3420	20	257.35	-171.00			10.02	25.36
0.05	1	neg	8567				20	428.35				15.34	
0.08	1	neg			1042		300				3.47		
0.18	1	pos		1546			345			4.48			
0.35	2	pos	5304			4729	20	265.20	236.45			10.27	12.19
0.38	2	neg	575				20	28.75				1.92	
0.45	2	neg			1786		307				5.82		
0.55	2	pos		1506			300			5.02			
0.68	3	pos	5653			4953	20	282.65	247.65			10.83	13.02
0.72	3	neg	700				20	35.00				2.20	
0.80	3	neg			3289		300				10.96		
0.88	3	pos		754			300			2.51			

Table 22: Third Long-term Test Trials 4-6, Fe-55 on

Time (Hours)	Trial	Amp Polarity	Counts	Pos Transitions	Neg Transitions	Corrected Counts	Duration (s)	Rate (Hz)	Corrected Rate (Hz)	Transition Rate Pos (Hz)	Transition Rate Neg (Hz)	Rate Error (Hz)	Corrected Rate Error (Hz)
1.02	4	pos	5840			5160	20	292.00	258.00			11.12	13.27
1.07	4	neg	680				20	34.00				2.15	
1.10	4	neg			2597		300				8.66		
1.18	4	pos		886			300			2.95			
1.35	5	pos	8713			8130	20	435.65	406.50			15.56	17.49
1.37	5	neg	583				20	29.15				1.94	
1.47	5	neg			1832		299.97				6.11		
1.57	5	pos		2520			300			8.40			
1.68	6	pos	7591			7025	20	379.55	351.25			13.85	15.74
1.70	6	neg	566				20	28.30				1.90	
1.90	6	neg			1087		300				3.62		
1.92	6	pos		1897			300			6.32			

Table 23: Third Long-term Test Trials 7-9, Fe-55 on

Time (Hours)	Trial	Amp Polarity	Counts	Pos Transitions	Neg Transitions	Corrected Counts	Duration (s)	Rate (Hz)	Corrected Rate (Hz)	Transition Rate Pos (Hz)	Transition Rate Neg (Hz)	Rate Error (Hz)	Corrected Rate Error (Hz)
2.77	7	pos	6553			6118	20	327.65	327.65			12.24	13.83
2.83	7	neg	435				20	21.75				1.59	
2.88	7	neg			1204		300				4.01		
3.00	7	pos		1657			335.35			4.94			
3.77	8	pos	5262			5061	20	263.10	253.05			10.20	11.16
3.80	8	neg	201				20	10.05				0.96	
3.92	8	neg			1392		300				4.64		
3.97	8	pos		1551			300			5.17			
4.95	9	pos	4641			4357	20.81	223.02	208.82			8.63	9.83
4.98	9	neg	284				20	14.20				1.20	
5.05	9	neg			2019		300				6.73		
5.15	9	pos		3873			300			12.91			

Table 24: Third Long-term Test Trials 10-12, Fe-55 on

Time (Hours)	Trial	Amp Polarity	Counts	Pos Transitions	Neg Transitions	Corrected Counts	Duration (s)	Rate (Hz)	Corrected Rate (Hz)	Transition Rate Pos (Hz)	Transition Rate Neg (Hz)	Rate Error (Hz)	Corrected Rate Error (Hz)
5.95	10	pos	4416			4274	20	220.80	213.70			8.84	9.62
5.98	10	neg	142				20	7.10				0.77	
6.12	10	neg			931		300				3.10		
6.22	10	pos		635			300			2.12			
6.95	11	pos	3987			3838	20	199.35	191.90			8.14	8.94
6.97	11	neg	149				20	7.45				0.80	
7.10	11	neg			838		300				2.79		
7.20	11	pos		760			300			2.53			
7.95	12	pos	3995			3834	20	199.75	191.70			8.15	8.99
7.97	12	neg	161				20	8.05				0.84	
8.07	12	neg			1409		300				4.70		
8.18	12	pos		431			300			1.44			

Table 25: Third Long-term Test Trials 13-15, Fe-55 on

Time (Hours)	Trial	Amp Polarity	Counts	Pos Transitions	Neg Transitions	Corrected Counts	Duration (s)	Rate (Hz)	Corrected Rate (Hz)	Transition Rate Pos (Hz)	Transition Rate Neg (Hz)	Rate Error (Hz)	Corrected Rate Error (Hz)
20.93	13	pos	2526			2465	20	126.30	123.25			5.67	6.14
20.98	13	neg	61				20	3.05				0.47	
21.23	13	neg			255		300				0.85		
21.32	13	pos		135			300			0.45			
25.00	14	pos	2593			2501	20	129.65	125.05			5.79	6.38
25.03	14	neg	92				20	4.60				0.59	
25.18	14	neg			372		300				1.24		
25.30	14	pos		22			300			0.07			
29.03	15	pos	2218			2191	20	110.90	109.55			5.13	5.42
29.07	15	neg	27				20	1.35				0.29	
29.12	15	neg			122		300				0.41		
29.27	15	pos		76			300			0.25			

Table 26: Third Long-term Test Trials 16-18, Fe-55 on

Time (Hours)	Trial	Amp Polarity	Counts	Pos Transitions	Neg Transitions	Corrected Counts	Duration (s)	Rate (Hz)	Corrected Rate (Hz)	Transition Rate Pos (Hz)	Transition Rate Neg (Hz)	Rate Error (Hz)	Corrected Rate Error (Hz)
33.03	16	pos	2034			2008	20	101.70	100.40			4.80	5.08
33.07	16	neg	26				20	1.30				0.29	
33.10	16	neg			60		300				0.20		
33.27	16	pos		450			300			1.50			
45.47	17	pos	1996			1971	20	99.80	98.55			4.73	5.01
46.02	17	neg	25				20	1.25				0.28	
46.23	17	neg			0		300				0.00		
46.32	17	pos		144			300			0.48			
48.03	18	pos	2159			2116	20	107.95	105.80			5.02	5.40
48.12	18	neg	43				20	2.15				0.38	
48.13	18	neg			0		300				0.00		
48.48	18	pos		54			300			0.18			

Tables for the Fourth Long-term Test

Table 27: Fourth Long-term Test Trials 1-2, Fe-55 on

Time (Hours)	Trial	Pos Counts	Transitions	Duration (s)	Avg Current (A)	Rate (Hz)	Corrected Rate (Hz)	Transition Rate (Hz)	Gain	Gain Error	Rate Error (Hz)	Corrected Rate Error (Hz)
0.00	1	10029		20		501.45	454.75		9.83E+04	20040.84	17.54	20.23906543
0.05	1			20								
0.22	1		1092	300				3.64				
0.35	1				-1.61E-09							
0.38	2	14589		20		729.45	662.95		2.54E+04	1186.41	24.28	27.76
0.40	2			20								
0.52	2		360	300				1.20				
0.65	2				-2.59E-10							

Table 28: Fourth Long-term Test Trials 3-4, Fe-55 on

Time (Hours)	Trial	Pos Counts	Transitions	Duration (s)	Avg Current (A)	Rate (Hz)	Corrected Rate (Hz)	Transition Rate (Hz)	Gain	Gain Error	Rate Error (Hz)	Corrected Rate Error (Hz)
0.70	3	13803		20		690.15	622.45		1.91E+04	6072.13	23.13	26.66
0.73	3			20								
0.87	3		257	300				0.86				
1.02	3				5.66E-10							
1.03	4	16335		20		816.75	755.90				26.81	30.07
1.05	4			20								
1.12	4		126	300				0.42				

Table 29: Fourth Long-term Test Trials 5-6, Fe-55 on

Time (Hours)	Trial	Pos Counts	Transitions	Duration (s)	Avg Current (A)	Rate (Hz)	Corrected Rate (Hz)	Transition Rate (Hz)	Gain	Gain Error	Rate Error (Hz)	Corrected Rate Error (Hz)
1.37	5	3786		20		189.30	131.35				7.81	10.96
1.38	5			20								
1.45	5		765	300				2.55				
1.75	6	6684		20		334.20	276.70		1.77E+04	28258.53	12.44	15.58
1.78	6			20								
1.82	6		207	300				0.69				
1.95	6				5.41E-10							

Table 30: Fourth Long-term Test Trials 7-8, Fe-55 on

Time (Hours)	Trial	Pos Counts	Transitions	Duration (s)	Avg Current (A)	Rate (Hz)	Corrected Rate (Hz)	Transition Rate (Hz)	Gain	Gain Error	Rate Error (Hz)	Corrected Rate Error (Hz)
2.08	7	6138		20		306.90	256.25		1.20E+03	322.86	11.59	14.45
2.13	7			20								
2.17	7		75	300				0.25				
2.27	7				2.34E-10							
3.20	8	5814		20		290.70	253.60		1.20E+04	582.92	11.08	13.37
3.22	8			20								
3.35	8		81	300				0.27				
3.50	8				4.34E-10							

Table 31: Fourth Long-term Test Trials 9-10, Fe-55 on

Time (Hours)	Trial	Pos Counts	Transitions	Duration (s)	Avg Current (A)	Rate (Hz)	Corrected Rate (Hz)	Transition Rate (Hz)	Gain	Gain Error	Rate Error (Hz)	Corrected Rate Error (Hz)
4.25	9	3376		20		168.80	132.25		2.96E+02	417.71	7.13	9.39
4.27	9			20								
4.40	9		210	300				0.70				
4.53	9				2.06E-10							
5.25	10	1530		20		76.50	46.20		6.46E+03	623.06	3.87	5.86
5.27	10			20								
5.43	10		307	300				1.02				
5.63	10				3.32E-10							

Table 32: The source-off reference trial of the fourth long-term test for use in gain calculations

Time (Hours)	Trial	Pos Counts	Transitions	Duration (s)	Avg Current (A)	Rate (Hz)	Corrected Rate (Hz)	Transition Rate (Hz)	Rate Error (Hz)	Corrected Rate Error (Hz)
5.67	source off ref				2.12E-10					
5.80	source off ref	339		20		16.95	8.50		1.34	2.21
5.82	source off ref			20						
5.97	source off ref		1	300				0.003		